COMPACT MUON SOLENOID DISCOVERY POTENTIAL FOR THE MINIMAL SUPERGRAVITY MODEL OF SUPERSYMMETRY IN SINGLE MUON EVENTS WITH JETS AND LARGE MISSING TRANSVERSE ENERGY IN PROTON-PROTON COLLISIONS AT CENTER-OF-MASS ENERGY 14 TEV

By

BOBBY SCURLOCK

A DISSERTATION PRESENTED TO THE GRADUATE SCHOOL
OF THE UNIVERSITY OF FLORIDA IN PARTIAL FULFILLMENT
OF THE REQUIREMENTS FOR THE DEGREE OF
DOCTOR OF PHILOSOPHY

UNIVERSITY OF FLORIDA

2006

ACKNOWLEDGMENTS

I am indebted to a great number of people without whom, I never could have completed this very long journey in science. I would like to thank my wife Belinda for her near infinite patience over the past 13 years during which time I have pursued this end. I am willing to wager that she did not believe me when I first told her of my plan back in the 11th grade. I thank my beautiful two month old daughter, Emilia, for keeping me company during the writing of most of this work. Despite her best efforts to pull me away from it, I managed to finish, and hopefully one day it will teach her what can be accomplished if she is willing to put forth the effort-just as her grandfather's work taught me. I would also like to thank my parents Dr. Bob Scurlock and Bonnie Rancel for their encouragement and support throughout this process. I thank my brother Tyrone Purvis as well as my most dear friends Garrett Cohen, Julio Blandon, and Raymond Chow for always reminding me that this career path is a noble one.

I would like to thank Mr. David Jones for delivering his lectures with the excitement and enthusiasm that are far too rare in the high school classroom. His Honors Physics class was the starting point for my journey. I am grateful to Professor Darin Acosta for hiring a nearly useless undergraduate eight years ago. Throughout our work together over the years, he maintained his usual degree of healthy skepticism towards my results, while showing me nothing but the utmost respect and kindness in voicing it. I've learned many valuable lessons from his leadership. I am also grateful to Dr. Richard Cavanaugh for his constant optimism and encouragement regarding our research. His support in this effort over the last two years has helped make this final step possible. I would like to thank Michael Schmitt for our daily, and at times

contentious, debates which thankfully had nothing to do with physics. I would also like to sincerely thank him for efforts in helping with this work.

I would also like to acknowledge the contributions from Yuriy Pakhotin, Konstantin Matchev, Kyoungchul Kong, Chris Tully, Jim Rohlf, Maria Spiropulu, Luc Pape, Andre Korytov, Guenakh Mitselmakher, and Salavat Abdullin to this work. In addition, this work would not have been possible without the excellent support from Craig Prescott, Yu Fu, and my old neighbor Jorge Rodriguez at the University of Florida CMS Tier-2 Center. I gratefully acknowledge my extensive use of computing resources from the LHC Computing Grid and the Open Science Grid, which were critical to the success of this thesis. Finally, I would like to express my gratitude to Lev Uvarov for making my service work on the Sector Processor so enjoyable. Lev is a truly unique individual.

TABLE OF CONTENTS

LIST OF TABLES

LIST OF FIGURES

Abstract of Dissertation Presented to the Graduate School
of the University of Florida in Partial Fulfillment of the
Requirements for the Degree of Doctor of Philosophy

COMPACT MUON SOLENOID DISCOVERY POTENTIAL FOR THE MINIMAL SUPERGRAVITY MODEL OF SUPERSYMMETRY IN SINGLE MUON EVENTS WITH JETS AND LARGE MISSING TRANSVERSE ENERGY IN PROTON-PROTON COLLISIONS AT CENTER-OF-MASS ENERGY 14 TEV

By

Bobby Scurlock

August 2006

Chairman: D. Acosta

Major Department: Physics

This dissertation estimates the ability of CMS to discover mSUGRA model of Supersymmetry in the single muon plus jets with missing transverse energy topology for 10 fb^{-1} of collected data using the inclusive-muon and di-muon High Level Trigger paths. A single low mass benchmark point ($m_0 = 60$ GeV/c^2, $m_{1/2} = 250$ GeV/c^2, $A_0 = 0$, $\mu > 0$, and $\tan(\beta) = 10$) is used to optimize the selection criteria and to study systematic uncertainties related to detector effects. Five sigma reach contours, including expected systematic uncertainties, are presented for 10, 30, and 60 fb^{-1}.

CHAPTER 1
INTRODUCTION

Modern particle physicists are reductionists; that is, they believe that all observable properties of macroscopic bodies can be explained in terms of the behavior of the more fundamental particles which compose them. So macroscopic states such as the temperature of a given object can be understood by the microscopic states of the particles from which it is composed. Perhaps the first scientifically useful ontology was offered by John Dalton in 1808. In his *A New System of Chemical Philosophy*, Dalton postulated the ancient idea that matter is composed of fundamental building blocks (atoms), which have particular properties such as weight, and can combine in particular ways to form larger structures. Dalton's postulates and laws offered a systematic way to study and understand matter. Nearly a century later, hints of atomic substructure began to emerge from the laboratories of Thomson and Rutherford. Of course we now know atoms are made of combinations of protons and neutrons which reside in the nucleus, and electrons which are in various orbital states outside of the nucleus. Over the last century, physicists have come to understand that the universe can be reduced even further to more fundamental particles (where fundamental is understood to mean having no additional sub-structure). The tradition of reductionism has ultimately led modern science to a mathematically consistent model (the *Standard Model*) of matter and its interactions, in which the smallest components of the universe are modeled to be point-like particles of infinitesimally small size with intrinsic properties.

The Standard Model of particle physics is a collection of theories from which predictions regarding the behavior of fundamental particles, and the forces which govern

their interactions (excluding gravity), can be derived. In the Standard Model there are twelve types of matter particles (six *leptons* and six *quarks*). The electrons (e), muons (μ), taus (τ), and their corresponding neutrinos (ν_e, ν_μ, and ν_τ) compose the lepton group. The e's, μ's, and τ's have electromagnetic charge, while the ν's remain electrically neutral. In the Standard Model, the ν's are massless particles* that can only interact through the weak interaction. From the six quarks, a vast array of particles called *hadrons* can be constructed. For example, protons and neutrons are constructed from different mixtures of *up*- and *down*- type quarks. The Standard Model fermions interact through the exchange of *gauge bosons*: the photon (γ) mediates the infinite range electromagnetic interaction between electrically charged particles, the massive W and Z bosons mediate the short range weak interaction, and the color charged gluons (g) mediate the strong interaction between particles with color charge. Particle masses are imparted in the Standard Model through the massive scalar Higgs boson: this critical piece of the Standard Model has thus far eluded detection, but if it does exist, will likely be discovered with the next generation collider machines.

The Standard Model contains equations that describe the dynamics of particle interactions. Although it provides a consistent mathematical framework within which calculations can be made, the Standard Model requires various input parameters based on measurements, such as particle masses and coupling constants, in order to ultimately obtain predictions of measurable quantities. For example, the decay width Γ_W† for the W boson can be expressed in terms of Fermi constant G_F‡ and

*Recent measurements of neutrino flavor oscillations demonstrate the neutrinos are likely massive particles. Popular extensions to the Standard Model, such as Grand Unified Theories, provide mechanisms for neutrinos to acquire mass thus indicating these results may provide the first glimpse at new physics beyond the Standard Model [1, 2].

†The inverse of Γ can be understood as the particle lifetime.

‡G_F can be understood as the coupling strength of the charged current weak interaction.

the W mass. Comparing the predicted value to the measured value shows a relative difference at the one percent level [3]. The Standard Model has allowed physicists to predict the behavior of the fundamental interactions of the known particles, and has been tested with precision measurements and has generally shown to be in excellent agreement with theoretical calculations [4].

Ultimately, the goal of particle physics is a complete description of all fundamental particles and forces through a set of a few basic equations, just as electromagnetism can be fully described through Maxwell's four equations. Unfortunately, laboratories are only able to reproduce conditions at energies far below that of the early universe. This likely implies that the Standard Model, which was developed through the analyses of low energy data, is likely to be at most a low energy effective theory which successfully describes particle phenomena at currently accessible energies. Indeed, despite the predictive success of the Standard Model, many questions remain, thus hinting that a new theory is needed.

One such theory, *Supersymmetry* (SUSY), may solve many problems with the Standard Model, by enforcing a new type of symmetry between half-integral-spin particles (*fermions*) and integral-spin particles (*bosons*). This new symmetry introduces many new particles (by more than a factor of two) and parameters into the theory. Some regions of SUSY parameter space are open to discovery at energies offered by the next generation colliders. Therefore, future experiments will be very important for the evolution of particle theory.

The proton-proton collider, the *Large Hadron Collider* (LHC), is scheduled to begin in late 2007. The LHC will offer the ability to study particle phenomena at unprecedented energies. The LHC will collide proton bunches together with center-of-mass energy likely starting at 0.9 TeV[§], and will ramp up to 14 TeV in 2008. This energy will be available for the creation of particles rarely seen because of their large

[§]1 eV (electron-volt) = 1.6×10^{-19} Joules.

masses, and typically short lifetimes. The *Compact Muon Solenoid* (CMS) experiment will surround one of the proton bunch crossing sites along the LHC ring, and will collect data from which the trajectories, energies, and momenta of the particle decays (which are products of the initial particle interactions), can be reconstructed. This task is accomplished with a series of specialized, yet complementary, detector subsystems, each of which is designed to be sensitive to particular kinematic parameters.

While the LHC is not currently colliding proton beams, analyses are being conducted using simulation software for both the underlying physics phenomenology and the CMS detector response, to study the ability of the CMS detector system to discover new physics. These analyses are useful in outlining strategies which may be employed to conduct searches with actual data. They also allow the CMS software framework to be exercised and tested for potential problems. In this dissertation, a study is presented on the feasibly to observe an excess of supersymmetric events over Standard Model events in the jets + missing transverse energy + muon topology. The dissertation is organized as follows:

- Chapter 2 briefly describes the Standard Model and one of its possible extentions Supersymmetry.
- Chapters 3 and 4 describe details of the next generation particle accelerator machine, the Large Hadron Collider and one of its experiments, the Compact Muon Solenoid experiment.
- Chapters 5 through 11 describe the methods and results of a simulation based study on the feasibility of the Compact Muon Solenoid detector system to provide evidence for the existence Supersymmetric particles.

CHAPTER 2
THE STANDARD MODEL AND BEYOND

2.1 The Standard Model

The Standard Model is considered a low energy effective theory of all known matter and their interactions [1, 5, 6, 7]. The theory consists of three interacting sectors which ideally, completely describe the constituents of the universe: the fermionic, gauge, and scalar sectors. The dynamics of these sectors is governed by the Standard Model Lagrangian and its gauge symmetries, where the Lagrangian is

$$\begin{aligned}
\mathcal{L} &= \bar{q}\gamma^{\mu}\left(i\partial_{\mu} - g_s T_a G_{\mu}^{a}\right) q - \frac{1}{4} G_{\mu\nu}^{a} G_{a}^{\mu\nu} \\
&+ \bar{L}\gamma^{\mu}\left(i\partial_{\mu} - \frac{i}{2}\bar{\tau}\cdot\bar{\mathrm{W}}_{\mu} - \frac{g'}{2}B_{\mu}Y\right) L + \bar{R}\gamma^{\mu}\left(i\partial_{\mu} - \frac{g'}{2}B_{\mu}Y\right) R \\
&- \frac{1}{4}\bar{W}_{\mu\nu}\cdot\bar{W}^{\mu\nu} - \frac{1}{4}B_{\mu\nu}B^{\mu\nu} \\
&+ \left|\left(i\partial_{\mu} - \frac{g}{2}\bar{\tau}\cdot\bar{\mathrm{W}}_{\mu} - \frac{g'}{2}B_{\mu}Y\right)\phi\right|^{2} - V(\phi) \\
&- G_e\left(\bar{L}\phi R + \bar{R}\phi^{\dagger}L + h.c.\right). \qquad (2.1)
\end{aligned}$$

Here, the first line describes the strong interaction where q is three component $SU(3)$ quark color field, G_{μ}^{a} is the gluon field, $G_{\mu\nu}^{a}$ is the gluon fields strength term, T_a is the $SU(3)$ generator, and g_s is the strong coupling strength. The second and third lines describe the electroweak interaction, where L is the left-handed* fermion SU(2) isospin doublet, R is right-handed isosinglet, $\bar{W}_{\mu}$ is the W boson three-vector; the

*Right- and left-handedness indicate the helicity state of a given particle, where left is understood as negative helicity and right as positive. Helcity can be understood as a particle's intrinsic-spin projection along its momentum direction. Handedness plays a particularly important role in the theory.

B_μ boson couples to the weak hypercharge,[†] $\bar{\tau}$ is the $SU(2)$ generator, Y is the $U(1)$ generator, and the coupling strengths are given by g and g'. The first three lines would be enough for a massless particle theory; however, the final two lines must be included to generate mass in the theory through interactions with the Higgs scalar field ϕ[‡].

2.1.1 Standard Model Fermions

The fermionic sector contains the matter content, which is composed of spin-1/2 particles called *fermions*. These particles obey the Pauli exclusion principle, and therefore, Fermi-Dirac statistics. There are two types of fermions, *leptons* and *quarks* (Table 2.1), each of which have six possible *flavors* that can be grouped into three generations, each heavier than the next.

2.1.2 Standard Model Gauge Bosons

The gauge sector contains the force carriers (*gauge bosons*); these gauge bosons allow the fermions to interact (Table 2.2). The most familiar of these gauge bosons is perhaps the neutral and massless photon (γ), which is described by the theory of quantum electrodynamics (QED), based on the $U(1)$ gauge group. The W^+, W^-, and the Z^0 are massive particles, which are capable of self-interaction, and are responsible for the weak nuclear force. These three massive *vector-bosons*, and the massless photon can be described in a unified way by the *Glashow-Weinberg-Salam model* [8, 9, 10]. This model is based on the gauge group $SU(2)_L \times U(1)_Y$, where the generator of the $U(1)_Y$ group is the hypercharge Y (defined such that $Q = T^3 + Y/2$), Q is the electric charge, and T^3 the third component of the weak isospin. The

[†]Note, the W_1, W_2, W_3, and B are not physically observable but gauge-eigenstates. The mass-eigenstates, Z^0, A^0, and $W^\pm$ are linear combinations of the gauge-eigenstate fields.

[‡]Including a potential energy terms into the Lagrangian such as $V(\phi) = \mu^2\phi^\dagger\phi + \lambda(\phi^\dagger\phi)^2$, which has a $U(1)$ global symmetry, allows the inclusion of mass terms in the Lagrangian by spontaneously breaking the gauge symmetry.

Table 2.1: Standard Model leptons.

Particle Name	Symbol	Charge (e)	Mass (GeV/c^2)
Leptons (spin-1/2)			
Electron	e^-	-1	5.11×10^{-4}
e-Neutrino	ν_e	0	$< 3 \times 10^{-8}$
Muon	μ^-	-1	0.106
μ-Neutrino	ν_μ	0	$< 0.19 \times 10^{-4}$
Tau	τ^-	-1	1.78
τ-Neutrino	ν_τ	0	$< 18.2 \times 10^{-4}$
Quarks (spin-1/2)			
Down	d	-1/3	0.008
Up	u	2/3	0.004
Strange	s	-1/3	0.15
Charm	c	2/3	1.2
Bottom	b	-1/3	4.5
Top	t	2/3	175

three generators of the $SU(2)_L$ group are $T_i = \sigma_i/2$, where σ_i are the three Pauli matrices. Mass is imparted to the electroweak vector-bosons through Spontaneous Symmetry Breaking (SSB), via the Higgs mechanism of the $SU(2)_L \times U(1)_Y$ gauge group [11, 12]. The $U(1)_{em}$ gauge group, which is responsible for the electromagnetic interaction, remains a symmetry of the broken vacuum state and therefore gives rise to a massless photon.

Table 2.2: Standard Model Gauge Bosons.

Force	Carrier	Symbol	Spin ($\hbar$)	Charge (e)	Mass (GeV/c^2)	Relative Strength	Range
Electro-magnetic	Photon	γ	1	0	0	~1/137	∞
Weak	Charged boson	$W^\pm$	1	± 1	81	$\sim 10^{-5}$	$\sim 10^{-18}$ m
	Neutral boson	Z^0	1	0	92		
Strong	Gluons	g_i	1	0	0	~ 1	$\sim 10^{-15}$ m

Through gluon exchange (the strong interaction), quarks are allowed to form hadrons. This interaction is described by the theory of Quantum Chromodynamics (QCD), which is based on the $SU(3)_C$ gauge group. This theory gives rise to eight gluons; each gluon is different mixture of two color charges (mixtures of red, blue, or green), therefore allowing gluons to interact with each other. The quarks are given one of three possible color charges. Quarks may interact through gluon exchange such that colorless (color-singlet) hadrons are formed in combinations of quark-antiquark pairs called *mesons* (e.g., $\pi^+ = u\bar{d}$) or more complex combinations called *baryons* (e.g., $p = uud$)[§]. As quarks and gluons are the only Standard Model particles which have color charge, only they can interact through the strong force.

An interesting consequence of the uncertainty principle[¶] is that the vacuum can be understood to be active with the production of so called virtual particle-antiparticle pairs. These pairs contribute to the "vacuum polarization" causes charge screening. For example, an electron can be surrounded by virtual electron-positron pairs. These pairs then act like a dielectric, aligning such that there is an effective cloud of negative charge surrounding the initial electron. Thus, the true charge of the electron is screened by this cloud. The electric charge, or coupling, can be probed by scattering this electron with another electron. As the energy of the probe electron increases, the effective coupling will change (or "run") as the distance between them decreases [13]. For the electromagnetic coupling, the strength increases with decreasing distance, as the probe penetrates the charge cloud. Because gluons are color-charged, and therefore self-interact, this type of screening effect for the strong coupling is more complicated. The vacuum can give rise to color-charged gluon pairs surrounding a

[§]Hadrons are required to be color-neutral objects, therefore mesons can be expressed by the combination $\frac{1}{3}\Sigma_{\alpha=R,G,B} q_1^\alpha \bar{q}_2^\alpha$ while baryons can be expressed by $\frac{1}{\sqrt{6}}\Sigma_{\alpha,\beta,\gamma=R,G,B}\epsilon^{\alpha\beta\gamma} q_1^\alpha q_2^\beta q_3^\gamma$ where the ϵ is anti-symmetric permutation tensor [1].

[¶]Heisenberg's uncertainty principle essentially establishes a fundamental limit on the precision of energy measurements for a given quantum system, $\Delta E \Delta t \geq \hbar/2$.

parton,[‖] these pairs then attract other color-charged virtual pairs from the vacuum. Therefore, a very complex color-charged cloud develops around the initial parton. The strong coupling constant also changes with the distance away from a parton probe; however, the coupling increases with increasing distance [14]. This result is called "antiscreening," and is responsible for "asymptotic freedom." Because antiscreening effects are small for close quarks, they behave as free particles. As quarks move apart, antiscreening causes an increase in interaction strength, thus increasing the required energy to pull the quarks apart. In principle, this causes quarks to be "confined" inside hadrons. If enough energy is provided, quarks may be pulled apart, building up enough energy to produce other quark-antiquark pairs which then combine to form new hadrons. These two examples provide hints that the Standard Model coupling constants may unify at some large energy.

2.1.3 Higgs Boson

The as of yet experimentally unverified scalar sector consists of the uncharged, massive, Higgs boson. The Higgs boson is required by the Glashow-Weinberg-Salam model in order to break the electroweak gauge symmetry by acquiring a non-zero vacuum expectation value. The electroweak model based on the $SU(2)_L \times U(1)_Y$ gauge group leads to massless electroweak vector bosons; however, these bosons are in fact massive, indicating that the $SU(2)_L \times U(1)_Y$ gauge symmetry is not respected by the vacuum, but broken through the Higgs mechanism. Through electroweak symmetry breaking, the $W^{\pm}$ and Z^0 bosons acquire their masses while preserving the massless gluon and photon interactions. The remaining Standard Model fermions also acquire their masses through interactions with the Higgs.

[‖] Quarks and gluons, the constituents of hadrons, are collectively known as partons.

2.1.4 Beyond the Standard Model

The Standard Model has been extremely successful in yielding experimentally confirmed predictions. Despite its great success, it is well known that the Standard Model is not a complete theory, but generally regarded as a low-energy effective theory for the following reasons [4]:

- The Standard Model contains no description of the gravitational force.
- No piece of the Standard Model requires the existence of three generations of quarks and three generations of leptons.
- In total the Standard Model depends on nineteen parameters: the three gauge coupling constants, the two parameters μ^2 and λ which determine the mass and self-coupling of the Higgs field, the nine quark and charged lepton masses, the three angles and one phase specifying the quark mixing matrix, and the θ_{QCD} phase which characterizes the QCD vacuum state. A satisfactory theory should have a way to predict these values and their relations.
- Electroweak symmetry breaking through the Higgs mechanism is inserted into the theory ad hoc in order to yield particle masses.
- In order to keep the Higgs mass of order 100 GeV/c^2, which satisfies Standard Model constraints, the effect of radiative corrections (Fig. 2.1) to the Higgs mass calculations must be cut off at some scale λ. The Higgs mass, given by $m_H^2 = m^2 - g^2\lambda^2$, where m is the bare Higgs mass and g is a dimensionless coupling constant, needs m^2 and $g^2\lambda^2$ to cancel up to 22 decimal places. This unlikely solution is called the fine-tuning (or naturalness) problem.
- The Standard Model provides no good candidate to explain the existence of "Dark Matter,"** which is supported through Astrophysical observation [16], provided for by the Standard Model.

Many theories have been developed to solve the aforementioned problems of the Standard Model. In *composite models* quarks and leptons are given a substructure

**Astrophysical observation supports the idea that the universe is made up of three ingredients of which baryons account for roughly 5%, "dark matter" 25%, and "dark energy" 70% [15]. Dark matter should be color and electrically neutral, otherwise it would likely have been detected. In the Standard Model, only the neutrino could satisfy these constraints; however, neutrino masses are too small to make up the needed abundance.

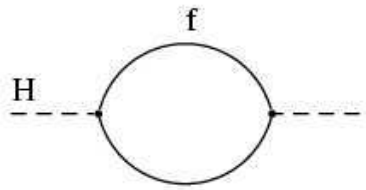

Figure 2.1: Fermion contribution to Higgs mass.

formed by common "preon" constituents; such models have been theoretically challenging as they do not explain the three generations of fermions, and none of the predicted excited states of quarks and leptons have been observed. *Technicolor* models, which propose a new "technicolor force" and "technifermions," can avoid the introduction of scalar particles which have problems with radiative corrections, but such models conflict with experimental bounds on flavor-changing neutral currents. In *Grand Unified Theories* (GUTs), a new unified gauge group is sought which could contain both the electroweak and color gauge groups. This pictures leads to the unification of electroweak and color couplings at some large energy scale; however, these models typically predict proton decays which have not be observed. One of the more promising theories, which addresses the challenges to the Standard Model, while having the flexibility to avoid contradictions with observation is Supersymmetry [1].

2.2 Supersymmetry

In Supersymmetry, each Standard Model particle is associated with a *superpartner* [17, 18]. The superpartner has a spin quantum number different by 1/2. This association more than doubles the particle content of the Standard Model. Supersymmetric models can be constructed in a variety of ways which can naturally ameliorate the previously mentioned difficulties faced by the Standard Model. For example, imposing this new symmetry allows the cancelation of the divergent contributions to the Higgs mass from fermion loops by introducing corrections from scalar particles (Fig

2.2), therefore solving the fine-tuning by forming the a new Higgs mass correction

$$\begin{aligned} \delta m_H^2 &= -\frac{g_f^2}{16\pi^2}(\Lambda^2 + m_f^2) + \frac{g_B^2}{16\pi^2}(\Lambda^2 + m_B^2) \\ &= \mathcal{O}(\frac{\alpha}{\pi}\left|m_B^2 - m_f^2\right|). \end{aligned} \tag{2.2}$$

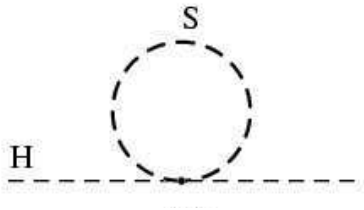

Figure 2.2: Scalar contribution to Higgs mass.

A supersymmetry is a symmetry relating fermions to bosons in a new way through the operation

$$Q\left|B\right\rangle = \left|F\right\rangle; \quad Q^\dagger\left|F\right\rangle = \left|B\right\rangle, \tag{2.3}$$

where Q, the transformation operator, is an anticommuting spinor with spin 1/2 [19]. This operator transforms bosonic states to fermionic states, and vice versa. The Standard Model fermions transform to bosonic *sfermions* and the Standard Model gauge bosons transform to *gauginos*. The resulting supersymmetric particles (*sparticles*) share the number of degrees of freedom as their superpartners.

In a supersymmetric gauge theory, superpartners are grouped into a *supermultiplet* whose elements are connected by the Q operator. This operator commutes with Hamiltonian, and thus the elements of the supermultiplet share the same mass. However, there have been no observed superpartners to the Standard Model particles. This implies if a supersymmetric description of nature is correct, the symmetry must be a broken one, as the superpartner masses must be at energies previously inaccessible by experiment.

2.2.1 The Minimal Supersymmetric Standard Model

The Minimal Supersymmetric Standard Model (MSSM) provides the simplest means to extend the Standard Model to include superpartners and their interactions by requiring the fewest number of particles and interactions needed to generate the proper supersymmetric phenomenology.

2.2.2 MSSM Particle Content

The MSSM Lagrangian maintains the same gauge group symmetry of the Standard Model, $SU(3)_C \times SU(2)_L \times U(1)_Y$, and contains all of the Standard Model particles plus their new superpartners (Table 2.3). Each Standard Model particle is combined with its superpartner, with spin differing by 1/2, in a supermultiplet.

Table 2.3: Chiral and gauge supermultiplets in the MSSM.

Name	spin 0	spin 1/2	spin 1
squarks, quarks	$\left(\tilde{u}_L, \tilde{d}_L\right)$	(u_L, d_L)	-
(x 3 families)	$\tilde{u}_R^*$	$u_R^\dagger$	-
	$\tilde{d}_R^*$	$d_R^\dagger$	-
sleptons, leptons	$(\tilde{\nu}, \tilde{e}_L)$	(ν, e_L)	-
(x 3 families)	$\tilde{e}_R^*$	$e_R^\dagger$	-
Higgs, higgsinos	(H_u^+, H_u^0)	$\left(\tilde{H}_u^+, \tilde{H}_u^0\right)$	-
	$\left(H_d^0, H_d^-\right)$	$\left(\tilde{H}_d^0, \tilde{H}_d^-\right)$	-
gluino, gluon	-	$\tilde{g}$	g
winos, W bosons	-	$\tilde{W}^\pm$, $\tilde{W}^0$	$W^\pm$, W^0
bino, B boson	-	$\tilde{B}^0$	B^0

The left- and right-handed Standard Model leptons are assigned scalar superpartners individually, as indicated by the "L" and "R" subscripts. The "quarks" and "squarks" maintain color charge. Both the squarks and sleptons maintain the same interactions as their Standard Model superpartners. The Standard Model Higgs is replaced by two complex chiral Higgs multiplets. These impart mass to the up- and

down-type quarks, as well as the leptons. These new Higgs particles have their own superpartners called higgsinos. Three of the eight degrees of freedom of the two Higgs doublets are absorbed to impart mass to the $W^{\pm}$ and Z^0 bosons. This leaves five Higgs bosons: $\{H^{\pm}, H^0, h^0, A^0\}$. The superpartners to the Higgs and electroweak bosons mix to form the *neutralinos* ($\tilde{\chi}_i^0, i = 1, 2, 3, 4$) and the *charginos* ($\tilde{\chi}_i^{\pm}, i = 1, 2$) (Table 2.4).

Table 2.4: Mass and gauge eigenstates in the MSSM.

Name	spin	Mass Eigenstates	Gauge Eigenstates
squarks	0	$\tilde{u}_L, \tilde{u}_R, \tilde{d}_L, \tilde{d}_R$ $\tilde{c}_L, \tilde{c}_R, \tilde{s}_L, \tilde{s}_R$ $\tilde{t}_1, \tilde{t}_2, \tilde{b}_1, \tilde{b}_1$	$\tilde{u}_L, \tilde{u}_R, \tilde{d}_L, \tilde{d}_R$ $\tilde{c}_L, \tilde{c}_R, \tilde{s}_L, \tilde{s}_R$ $\tilde{t}_L, \tilde{t}_R, \tilde{b}_L, \tilde{b}_R$
sleptons	0	$\tilde{e}_L, \tilde{e}_R, \tilde{\nu}_e$ $\tilde{\mu}_L, \tilde{\mu}_R, \tilde{\nu}_\mu$ $\tilde{\tau}_1, \tilde{\tau}_2, \tilde{\nu}_\tau$	$\tilde{e}_L, \tilde{e}_R, \tilde{\nu}_e$ $\tilde{\mu}_L, \tilde{\mu}_R, \tilde{\nu}_\mu$ $\tilde{\tau}_L, \tilde{\tau}_R, \tilde{\nu}_\tau$
neutralinos	1/2	$\tilde{\chi}_1^0, \tilde{\chi}_2^0, \tilde{\chi}_3^0, \tilde{\chi}_4^0$	$\tilde{B}^0, \tilde{W}^0, \tilde{H}_u^0, \tilde{H}_d^0$
charginos	1/2	$\tilde{\chi^{\pm}}_1, \tilde{\chi^{\pm}}_2$	$\tilde{W}^{\pm}, \tilde{H}_u^+, \tilde{H}_d^-$
gluino	1/2	$\tilde{g}$	$\tilde{g}$

2.2.3 R-Parity

The MSSM includes terms in its Lagrangian which allow baryon number and lepton number violating interactions [20]. Such violations, which can lead to proton decay, are strongly constrained by experiment. These violations can be handled in the MSSM by requiring that *R-Parity* be conserved, where R-parity is defined as:

$$R_P = (-1)^{(3B+L+2s)}, \tag{2.4}$$

where B is baryon number, L is lepton number, and s is the particle spin. As a result of this definition, the Standard Model particles have the value $R_P = +1$, while their superpartners have $R_P = -1$.

Imposing R-parity conservation on Supersymmetric interactions has very important consequences for the phenomenology of the theory as all sparticles must be pair produced and finally decay to the lightest supersymmetric particle (LSP). Since this LSP is heavy and weakly-interacting, it could be good candidate for dark matter.

2.2.4 Soft Supersymmetry Breaking

Because Supersymmetry is a broken symmetry, as low mass SUSY particles have yet to be observed, the Lagrangian must contain terms which violate invariance under the SUSY transformation. In the MSSM, this can be accomplished by writing the Lagrangian to include a *soft-breaking* term [21]

$$\mathcal{L} = \mathcal{L}_{SUSY} + \mathcal{L}_{soft}. \tag{2.5}$$

Here, $\mathcal{L}_{SUSY}$ describes the generalization of the Standard Model and remains invariant under the Supersymmetry transformation. The soft-breaking term, $\mathcal{L}_{soft}$, contains the masses and couplings while still allowing the cancelation of quadratic divergences. This term is constructed to become negligible at high energy scales.

This soft-breaking term introduces over 100 new free parameters into the theory of which, the new mass parameters introduce the needed mass splittings between superpartners contained in the same supermultiplets. The large number of free parameters allow the MSSM the flexibility to assume gauge coupling unification at the scale of $\mathcal{O}(10^{16}$ GeV). This is another ingredient of the theory that makes SUSY so attractive, as the Standard Model has no mechanism for unifying the strong and electroweak coupling constants in a natural way (Fig. 2.3) [22].

Although soft-breaking in the MSSM gives the needed mass splittings and solves many of the problems in the Standard Model listed above, nearly the full parameter space is forbidden by observation due to effects in the theory such as Flavor Changing Neutral Currents (FCNC), CP violation, and violations of lepton number conserva-

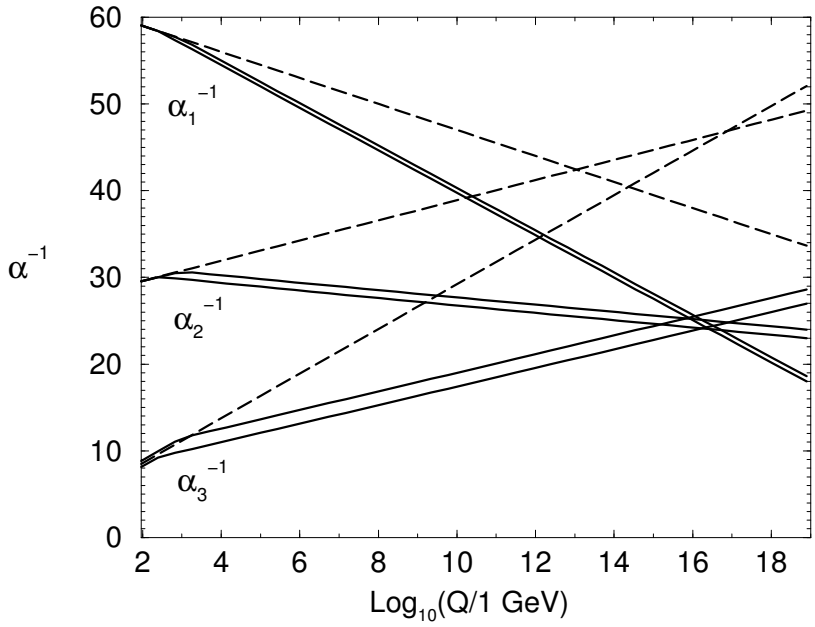

Figure 2.3: Evolution of inverse gauge couplings in the Standard Model (dashed lines) and the MSSM (solid lines). The MSSM lines are drawn with variations in sparticle masses and the strong coupling [19].

tion. There is also no understanding of the origin of the SUSY breaking parameters, or choice of parameters which leads to electroweak symmetry breaking. By embedding SUSY in a Grand Unification Theory (GUT) framework, it becomes possible to solve these problems.

2.2.5 Minimal Supergravity

The soft breaking terms run as a function of energy scale as do the gauge couplings. Parameters such as gaugino and scalar particle mass terms unify at some large scale M_X. SUSY breaking is mediated from the *hidden sector* to the *visible sector* by flavor-blind interactions such as gravity. This is the mechanism described in the *minimal Supergravity* (mSUGRA) scenario [23]. By forcing the soft-breaking terms to be consistent with observable phenomena, and imposing the initial conditions of the model parameters at the unification scale, the number of free parameters in the theory is significantly reduced and includes:

- m_0, the common scalar mass term at the unification scale
- $m_{1/2}$, the common gaugino mass term at the unification scale
- $\tan\beta$, the ratio of vacuum expectation values of the two Higgs doublets
- A_0, a common trilinear coupling constant at unification scale
- sign(μ), the sign of the Higgsino mass parameter

By evolving these parameters from energies at the GUT scale to the electroweak scale, the SUSY particle spectrum and mixing angles become determined (Fig. 2.4) [24].

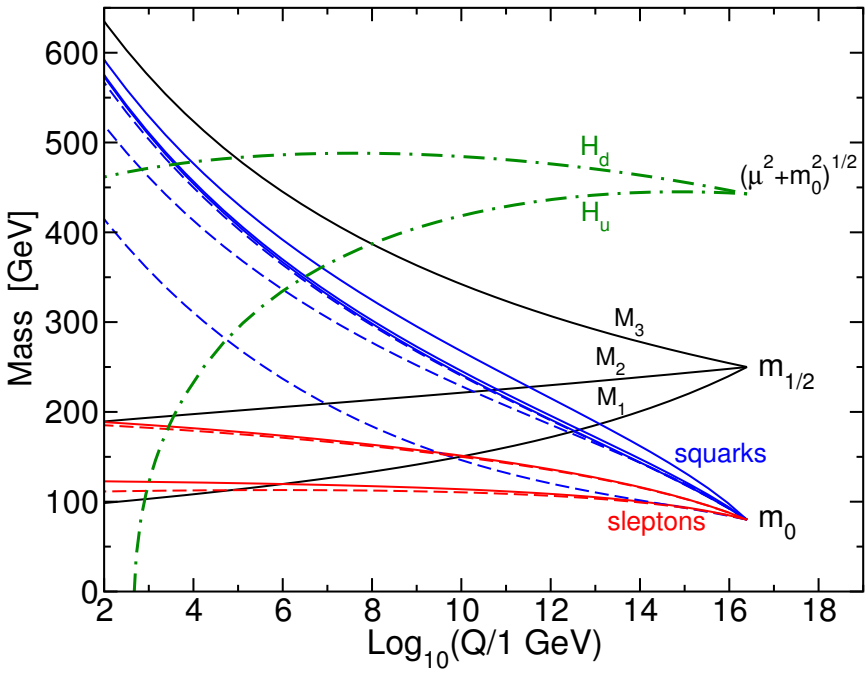

Figure 2.4: Evolution of scalar and gaugino mass parameters in the MSSM, imposing unification boundary conditions [19].

The Higgs mass parameter is given by solving [19]

$$\tan^2\beta = \frac{\mu^2 + m_{H_1}^2 + m_Z^2/2}{\mu^2 + m_{H_2}^2 + m_Z^2/2}. \tag{2.6}$$

As the free SUSY parameters are evolved down to the electroweak scale, μ is driven negative. This is precisely what is required to induce electroweak symmetry breaking, which now becomes a natural consequence of the theory.

2.2.6 Past Searches and Limits

At present, no experiment has been able to yield a measurement which confirms the existence of sparticles; however, previous studies can restrict the allowable parameter space for supersymmetric models, for example by setting lower bounds on sparticle mass spectra, as well as restricting the allowed values of other model parameters such as those in mSUGRA. Below is a brief summary of past experimental searches. A summary is given in Table 2.5, and combined limits are shown in Figure 2.5.

- **The LEP experiments (ALEPH, DELPHI, L3, OPAL)**: results were obtained using e^+e^- collisions at $\sqrt{s}$ energies from the Z peak to ~ 200 GeV/c^2. In these collisions, the sparticle production cross-section is dominated by charginos and neutralinos, typically decaying directly to SM particles and LSP's. The typical signature consists of jets, leptons, and missing energy [25]. For example, finding no excess of events over Standard Model expectations in acoplanar opposite-charge-same-flavor lepton pairs plus missing energy topology, the ALEPH experiment was able to establish lower bounds on the masses of $m(\tilde{e_R}) > 95$ GeV/c^2, $m(\tilde{\mu}_R) > 88$ GeV/c^2, and $m(\tilde{\tau}_R) > 79$ GeV/c^2 at 95% C.L., assuming $\mu = -200$ GeV/c^2 and $\tan\beta = 2$ [26]. The dominate slepton decay is through $\tilde{l}^{\pm} \rightarrow l^{\pm}\tilde{\chi}_1^0$, and slepton pairs produced through s-channel exchange of a Z or γ.
- **The Tevatron experiments (CDF, D0)**: results were obtained using $p - \bar{p}$ collisions at $\sqrt{s} = 1.8$ TeV/c^2. The sparticle production cross section is dominated squark and gluino production due to the effect of strong coupling. These are pair produced, and typically cascade decay down through lower mass sparticles such that events have at least two LSPs, therefore leading to a signature of leptons + multi-jets + missing transverse energy [27, 28]. For example, the CDF collaboration has searched for the pair produced $\tilde{t}_1$ in the two jets plus missing transverse energy topology from the decay $\tilde{t}_1 \rightarrow c\tilde{\chi}_1^0$. Searches were also conducted examining events with b-tagged jets plus muons and missing transverse energy from the decay $\tilde{t}_1 \rightarrow bl\tilde{\nu}$. In both cases, no excess events above Standard Model expectations were found [29].

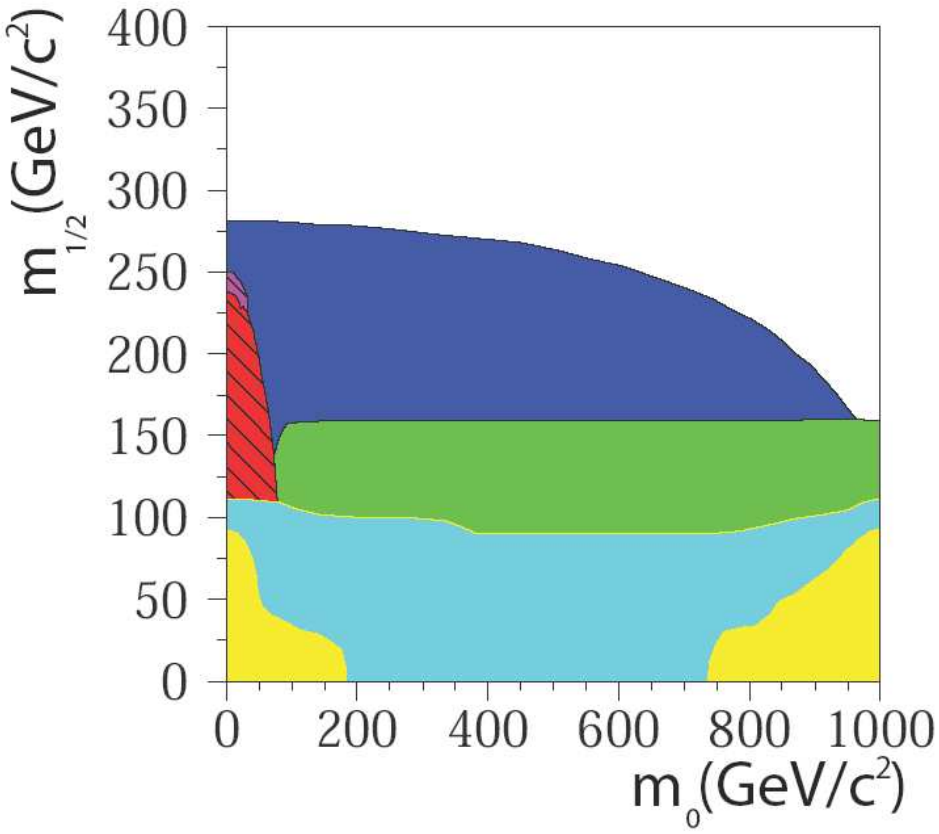

Figure 2.5: Excluded regions in the mSUGRA universal (m_0, $m_{1/2}$) plane. The different regions in this plot are: Yellow - forbidden by theory, Light blue - inconsistent with measurement of the electroweak parameters at LEP1, Green - regions excluded by chargino searches, Red - regions excluded by selectron or stau searches, Dark blue - regions excluded by Higgs searches, Brown regions excluded by neutralino stau cascade searches, Magenta - regions excluded by the search for heavy stable charged particles applied to staus [25].

Table 2.5: Lower limits on supersymmetric particle masses assuming the mSUGRA scenario [3].

Particle		Condition	Lower Limit (GeV/c^2)	Source
$\tilde{\chi}_1^{\pm}$	gaugino	$M_{\tilde{\nu}} > 200$ GeV/c^2	103	LEP 2
		$M_{\tilde{\nu}} > M_{\tilde{\chi}^{\pm}}$	85	LEP 2
		any $M_{\tilde{\nu}}$	45	Z width
	Higgisino	$M_2 < 1$ TeV/c^2	99	LEP 2
$\tilde{\chi}_1^0$	indirect	any $\tan\beta$, $M_{\tilde{\nu}} > 500$ GeV/c^2	39	LEP 2
		any $\tan\beta$, any m_0	36	LEP 2
		any $\tan\beta$, any m_0, SUGRA Higgs	59	LEP 2 combined
$\tilde{e}_R$	$e\tilde{\chi}_1^0$	$\Delta M > 10$ GeV/c^2	99	LEP 2 combined
$\tilde{\mu}_R$	$\mu\tilde{\chi}_1^0$	$\Delta M > 10$ GeV/c^2	95	LEP 2 combined
$\tilde{\tau}_R$	$\tau\tilde{\chi}_1^0$	$M_{\tilde{\chi}_1^0} > 20$ GeV/c^2	80	LEP 2 combined
$\tilde{\nu}$			43	Z width
$\tilde{\mu}_R, \tilde{\tau}_R$		stable	86	LEP 2 combined
$\tilde{t}_1$	$c\tilde{\chi}_1^0$	any θ_{mix}, $\Delta M > 10$ GeV/c^2	95	LEP 2 combined
		any θ_{mix}, $M_{\tilde{\chi}_1^0} \sim \frac{1}{2} M_{\tilde{t}}$	115	CDF
		any θ_{mix}, any ΔM	59	ALEPH
	$b\ell\tilde{\nu}$	any θ_{mix}, $\Delta M > 7$ GeV/c^2	96	LEP 2 combined
$\tilde{g}$	any $M_{\tilde{g}}$		195	CDF jets + $\not\!\!E_T$
$\tilde{q}$	$M_{\tilde{q}} - M_{\tilde{g}}$		300	CDF jets + $\not\!\!E_T$

CHAPTER 3
EXPERIMENTAL APPARATUS

3.1 The Large Hadron Collider

3.1.1 Overview of the Collider

The Large Hadron Collider (LHC) is scheduled to become operational during the third quarter of 2007 [30]. It consists of two 27 kilometer long proton synchrotrons, which have been designed to share the same tunnel as that which housed the previous Large Election Positron Collider (LEP), and sits 100 m beneath the Swiss/French countryside near Geneva (Fig. 3.1). The LHC will provide proton-proton collisions at a center-of-mass energy of 14 TeV; this is approximately 7 times higher than the worlds highest energy collider, the Tevatron at Fermilab in Chicago. Figure 3.2 illustrates the cross sections and event rates of the phenomena expected to be studied at the LHC [31]. In addition to proton-proton collisions, the LHC will provide heavy-ion collisions subsequent to the first physics runs with protons.

Proton bunches will collide at a frequency of 40 MHz, or every 25 ns, when the LHC is running at full design luminosity* at 10^{34} cm^{-2}s^{-1} - nearly 100 times that achievable by the Tevatron. This is accomplished by accelerating 2835 proton bunches, where each bunch is composed of 10^{11} protons.

The commissioning of the LHC will commence during the third quarter of 2007, first accelerating single beams containing a few bunches, followed by a low luminosity pilot run consisting of machine development periods and data-taking runs [33].

*The luminosity $\mathcal{L} = f\frac{N_1 N_2}{4\pi\sigma_x\sigma_y}$, where f is the collision frequency, N_i is the number of particles per bunch, and σ_j is the rms bunch transverse length. A physics process with a particular production cross-section σ, will then result in an event rate of $R = \mathcal{L}\sigma$ [32].

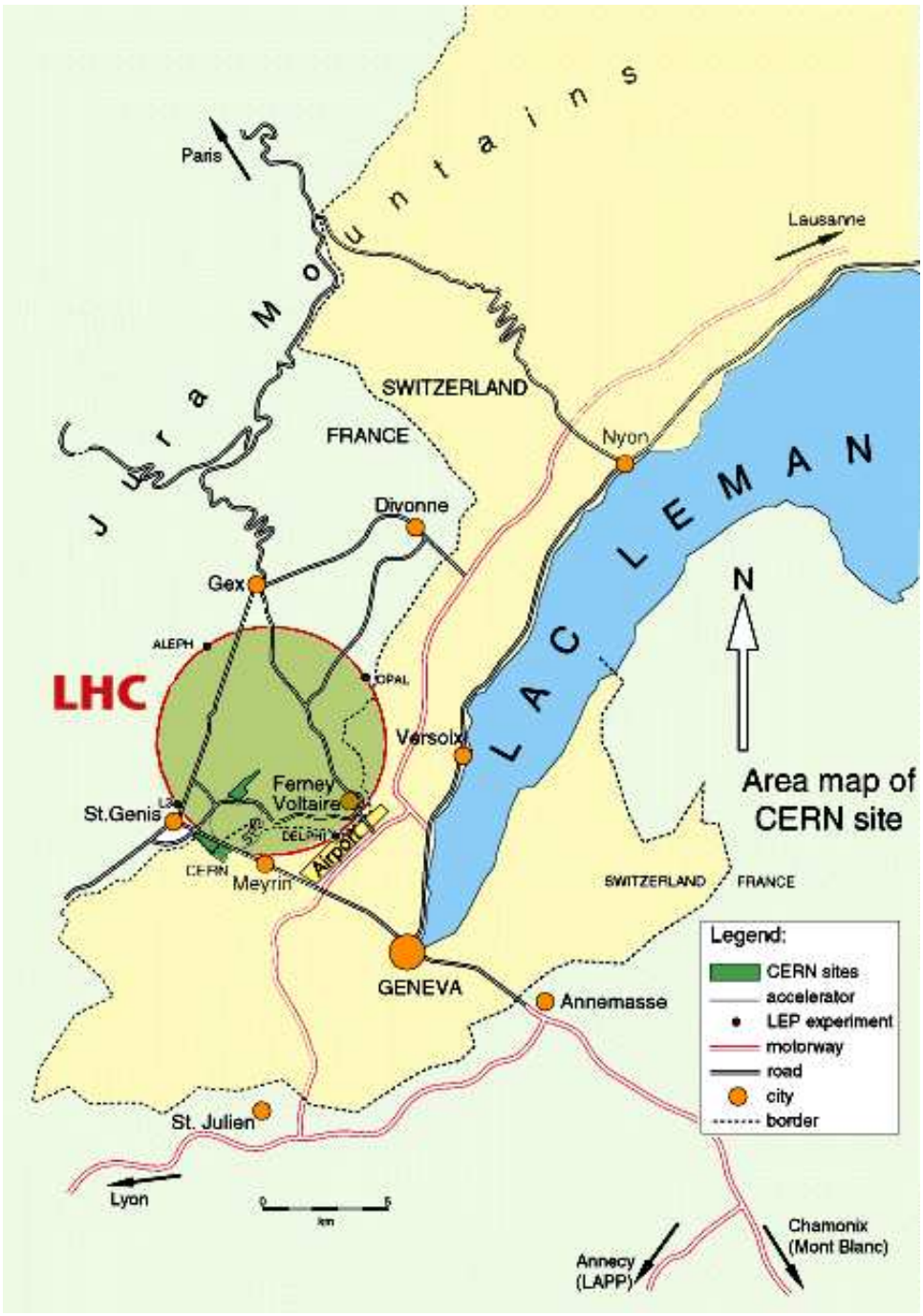

Figure 3.1: LHC geographical situation.

During this debugging phase, only 43 or 156 bunches per beam will be accelerated. A luminosity of 2×10^{31} cm^{-2}s^{-1} is achievable during runs with 156 bunches: a month-long pilot physics run could lead to 10 pb^{-1} of integrated luminosity[†].

The LHC will increase to 936 bunches with 75 ns spacing in 2008, and will eventually be changed to 25 ns spacing, increasing the beam content to 2808 bunches. An instantaneous luminosity of 2×10^{33} cm^{-2}s^{-1} is anticipated until 2010, with the first year of physics running delivering 5 fb^{-1}.

Since the LHC will collide proton bunches, each of the two synchrotrons will require its own magnetic field such that the protons can be held in counter rotating orbits during spill cycles. Protons are kept in orbit around the LHC ring through Lorentz force[‡] induced by a 8.33 Telsa magnetic field provided by 1296 superconducting dipole magnets.

Since the proton-proton interaction cross-section (or probability) is proportional to 1/Energy^2, a high beam luminosity is required to ensure an interaction rate high enough to facilitate a successful physics program. Because of the high collision luminosity, and total proton-proton inelastic cross-section $\mathcal{O}(100$ mb) at the LHC, nearly 20 proton interactions per bunch crossing are expected at full design luminosity or 800 million proton interactions per second. The large interactions rate presents a considerable challenge for readout electronics, triggering, and data acquisition. The LHC accelerator chain is described below.

[†]1 barn = 10^{-24} cm^2. Therefore, we have $\mathcal{L} = 2 \times 10^{31}$ cm^{-2}s^{-1} = 2×10^{-5} pb^{-1}s^{-1}. This means $\int^{1\ \mathrm{month}} \mathcal{L}dt \sim 10$ pb.

[‡]A particle of electric charged q moving with velocity $\vec{v}$ through an electric field of strength $\vec{E}$ and a magnetic field of strength $\vec{B}$, will experience a force given by $\vec{F} = q(\vec{E} + \vec{v} \times \vec{B})$ [34]. This relation along with the centripetal force equation, can be used to determine the momentum p of a particle held in circular orbit of radius r, which is given by $p(\mathtt{GeV}) = 0.3Br$.

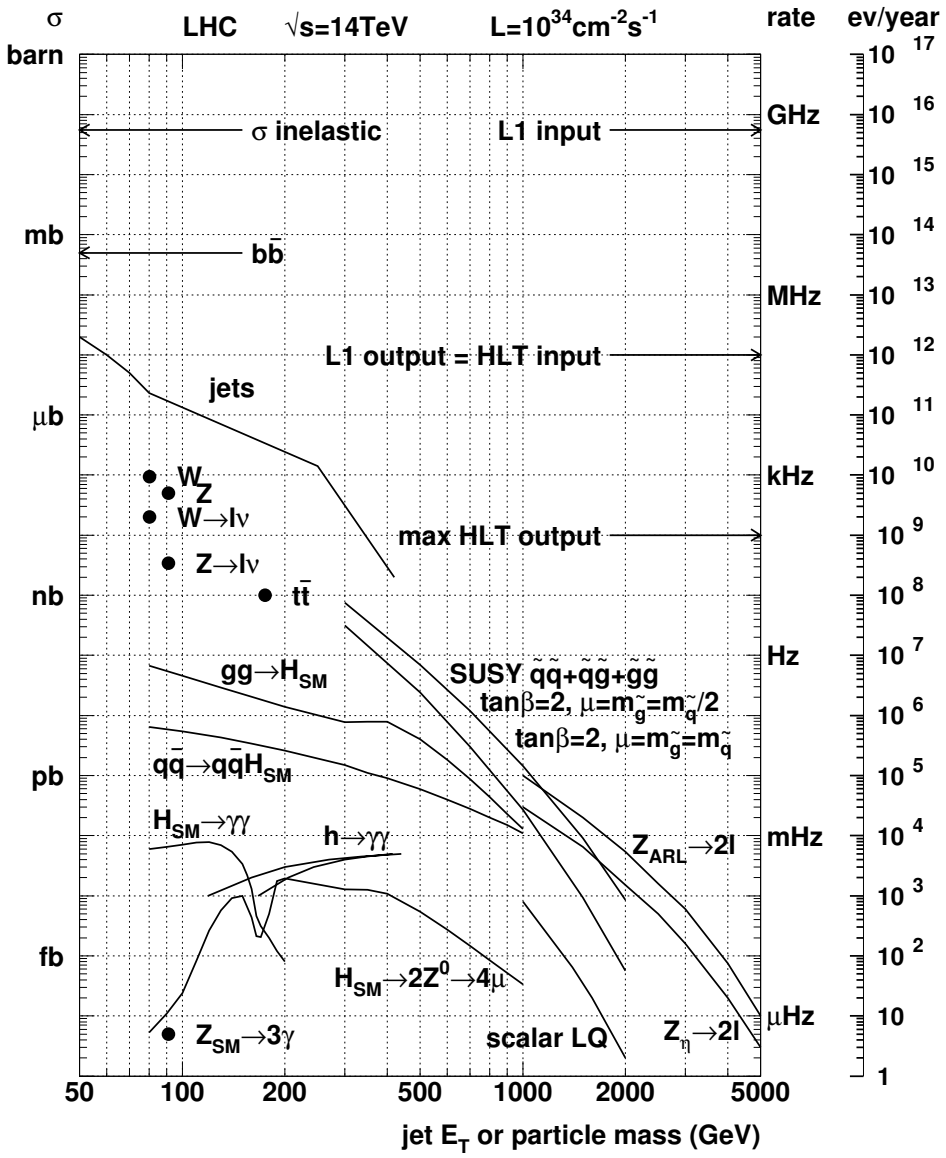

Figure 3.2: Inclusive proton-proton cross sections for physics processes of interest at the LHC [31].

3.1.2 Proton Source

The LHC accelerator chain is shown in Figure 3.3 [35]. First, a duoplasmatron source is used to extract protons from hydrogen gas. Bunches of these protons are then accelerated to 50 MeV by a linear accelerator (Linac2) and sent separately into one of four booster rings. These booster rings are then used to further accelerate the protons an additional 1.0 GeV, thus preparing them for next injection. The LHC receives protons from the older 200 meter diameter Proton Synchrotron (PS). The PS is an all purpose accelerator ring that in particular will be used for the acceleration and injection into the Super Proton Synchrotron (SPS) ring. The PS takes bunches from each booster, combines them into larger bunches, and accelerates them to 0.026 TeV. A 40 MHz RF system takes the bunches from the PS and injects them into the SPS, where the bunches are separated by 25 ns. This proton bunch structure is very important for data synchronization. The CMS readout electronics for the detector systems is synchronized to the LHC collision frequency, latching in data from each 25 ns window.

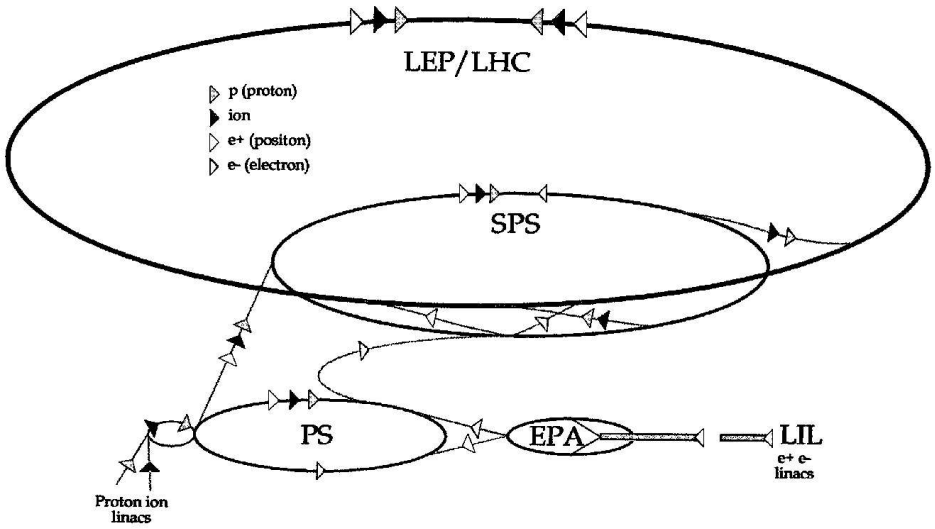

Figure 3.3: LHC Accelerator chain.

The 6 km long SPS ring will accelerate the protons to 0.45 TeV before injection into the LHC, where they are then accelerated to 7 TeV in about 20 minutes. The LHC ring will require new proton bunches every 10 hours due to inefficiencies in keeping them in orbit over four-hundred-million times; one such inefficiency is caused by deflections from the beam-beam interactions during a bunch crossing. The additive effect of multiple deflections can cause proton losses within the beam.

3.1.3 Detector Systems

The LHC will host five detector systems (Fig. 3.4) with each served their own beam crossing. Point 2 will contain ALICE, A Large Ion Collider Experiment, a detector that is specialized for heavy ion collisions. Point 8 hosts the LHC-B experiment, which is a dedicated B-physics detector. The remaining two detectors are considered multi-purpose, and are in some sense competing experiments: they are A Toroidal LHC Apparatus (ATLAS) at Point 1, and The Compact Muon Solenoid (CMS) at Point 5. The TOTEM (Total Cross Section, Elastic Scattering and Diffraction Dissociation) experiment shares point 5 with CMS and will study forward physics.

3.2 The Compact Muon Solenoid

Because we cannot directly observe the interactions which govern the behavior of subatomic particles, but rather their final decay products, we must enclose the volume around the proton bunch collisions with detectors whose data results in measurements of various kinematic parameters. Parameters such as position, momentum, energy, mass, are the measurable quantities that can uniquely describe the underlying initial particle interactions. Thus, the goal of the CMS detector is the measure these quantities as completely and precisely as possible using an array of specialized detectors, each of which will supply a piece of the complete event structure [36]. These detector systems are arranged in a series of concentric cylinders about the beam axis. Starting from the layer nearest the beam pipe, CMS has the following detector systems

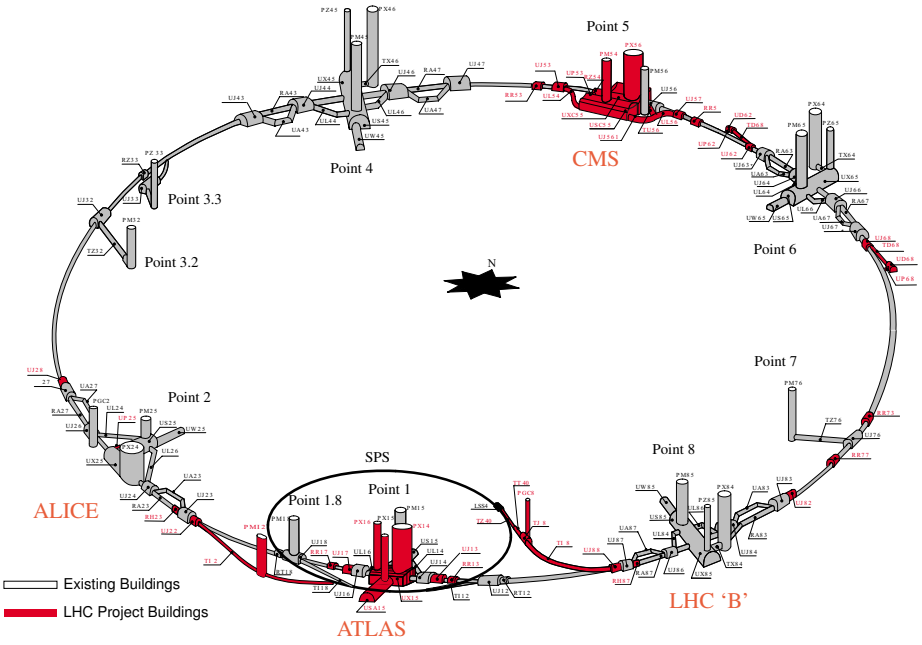

Figure 3.4: Location of LHC experiments along main ring.

(Fig. 3.5): First is the inner tracker system, capable of charged track reconstruction and high resolution momentum measurements with good efficiency. Based on pixel and microstrip detectors, the tracker has good special resolution that allows for the tagging of heavy flavor jets originating from b and c quark decays. After the tracker system is the Electromagnetic Calorimeter system (ECAL). A $PbWO_4$ scintillating crystal calorimeter, the ECAL system measures the energy and direction of electrons and photons. It must have good energy measurement resolution such that a di-photon and di-electron mass resolution of better than 1% at 100 GeV is possible. The third layer is the Hadron Calorimeter (HCAL) system. Working in conjunction with the ECAL system, this sampling calorimeter measures the energy and direction of particle jets. This system must provide good hermetic coverage such that reasonable energy measurements can be made. After the HCAL system is the 4 Tesla superconducting solenoid which provides the magnetic field that causes bending in particle trajectories. The final detector system is the muon system. Benefiting from the muons relatively long lifetime and large mass, muons provide a clean signature of new physics. The

muon system is placed outside both calorimeters. The muon system provides good muon identification, charge assignment, and is able to reconstructed di-muon masses at better than 1% resolution for 100 GeV muons. Each detector subsystem will be described in more detail below.

3.2.1 Coordinate System

The CMS detector is approximately 21.6 m in length from end-to-end, has a diameter of approximately 15 m, and weighs 12500 t. CMS uses a cylindrical coordinate system in which the x-axis points towards the LHC center, y-axis points vertically, and the z-axis runs parallel to the beam line and points towards the Jura mountains. The azimuthal angle ϕ (Fig. 3.6) is measured away from the x-axis, and the polar angle θ is measured away from the z-axis. It is usually more convenient to work with the pseudorapidity $\eta = -\ln(\tan\theta/2)$ rather than θ (Fig. 3.7), as particle production is roughly uniform as a function of η.

3.2.2 Magnet

The magnetic field is at the heart of CMS (Table 3.1) [37]. The liquid helium superconducting solenoid at CMS is 13 m long, and generates a 4 T field. This field is sufficiently strong enough to allow for precise muon tracking and momentum measurements using track curvature caused by the Lorentz force up to $|\eta| < 2.5$. As of this writing, the magnet has been installed, and has began undergoing tests, including a successful cool-down period. The magnet will be used during the CMS Magnet Test and Cosmic Challenge (MTCC). The primary goal of the magnet test is to check functionality of the magnet including its cooling, power supply and control systems. In addition, tests will be conducted to map the magnetic field, check closure tolerances and the field tolerance of yoke mounted components [38].

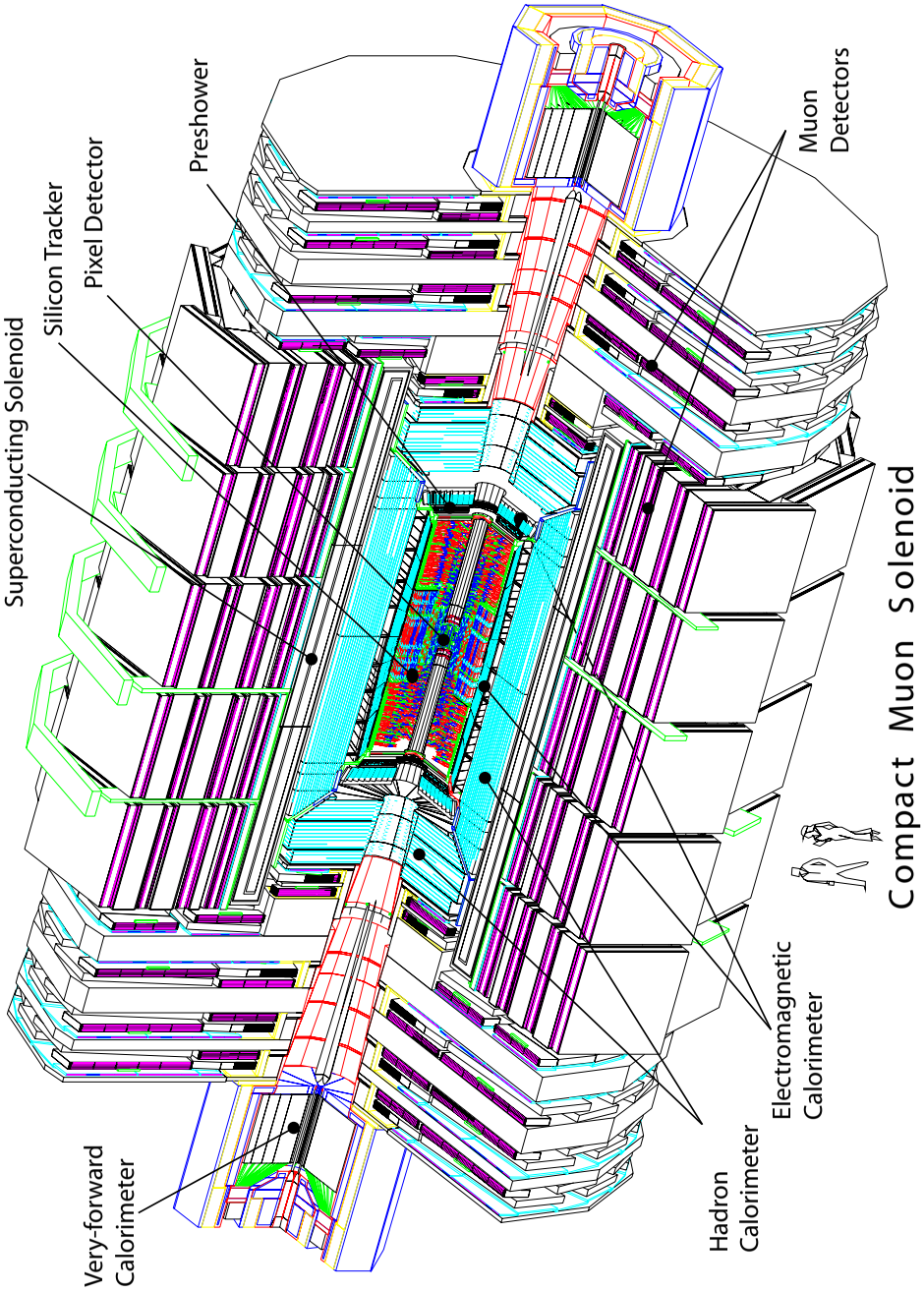

Figure 3.5: Schematic of the CMS detector system.

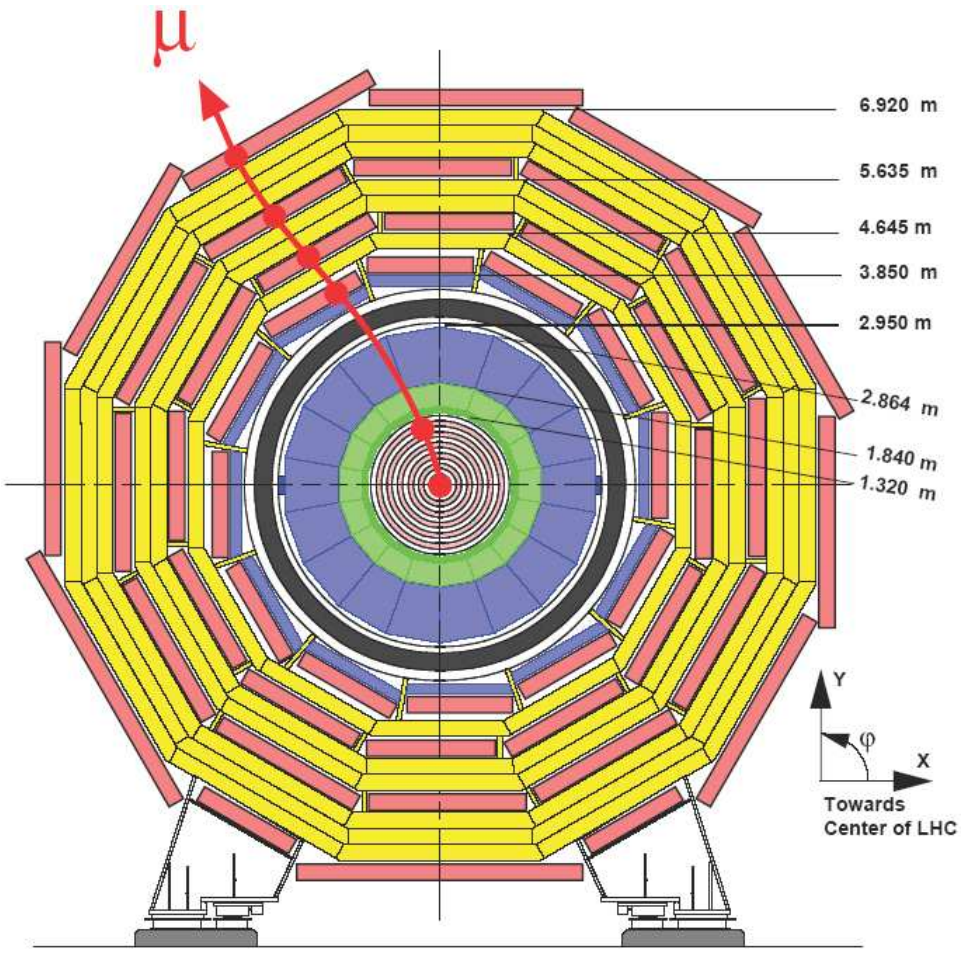

Figure 3.6: Side view of CMS showing the ϕ coordinate.

Table 3.1: CMS super-conducting solenoid parameters.

Field	4 T
Inner Bore	5.9 m
Length	12.9 m
Number of Turns	2168
Current	19.5 kA
Stored Energy	2.7 GJ

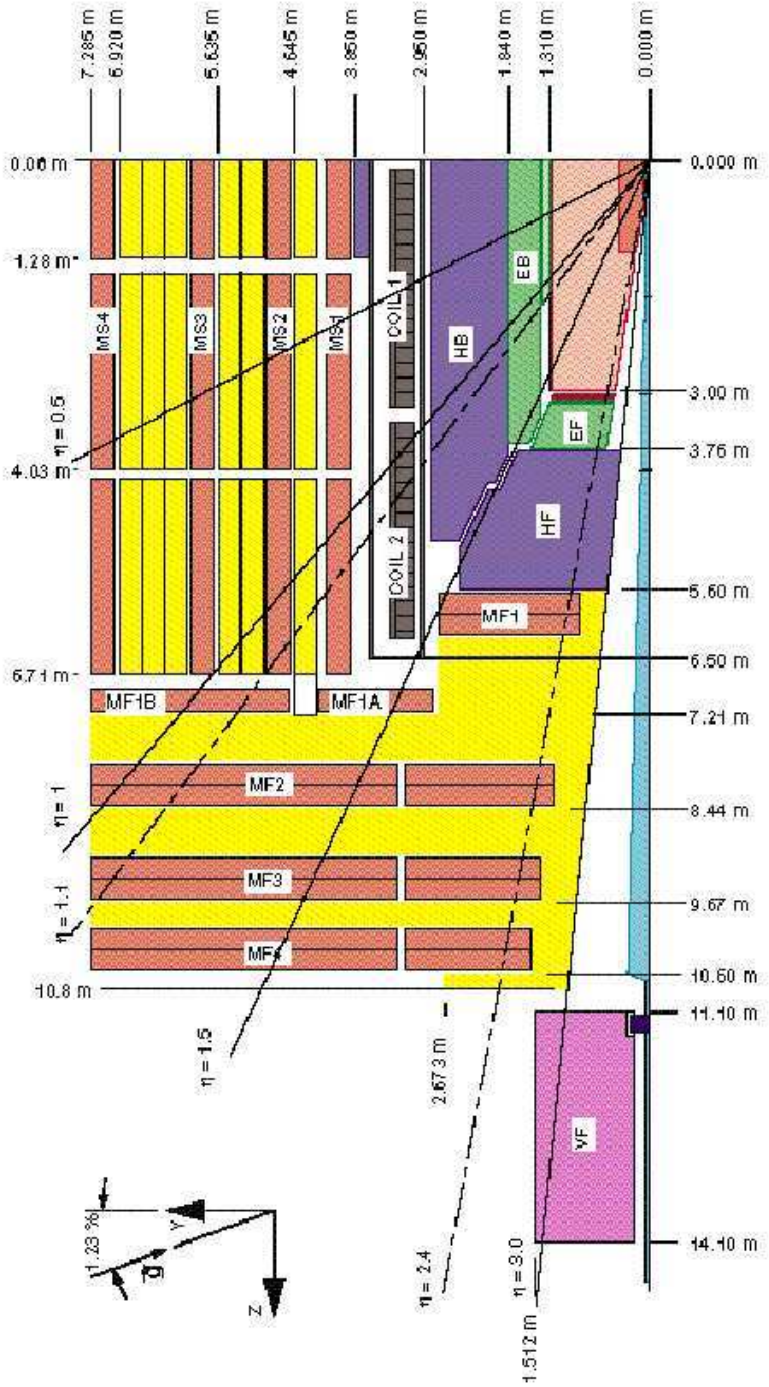

Figure 3.7: Quarter profile view of CMS showing the η coordinate.

3.2.3 Inner Tracking System

With its location being closest to the beam collision vertex, the tracker system is used to provide precise measurements of lepton and jet momenta at high resolution. Momentum measurements are important in order to define isolated physics objects such as e's, μ's, γ's, and τ's. Because heavy particles such as the c- and b- quarks have relatively long lifetimes, they can travel a measurable distance before decaying; for example, the D meson has $c\tau = 317$ micrometers. Such heavy flavored objects, which can decay hundreds of micrometers away from the primary interaction vertex, produce secondary vertices. The tracker system must be able to resolve these secondary vertices with sufficient precision to accommodate the identification of the decaying parent particle. The tracker must perform these functions while minimally interfering with the particles themselves; therefore, a minimal number of active detector layers are used such that good performance is ensured, but at the cost of a few radiation and interaction lengths[§].

Its close proximity to the primary collision vertex implies that the tracker must be radiation hard, as at full luminosity, over 1000 particles per bunch crossing are expected to traverse its volume. This high particle multiplicity also means that in order to achieve a minimal occupancy, which would allow for reasonable position resolution, a large number of detector channels must be used. The Tracker consists of three regions [40]:

At 10 cm $< r <$ 20 cm, Pixel detectors are used. The typical Pixel size is 100×150 μm^2 thus allowing for an occupancy of 10^{-4} particles/pixel/bx at 10 cm from the collision point. Designed to provide 3-dimensional positional information with high precision, the Pixel detector system is composed of 3 barrel and 4 endcap detector layers (Fig. 3.8).

[§]Because energy loss of a charged particle (from radiation) traversing a material is given by $\frac{dE}{dx} = \frac{E}{X_0}$, the "radiation length" can be understood as the length of material that reduces the mean

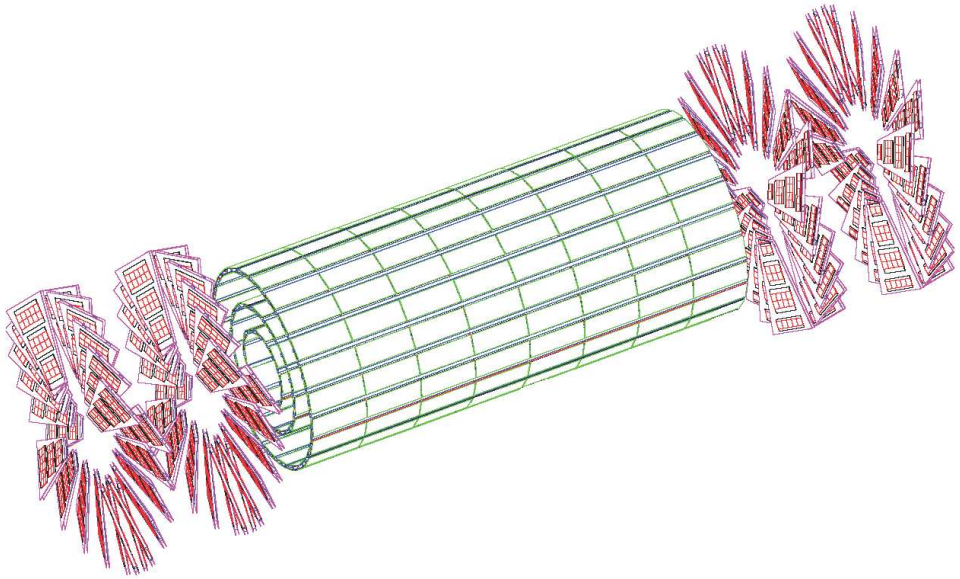

Figure 3.8: Schematic of the CMS Pixel detector.

The pixel detector system is built from an array of individual pixel modules. Each module is composed of a sensor layer bump bonded to the readout circuitry. The sensor layer is partitioned into individual pixel cells 150 × 150 μm^2 in size (Figures 3.9 and 3.10).

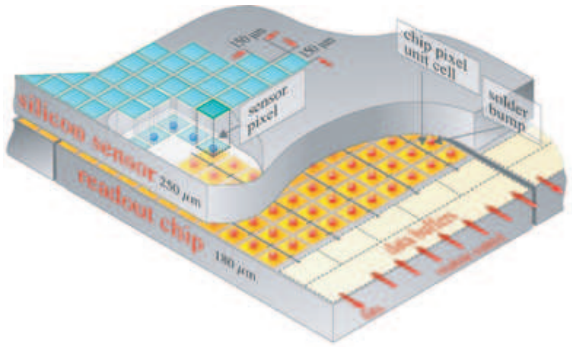

Figure 3.9: Diagram showing a pixel detector element.

The detection mechanism for the pixel detectors is shown in Figure 3.11. An potential difference is induced between the upper and lower surfaces of the pixel. As a charged particle traverses the p-type medium, electrons excited to the conduction

energy of a particle by a factor of e [39].

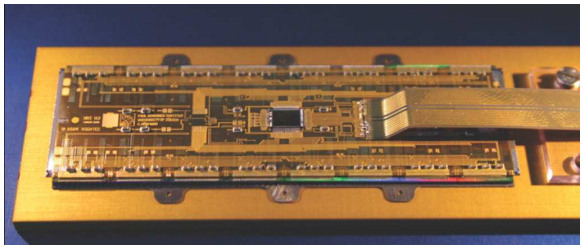

Figure 3.10: Photograph of a pixel detector module (courtesy CMS).

band drift towards the n-type pixels which act as collectors. In the barrel region, these electrons have a large dispersion angle (Lorentz angle) caused by the CMS magnetic field. This dispersion helps to distribute electrons to neighboring pixels which can improve the position resolution. The Silicon Microstrip detectors, described below, work in a similar manner.

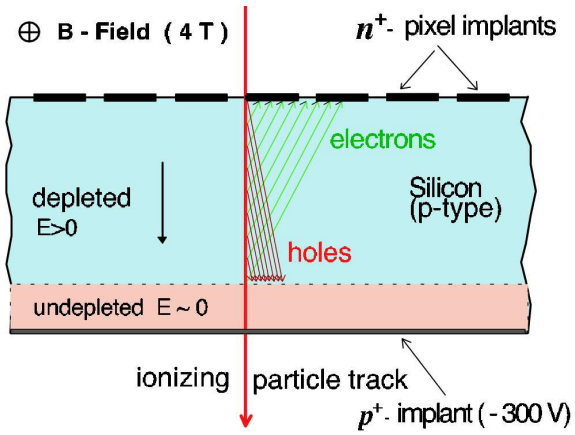

Figure 3.11: Diagram of demonstrating the pixel detector concept.

With its 15 μm resolution, vertex construction can be accomplished in 3-dimensions which allows b and τ-jets to be efficiently reconstructed. The barrel layers are positioned at an average distance of 4.4 cm, 7.3 cm, and 10.2 cm away from the beam axis, and have a total length of 53 cm. The endcaps are positioned at a distance $|z| = 34.5$ cm and $|z| = 46.5$ cm away from the collision region. The radial coverage is 6 cm $<$ r $<$ 15 cm away from the beam axis. Each endcap layer is composed of 24 wedges, rotated at 20° to benefit from the Lorentz effect, and so have a turbine-like geometry.

The barrel has a total of 768 pixel modules, while the endcap has 672 modules for a total of 1440. The pixels are bonded to readout circuits on readout chips which have a total of 52×53 pixels each. Thus, about 40 million pixel channels are read out for an active area of 0.92 m^2. The pixels can achieve an $r-\phi$ resolution of 10 μm and a z resolution of 20 μm over $|\eta| < 2.4$.

At 20 cm $< r <$ 55 cm, Silicon Microstrip detectors are used. The reduced flux is low enough such that the cell size can be increased to 10 cm $\times$ 80 μm, allowing a 2-3% occupancy/bx. The TIB (Tracker Inner Barrel) consists of 4 detector layers extending to $|z| <$ 65 cm. The TIB is built from 300 μm thick sensors, with 80-120 μm pitch, and 7-12.5 cm length. The first two layers provide stereo measurements, with an angle of 100 mrad, which allows for a $r-\phi$ resolution of 23-34 μm, and a z resolution of 23 μm.

At 55 cm $< r <$ 120 cm, more course Silicon Microstrips are used, with cell size of 25 cm x 180 μm, allowing a 1% occupancy (Fig. 3.12). The TOB (Tracker Outer Barrel) consists of six detector layers extending to $|z| <$ 110 cm, and uses 500 mm thick sensors with a strip pitch from 120 to 180μm. This coarse readout is acceptable because of the decreased particle flux. The first two layers provide stereo measurements. This layer can measure $r-\phi$ at a 35-52 μm resolution and a z resolution at 52 μm. The TEC (Tracker End-Cap) consists of nine large disks in the region 120 cm $< |z| <$ 280 cm along the beam axis.

The tracker is expected to reconstruct charged particles with $p_T > 1$ GeV/c, as particles below this threshold ("loopers") are expected to be bent such that they will not make it far enough in the r-direction to be detected by the pixels. Charged hadrons above this threshold are expected to be reconstructed with 85% efficiency. This efficiency will improve with higher p_T up to 95%. Muons will be reconstructed with an efficiency of better than 98% in the barrel region, while electrons will be reconstructed with an efficiency of 90%. The resolution of transverse momentum,

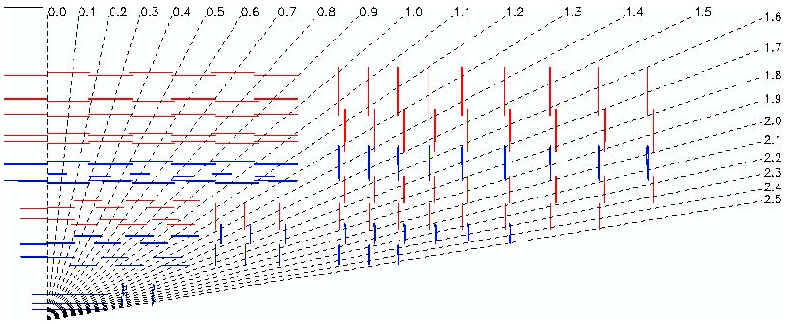

Figure 3.12: Quarter view of CMS strip detector layout.

transverse impact parameter, and longitudinal impact parameter for single muons is shown in Figure 3.13.

As of this writing, the silicon microstrip tracker system is scheduled to be delivered to point 5 at the beginning of 2007. The pixel system is expected to be delivered at the beginning of 2008.

3.2.4 Electromagnetic Calorimeter

Situated between the tracker system and the hadron calorimeter (Fig. 3.14), the Electromagnetic Calorimeter is designed to precisely measure electrons and photons using nearly 80,000 lead tungstate ($PbWO_4$) scintillating crystals (Fig. 3.15) covering the pseudorapidity range of $|\eta| < 3$ [41]. The high resolution performance of the ECAL system is dictated by the requirement to measure di-photon final states.

The ECAL crystals induce electromagnetic showers within their volume through Coulomb interactions between incoming electrons or photons and the nuclei of the crystal. This interaction causes a strong deflection in the path an incoming electron, which intern causes the electron to radiate photons (bremmstralung). These photons will then typically produce electron-positron pairs. These pairs then interact in the same manner as the initial electron. This propagation leads to an electro-

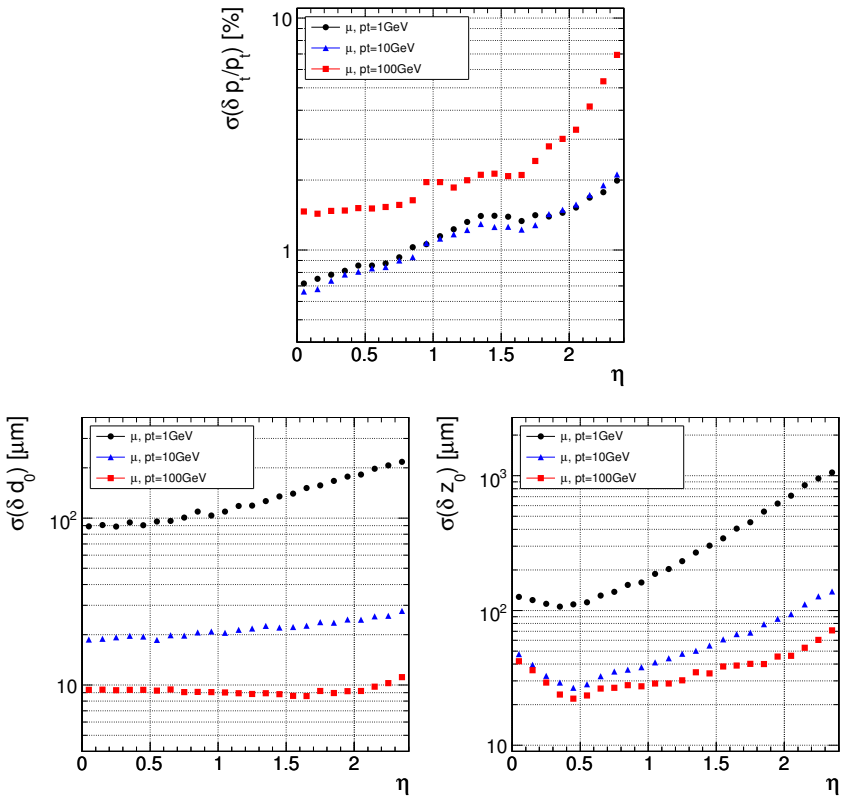

Figure 3.13: Resolution for single muons with transverse momenta 1, 10, and 100 GeV/c for: (upper) transverse momentum, (lower left) transverse impact parameter, and (lower right) longitudinal impact parameter [33].

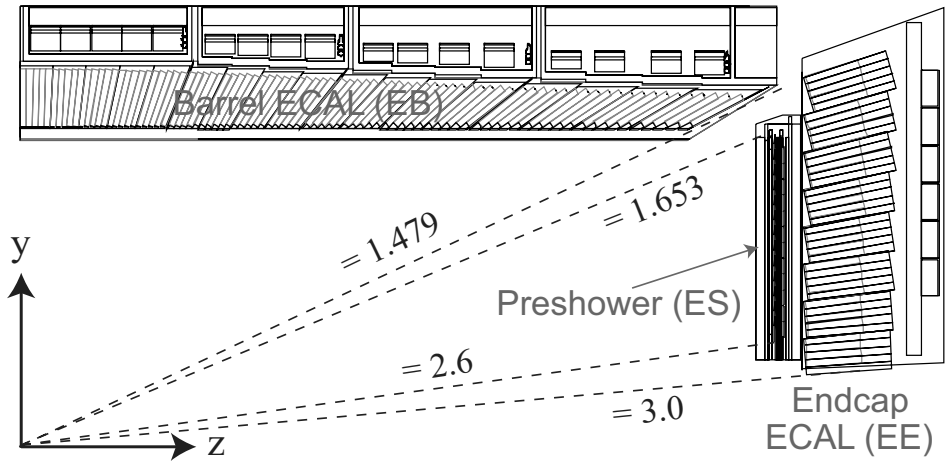

Figure 3.14: Quarter view of ECAL layout.

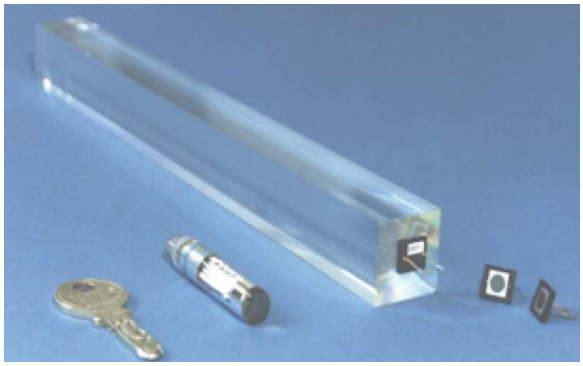

Figure 3.15: Photograph of a single ECAL crystal (courtesy CMS).

magnetic shower formation within the crystal (Fig. 3.16). Photons which initially enter the crystal volume initiate shower production in the a similar manner. As more particles are produced, the energy per new particle decreases until finally particle pair-production stops, and most of the energy is absorbed by the crystal resulting in light emission that is collected by detectors at the end of the crystal [39]. The light yield is proportional the initial energy of the incoming particle.

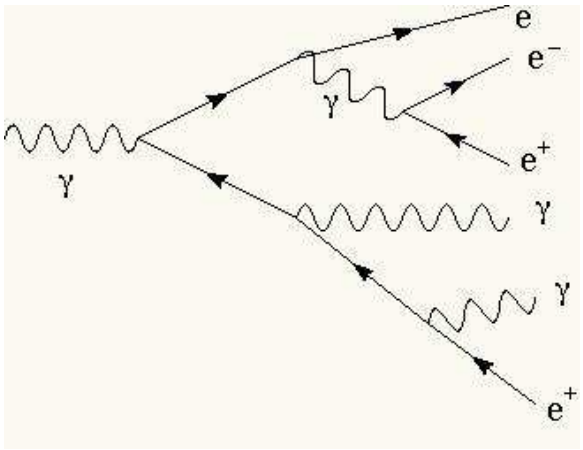

Figure 3.16: Diagram of an electromagnetic shower developing from an initial photon.

The ECAL crystals have a short radiation length (X_0 = 0.89 cm), a Moliere radius[¶] (2.2 cm), and are about 23 cm long. This allows narrow electromagnetic showers to form in the crystals, of which 99% of the energy is contained therefore

[¶]In an electromagnetic shower, the Moleire radius R_M characterizes the transverse shower size [39].

making a very small ECAL system overall with good energy and position resolution (Fig. 3.17). These crystals work well with the LHC timing structure as 85% of the light is emitted in 20 ns. In the barrel region, the ECAL crystals have an area of 20.5×20.5 mm^2 (or $\Delta\eta \times \Delta\phi = 0.014 \times 0.014$) facing the radial direction, while in the endcap, they range from 27×29 mm^2 to 18×20 mm^2 ($\Delta\eta \times \Delta\phi = 0.05 \times 0.05$).

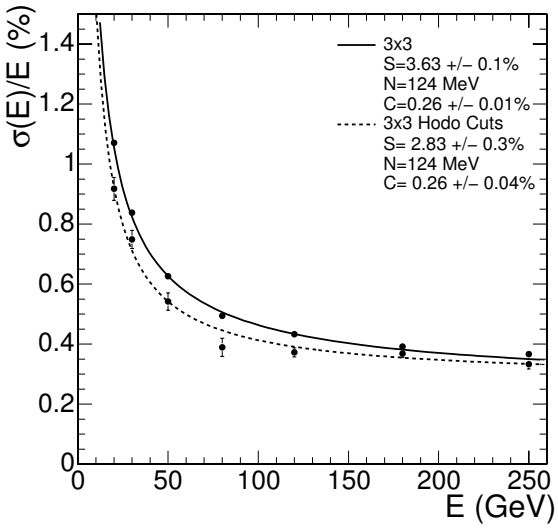

Figure 3.17: ECAL supermodule energy resolution as a function of electron energy entering a 3×3 array of crystals [33].

In order to enhance the ability to separate π^0's from γ's, CMS employs a preshower detector in front of the ECAL crystals in the forward region ($1.65 < |\eta| < 2.6$). This detector contains two lead converters. Each lead converter layer is followed by a plane of silicon strip detectors with a pitch of 1.9 mm. π^0's can be distinguished from γ's by examining the charge distribution of along the detector strips as di-γ production from π^0 decays should result in broad charge distributions on the strip detectors.

As of this writing, nearly 80% of the ECAL crystals have been delivered. More than half of the 36 ECAL "supermodules" have been assembled and calibrated. Two supermodules have been installed for use during the MTCC.

3.2.5 Hadron Calorimeter

In between the ECAL system and the superconducting solenoid sits the Hadron Calorimeter system [42]. The HCAL system works in concert with the ECAL system to provide full coverage up to $|\eta| < 5$ and to measure the energy and direction of particle jets caused by quarks and gluons, as well as missing transverse energy caused by neutrinos[‖] (or other exotic phenomena).

Much like the ECAL, the HCAL system relies on shower development and energy absorption to detect the initial incoming particles [39]. Because the incoming hadrons lose energy primarily through strong interaction with the nuclei of the absorber material, the HCAL system must be much larger than ECAL. The HCAL system is a sampling calorimeter which consist of 4 mm thick plastic scintillator tiles with wavelength-shifting fiber readout, interleaved with 5 cm thick brass absorber plates (Fig. 3.18).

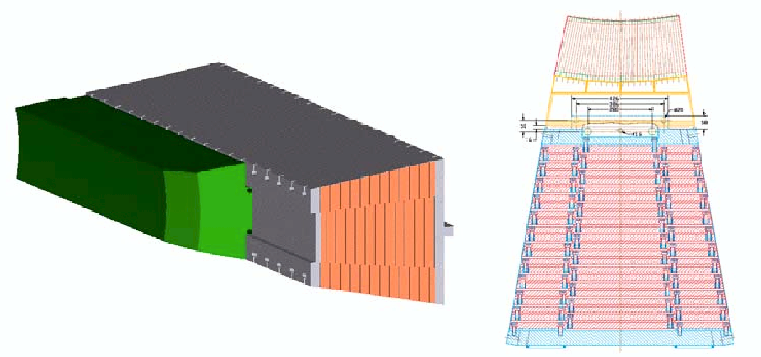

Figure 3.18: Schematic wedge used to build up barrel region of the HCAL system.

As a hadronic shower passes through each layer of absorber, more energy is lost which is then measured by the subsequent scintillator layer. The total energy collected by the scintillators is then proportional to that of the initial incoming hadron. A

[‖]Missing transverse energy is measured by taking the negative vector sum of the calorimeter energy content in the $x-y$ plane. This quantity is important in hadron collisions as the total initial transverse energy in hadron beam collision is considered a conserved quantity (whose initial state is $\vec{0}$); therefore, the missing transverse energy indicates invisible particle content.

granularity of $\Delta\eta \times \Delta\phi = 0.087 \times 0.087$ is used in the barrel region $|\eta| < 2$ (Fig. 3.19). This granularity is suitable for good di-jet separation and mass resolution. In the endcap region, $1.3 < |\eta| < 3.0$, the η granularity ranges from 0.087 to 0.35, while the ϕ segmentation ranges from 0.087 to 0.175 radians (Fig. 3.20).

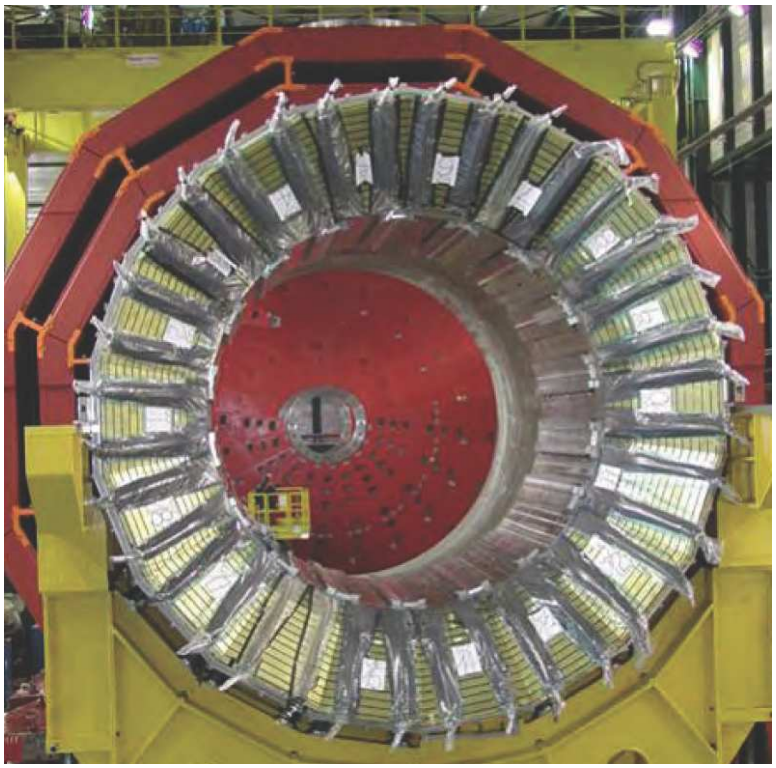

Figure 3.19: Photograph of barrel portion of the HCAL detector with individual wedges clearly visible (courtesy CMS).

In the region $|\eta| < 1.4$, CMS has an hadron outer calorimeter which sits outside of the solenoid and serves to measure the low-energy tails that result from late developing or highly energetic showers which are not contained by the barrel HCAL. This detector helps ensure a robust energy measurement.

In order to give full geometrical coverage of the calorimeter system, enabling the reconstruction of very forward jets, a separate forward calorimeter system is used in the region $3 < |\eta| < 5$. It is a located 11 m away from the interaction region. This detector uses a steel absorber with embedded quartz fibers which act as the active material.

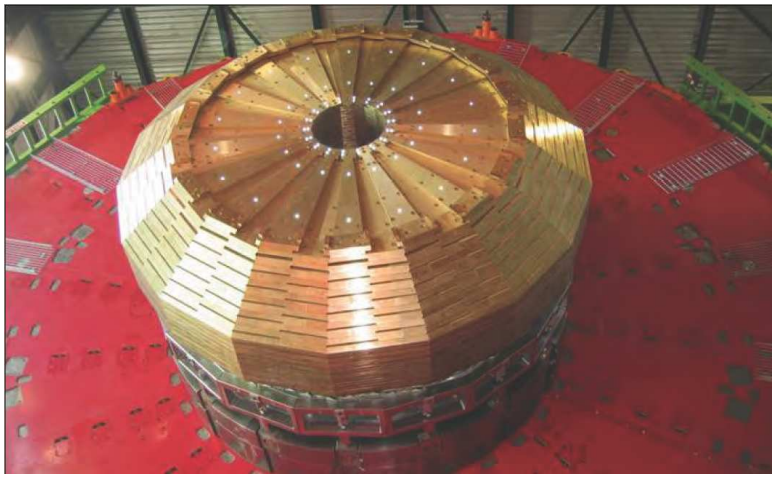

Figure 3.20: Photograph of the endcap portion of the HCAL detector (courtesy CMS).

As of this writing, the HB portion of the HCAL system has been inserted into the solenoid. Part of this system will participate in the MTCC. The endcap modules have also been assembled.

3.2.6 Muon System

Muons will provide a clean signature of interesting physics at the LHC as they are often in the final states of heavy particle decays and minimally interact with inner detector systems; therefore, CMS has an extremely robust muon system. The CMS muon system efficiently identifies muons up to $|\eta| < 2.4$ and measures their momenta with good resolution (Fig. 3.21). Its fast detector response and custom electronics allow this system to provide CMS a with very efficient muon trigger [43].

The muon system is composed of a barrel and endcap system, each with four layers (or stations). The outer volume of CMS is instrumented with muon detectors mounted on to the iron support structure that also serves as the return yoke for the 4 T magnetic field.

Because of the low occupancy in the barrel region and a near uniform magnetic field, the barrel region of the muon system uses drift tubes (Fig. 3.22). The drift tubes are drift chambers filled with a gas mixture of Ar-CO_2. They have 1.2 mm thick aluminum cathodes, as well as stainless steel anode wires strung along the center of

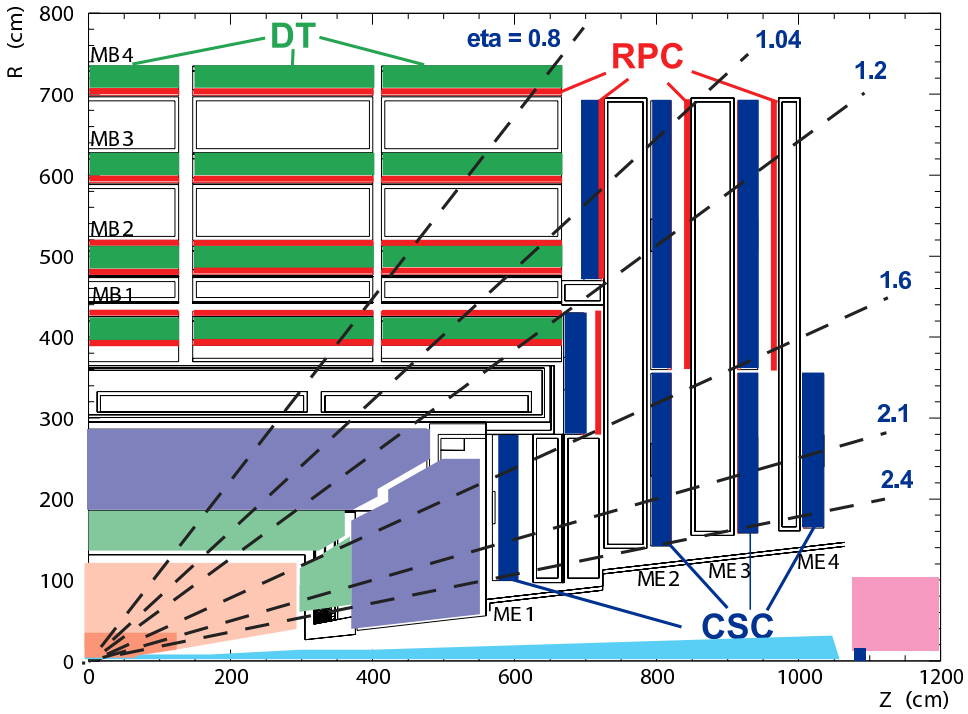

Figure 3.21: Quarter view showing Muon System.

the tube. As muons traverse the gas volume, the free electrons liberated from the gas drift toward the anode wires which provide the signal information for the detector. By knowing the drift velocity and drift time, the position of an incoming particle's distance from the anode wire can be reconstructed. These detectors are capable of a spatial resolution better than 250 μm, and have a timing resolution of about 5 ns, which is adequate for bunch crossing identification.

With higher particle rates and a non-uniform magnetic field, the endcap region employees cathode strip chamber technology. The endcap region consists of four stations of Cathode Strip Chambers (CSC). These are Ar-CO_2-CF_4 filled multiwire proportional chambers providing CMS complete azimuth coverage (in ϕ), as well as $0.9 < |\eta| < 2.4$. Six cathode strip and anode wire layers compose a single station in the endcap system. The chambers are trapezoidal in shape, extending 10° or 20° in ϕ, and are composed of cathode strips aligned radially from the beam axis, and gold

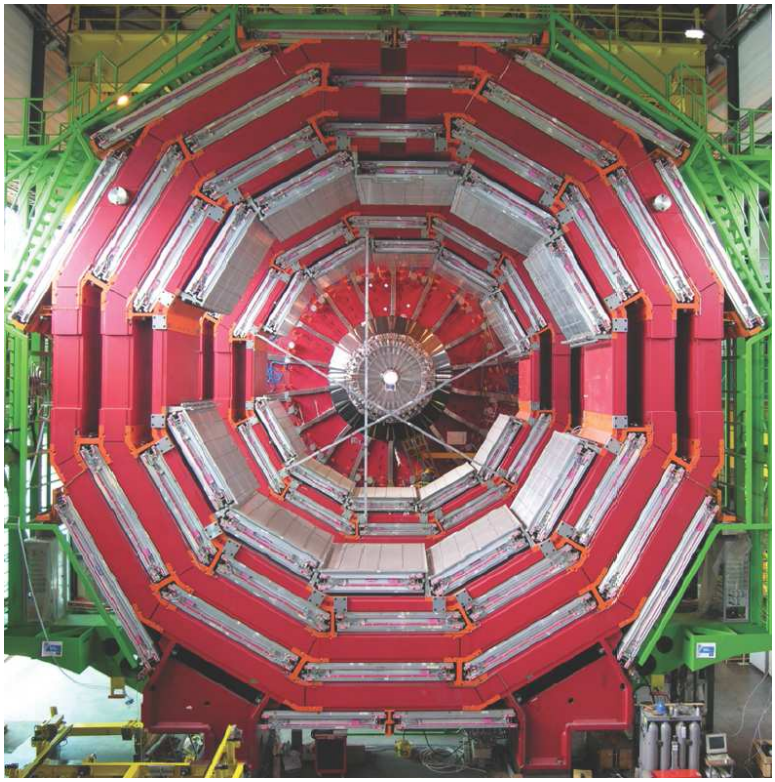

Figure 3.22: Photograph of Drift-tube detectors in the barrel region (courtesy CMS).

plated anode wires aligned in the orthogonal direction. These chambers are arranged to form a complete disk (Fig. 3.23).

A muon entering the gas volume of a CSC will caused ionization. The resulting electrons will accelerate towards the anode wires causing a charge avalanche. These electrons are then collected by the anode wires, inducing an image charge on the cathode strips. By interpolating the charge distribution between neighboring strips, a precise measurement of the ϕ coordinate can be made (Fig. 3.24). The anode signals provides fast timing information and a course measurement of the η coordinate. These chambers are typically able to provide a spatial resolution of about 200 μm (100 μm for the chambers on the inner most ring closest to the interaction region). The ϕ resolution is $\mathcal{O}$(10 mrad).

The barrel and endcap regions will also contain Resistive Plate Chambers (RPCs), used to provide additional timing information ($\sim$ 1 ns) to service the trigger system

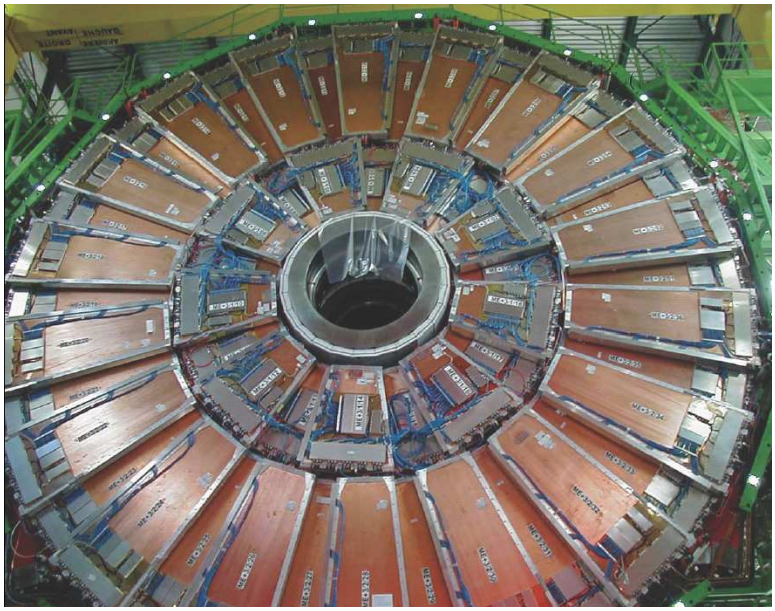

Figure 3.23: Photograph of one station of the endcap muon system (courtesy CMS).

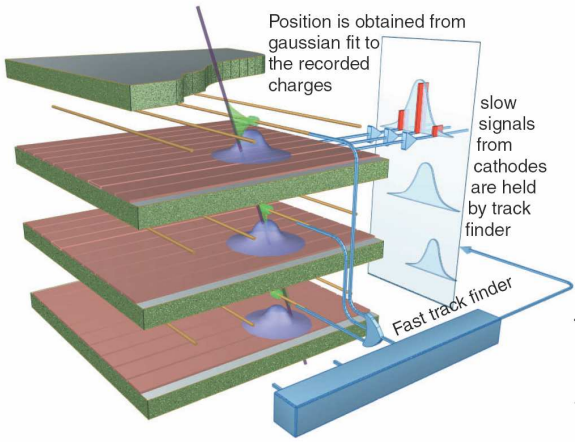

Figure 3.24: Cartoon illustrating the concept of CSC design.

and provide additional muon detection capabilities. A RPC is made from two parallel plates with high bulk resistivity, separated by a gas gap a few millimeters wide. Electrodes are formed by the outer surfaces of the plates, which are coated with a conductive graphite paint. The detector signal is produced when an electron avalanche, induced by incoming muons crossing the gas region, drifts toward the anode, thus inducing an image charge on the readout cathodes.

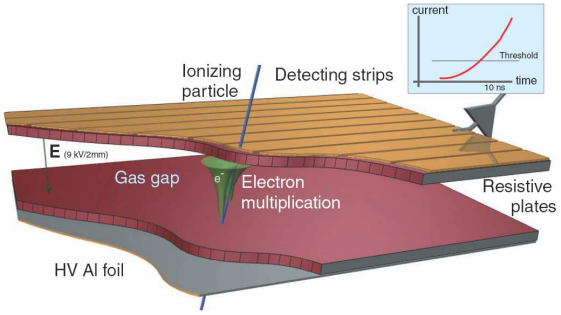

Figure 3.25: Cartoon illustrating the concept of RPC design.

Figure 3.26 shows the muon momentum resolution achievable by CMS.

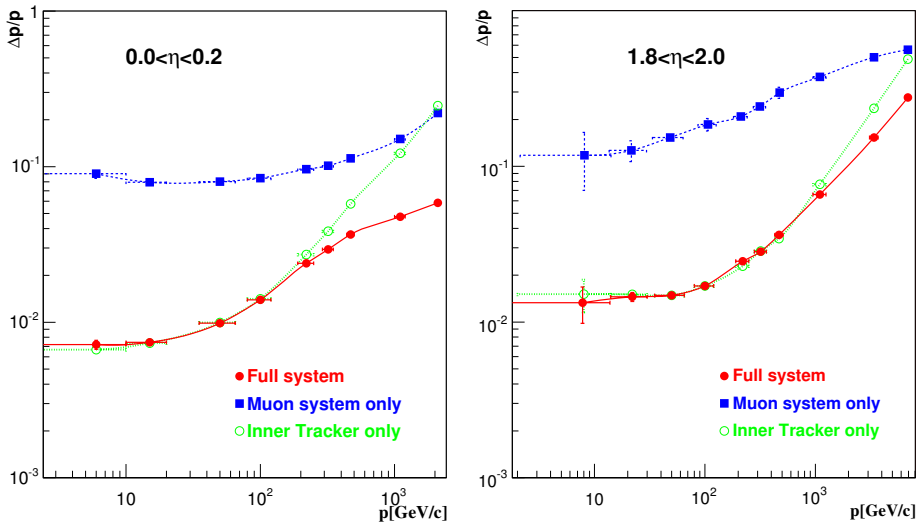

Figure 3.26: Muon momentum resolution versus momentum for (left) the barrel and (right) the endcap regions [33].

As of this writing, nearly 90% of the muon detectors have been installed. A slice of this system will participate in the MTCC.

3.3 CMS Trigger System

At full luminosity, the LHC collisions will result in an enormous amount of detector data (approximately 40 TB/s) from the near 10^9 interactions per second. At CMS three levels of trigger systems are implemented to reduce the data bandwidth to a manageable 100 MB/s. While the trigger system forms its decision for a particular collision, the collision event detector data is held in memory and is ultimately sent to permanent storage upon the formation of a positive trigger decision.

The Level-1 Trigger must reduce the data rate to $\mathcal{L}(100\text{ kHz})$ in 3.2 μs (128 proton bunch-crossings). This trigger is based on custom electronics, and forms its decision with no dead-time by identifying muons, electrons, photons, jets, and missing transverse energy with the lowest possible thresholds while satisfying the Level-1 rate requirement. The High-Level Trigger (HLT) is based on commercial processors and uses the full resolution avaliable from the detectors to further reduce the rate to 100 Hz.

3.3.1 Level-1 Trigger

The first trigger level (Level-1) reduces the data size by a factor of 400 in just 3.2 μs. The algorithms employed to facilitate this reduction are executed by custom electronics, and are motivated by knowledge of the standard model, as well as particular physics processes and decay channels of interest such as new physics phenomena that result in high-p_T decay products. Only the calorimeters and muon system participate in the Level-1 trigger system, which provide fast reconstruction of muons, electrons, taus, jets, and missing transverse energy using coarse detector data.

While the Level-1 decision is being formed, the full precision detector data is held in a pipeline. Every 25 ns, a new event is received by the Level-1 system. The Level-1 Trigger decision is determined by its two detector subsystems: the Level-1 calorimeter

trigger and the Level-1 muon trigger, while the tracker system does not participate in the Level-1 Trigger formation (Fig. 3.27).

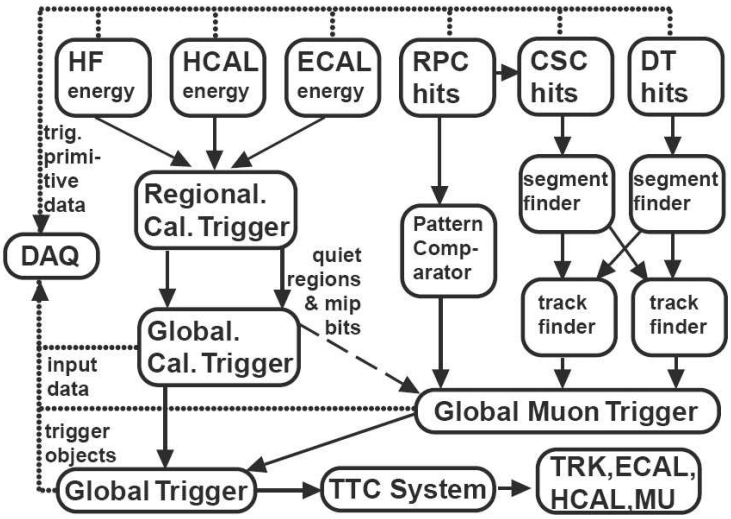

Figure 3.27: Overview of Level-1 Trigger system [31].

Using the HCAL and ECAL systems, the Calorimeter trigger sends the best candidate isolated and non-isolated e/γ objects, τ-jet objects, and forward and central jets, as well as the sum of transverse energy (ΣE_T) and missing transverse energy ($\not{E}_T$) of the event to the Global Trigger each event. Additional information is used in conjunction with the Global Muon Trigger to identify isolated muons.

The Global Muon Trigger accepts the best muon candidate tracks formed by the Resistive Plate Chamber, the Barrel Muon Drift Tube, and the Cathode Strip Chamber systems. The tracks provided by these systems must be placed into a common (η,ϕ) coordinate space and P_T scale. Using information from the Calorimeter trigger, isolated muons are also found. A final list of the four best muons are sent to the Global Trigger. Figure 3.28 shows the simulated single- and di- muon trigger rates for various muon P_T thresholds.

The Global Trigger uses a logical combination of the Calorimeter and Global Muon triggers. The Global Trigger processes the list of objects passed to it by the lower level trigger systems, applies thresholds, and passes the final Level-1 accept command

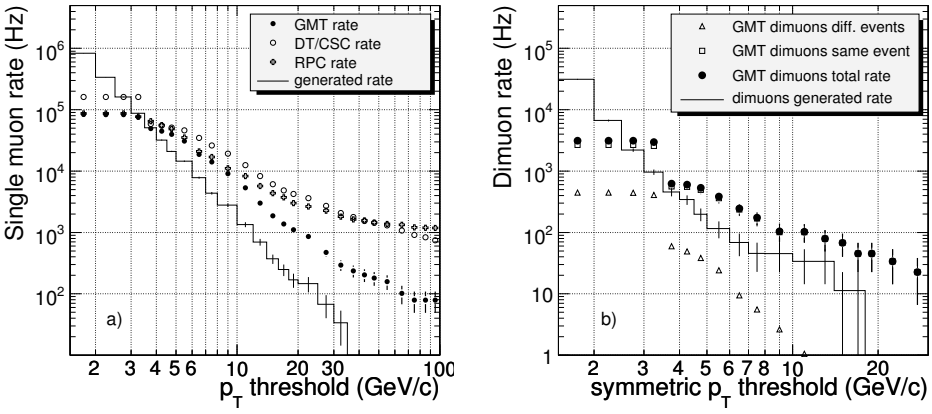

Figure 3.28: Simulated Level-1 Trigger rate for $\mathcal{L} = 2 \times 10^{33}$ cm^{-2}s^{-1}. a) shows the single-muon rate and b) shows the di-muon trigger rate as a function of transverse momentum threshold [33].

to the Trigger, Timing, and Control ystem (TTC). These thresholds (defined in the "trigger menu") are determined by the needs and requirements of the experiment. A possible Level-1 trigger menu for low luminosity conditions is shown in Table 3.2 [30].

3.3.2 High Level Trigger

The High-Level Trigger (HLT) is composed of two trigger levels. The Level-2 Trigger is executed on commercial processors. This stage uses full precision detector data from the muon and calorimeter systems to reconstruct the physics objects. Its input data rate is reduced by a factor of 10 compared to the Level-1 Trigger. The Level-3 Trigger uses additional information from the tracker system to fully reconstruct the event and is therefore more time consuming. This allows an additional rate reduction to 100 Hz. By using a commercial processor farm, the HLT system is extremely flexible, and is ultimately more cost effective than using a system based on custom electronics. Because the HLT is software based, the reconstruction algorithms used to identify physics objects from the high-quality detector data can be the same as that used for offline analysis.

The HLT uses regional reconstruction whereby physics objects are reconstructed based on detector data originating from regions of interest as identified by the Level-1

Table 3.2: The Level-1 Trigger Menu at $\mathcal{L} = 2 \times 10^{33}$ cm^{-2}s^{-1}. Individual and cumulative rates are given for the different trigger paths and selected kinematic thresholds.

Trigger	Level-1 Threshold (GeV)	Level-1 Rate (kHz)	Cumulative Level-1 Rate (kHz)
Inclusive $e\,\gamma$	22	3.9 ± 0.3	3.9 ± 0.3
Double $e\,\gamma$	11	1.0 ± 0.1	4.6 ± 0.3
Inclusive μ	14	2.5 ± 0.2	7.1 ± 0.3
Double μ	3	4.0 ± 0.3	11.0 ± 0.4
Inclusive τ	100	2.2 ± 0.2	12.9 ± 0.5
Double τ	60	3.0 ± 0.2	14.9 ± 0.5
1-,2-,3-,4-jets	150,100,70,50	2.2 ± 0.2	15.8 ± 0.5
H_T	275	2.0 ± 0.2	16.2 ± 0.5
$\not\!\!E_T$	60	0.4 ± 0.1	16.3 ± 0.5
H_T+ $\not\!\!E_T$	200, 40	1.1 ± 0.1	16.6 ± 0.5
jet + $\not\!\!E_T$	100, 40	1.1 ± 0.1	16.7 ± 0.5
τ + $\not\!\!E_T$	60, 40	2.7 ± 0.2	18.8 ± 0.5
μ + $\not\!\!E_T$	5, 30	0.3 ± 0.1	19.0 ± 0.6
$e\,\gamma$ + $\not\!\!E_T$	15, 30	0.5 ± 0.1	19.1 ± 0.6
μ + jet	7, 100	0.2 ± 0.1	19.1 ± 0.6
$e\,\gamma$ + jet	15, 100	0.6 ± 0.1	19.2 ± 0.6
μ + τ	7, 40	1.2 ± 0.1	19.8 ± 0.6
$e\,\gamma$ + τ	15, 60	2.6 ± 0.2	20.5 ± 0.6
$e\,\gamma$ + μ	15, 7	0.2 ± 0.1	20.5 ± 0.6
Prescaled			22.3 ± 0.6
Total Level-1 Rate			22.3 ± 0.6

Trigger. A detailed description of single- and di-μ triggering is provided below. A possible High-Level trigger table for low luminosity conditions is shown in Table 3.3. This work uses event samples selected by two HLT triggers, the inclusive single-muon and the di-muon triggers; these triggers are described in more detail below.

3.3.3 Single-muon trigger

A single-muon inclusive trigger is formed by requiring that either (1) in the endcaps, low quality Level-1 cathode strip chamber (CSC) tracks be matched with resistive plate chambers (RPC) tracks by the Global Muon Trigger and at least one Level-2 muon be reconstructed with a valid extrapolation to the collision vertex, or (2) in the barrel, at least one drift tube (DT) track segment be reconstructed with

the sum of the number of DT segments and RPC hits greater than three. At Level-3, a muon must have more than five tracker hits. Finally, for the HLT, the Level-2 muon must satisfy calorimeter isolation (at the 97% efficiency point), and the Level-3 muon must satisfy the tracker isolation (at the 97% efficiency point). For low-luminosity running, the single-muon trigger p_T threshold is set at Level-1 to be 14 GeV/c, corresponding to 2.7 kHz and 95% efficiency, and at HLT to be 19 GeV/c, corresponding to 25 Hz and 90% efficiency.

3.3.4 Di-muon Trigger

A di-muon trigger is formed by the same criteria as for the single-muon trigger, but the isolation criteria are relaxed so that only one of the two muons need satisfy it. Further, at Level-3, both muons are required to originate from the same vertex (within 5 mm) and di-muons which are close in space/momentum ($\Delta\phi < 0.05$ radians, $\Delta\eta < 0.01$, $\Delta p_T < 0.1$ GeV/c) are rejected to remove ghost tracks which may result from a single muon resulting in two reconstructed muon tracks. For low-luminosity running, the symmetric p_T threshold for the di-muon trigger is lowered at Level-1 to be 3 GeV/c, corresponding to a rate of 0.9 kHz and 95% efficiency, and at HLT to be 7 GeV/c, corresponding to a rate of 4 Hz and 90% efficiency.

Table 3.3: The High-Level Trigger Menu at $\mathcal{L} = 2 \times 10^{33}$ cm^{-2}s^{-1} for an output of approximately 120 Hz. The transverse energy values are the kinematic thresholds for the different trigger paths.

Trigger	Level-1 bits used	Level-1 Prescale	HLT Threshold (GeV)	HLT Rate (Hz)
Inclusive e	2	1	26	23.5 ± 6.7
e-e	3	1	12, 12	1.0 ± 0.1
Relaxed e-e	4	1	19, 19	1.3 ± 0.1
Inclusive γ	2	1	80	3.1 ± 0.2
γ-γ	3	1	30, 20	1.6 ± 0.7
Relaxed γ-γ	4	1	30, 20	1.2 ± 0.6
Inclusive μ	0	1	19	25.8 ± 0.8
Relaxed μ	0	1	37	11.9 ± 0.5
μ-μ	1	1	7, 7	4.8 ± 0.4
Relaxed μ-μ	1	1	10, 10	8.6 ± 0.6
$\tau + \not{E}_T$	10	1	65 ($\not{E}_T$)	0.5 ± 0.1
Pixel τ-τ	10, 13	1	—	4.1 ± 1.1
Tracker τ-τ	10, 13	1	—	6.0 ± 1.1
$\tau + e$	26	1	52, 16	< 1.0
$\tau + \mu$	0	1	40, 15	< 1.0
b-jet (leading jet)	36, 37, 38, 39	1	350, 150, 55	10.3 ± 0.3
b-jet (2$^{\text{nd}}$ leading jet)	36, 37, 38, 39	1	350, 150, 55	8.7 ± 0.3
Single-jet	36	1	400	4.8 ± 0.0
Double-jet	36, 37	1	350	3.9 ± 0.0
Triple-jet	36, 37, 38	1	195	1.1 ± 0.0
Quadruple-jet	36, 37, 38, 39	1	80	8.9 ± 0.2
$\not{E}_T$	32	1	91	2.5 ± 0.2
jet + $\not{E}_T$	32	1	180, 80	3.2 ± 0.1
acoplanar 2 jets	36, 37	1	200, 200	0.2 ± 0.0
acoplanar jet + $\not{E}_T$	32	1	100, 80	0.1 ± 0.0
2 jets + $\not{E}_T$	32	1	155, 80	1.6 ± 0.0
3 jets + $\not{E}_T$	32	1	85, 80	0.9 ± 0.1
4 jets + $\not{E}_T$	32	1	35, 80	1.7 ± 0.2
Diffractive	Sec. **??**	1	40, 40	< 1.0
H_T+ $\not{E}_T$	31	1	350, 80	5.6 ± 0.2
H_T+ e	31	1	350, 20	0.4 ± 0.1
Inclusive γ	2	400	23	0.3 ± 0.0
γ-γ	3	20	12, 12	2.5 ± 1.4
Relaxed γ-γ	4	20	19, 19	0.1 ± 0.0
Single-jet	33	10	250	5.2 ± 0.0
Single-jet	34	1 000	120	1.6 ± 0.0
Single-jet	35	100 000	60	0.4 ± 0.0
Total HLT rate				119.3 ± 7.2

CHAPTER 4
LEVEL-1 ENDCAP MUON TRIGGER SYSTEM

The Level-1 trigger receives trigger decisions form both the calorimeter and muon systems. The muon system trigger decision is derived from the Global Muon Trigger (GMT) which uses data from at most four reconstructed muons reported from the barrel and endcap portions of the trigger.

The challenge for the CSC muon trigger is to report muon candidates with the lowest possible p_T threshold, and yet maintain a single muon trigger rate below 1 kHz/η at full LHC luminosity. Therefore, the CSC muon trigger must reconstruct tracks using the reduced granularity data given in the trigger stream, with the best possible resolution (Fig. 4.1) in order to prohibit fakes. This task is made difficult because reconstructing muons from physically interesting heavy object decays admits a large muon background associated with heavy quark decays, decays of π's and K's, hadronic punch-through, beam halo, cosmic rays, and the large neutron background that results in $\gamma \rightarrow e^+e^-$ processes within muon detectors. These backgrounds can result in both legitimate muon tracks through the detector volume as well as random muon track-segments formed in the muon detectors, both of which can lead to muon track reconstruction. The background rate must be controlled by taking advantage of its decreasing spectrum as a function of muon p_T. This allows the trigger rate to be effectively throttled by the p_T trigger threshold. The rate can also be controlled by restricting the patterns of detector hits from which reconstructed muon tracks are formed. By restricting these patterns, the trigger threshold can be lowered such that events with prompt muons from heavy decays such as from W's might be stored. The endcap muon track-finding system was designed and tested by the University of

Florida: this work accounts for much of the time and effort spent over the last few years by professors, engineers, and students who are involved with the project at the University of Florida. The design and numerous tests of the track-finding system are described below.

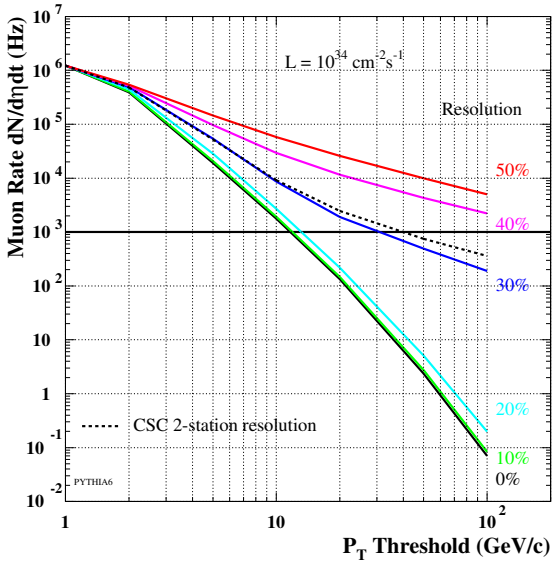

Figure 4.1: Example of Level-1 single muon rate per unit rapidity from the CSC as a function of transverse momentum threshold for possible reconstruction resolutions [44].

In the endcap system, muon track-finding is electronically partitioned into six 60° sectors in each endcap (Fig. 4.2) covering $0.9 < |\eta| < 2.4$. A Sector Processor (SP) unit is used in each sector to form muon tracks within its ϕ boundaries. A single SP receives trigger primitives from front-end electronics, which sit on or near the CSCs (Fig. 4.3). The front-end electronics form Local Charged Tracks (LCTs) from the six detector layers of a station. The cathode and anode LCT (CLCT and ALCT) trigger cards search for valid patterns in the anode wire and cathode strip planes of a CSC. The ALCT provides precise timing and η position data, while the CLCTs use comparators to localize hit clusters to within a half-strip for each of the six chamber layers, which is used to calculate ϕ. A Trigger Mother Board (TMB) card combines the ALCT and CLCT data from a given chamber by associating wire data to cathode

data along with a bunch-crossing time. The TMB sends the best two LCT candidates to a Muon Port Card (MPC). The Muon Port Card (MPC) collects all of the LCTs (up to 18) for a given station within a sector, sorts them, and sends the best three to an SP via optical fibers. A single SP collects LCTs sent via fifteen 1.6 Gbit/s optical links, and is responsible for linking LCTs in ϕ and η in order to form full tracks, and to report the transverse momentum (p_T), ϕ, and η for each full track. The entire Track-Finding processor is composed of twelve such SPs housed in a single 9U VME* crate (Fig. 4.4) [33].

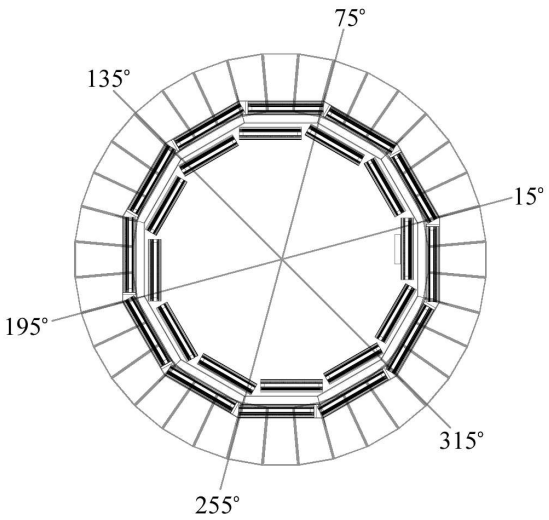

Figure 4.2: Diagram end-cap muon sectors.

4.1 Muon Track-Finding in the Endcap Region

The principle of the TF logic [31] is illustrated in Figure 4.5. The Track-Finder searches in η and ϕ roads for LCTs received within a three bunch-crossing window that are consistent with a muon trajectory through the endcap. By measuring the sagitta induced by the magnetic field, a p_T measurement can be made.

*Versa Module Europe bus provides an IEEE standard used for communication between electronic modules. This allows engineers the freedom to design hardware modules with the assurance of a standard interface for data flow [45].

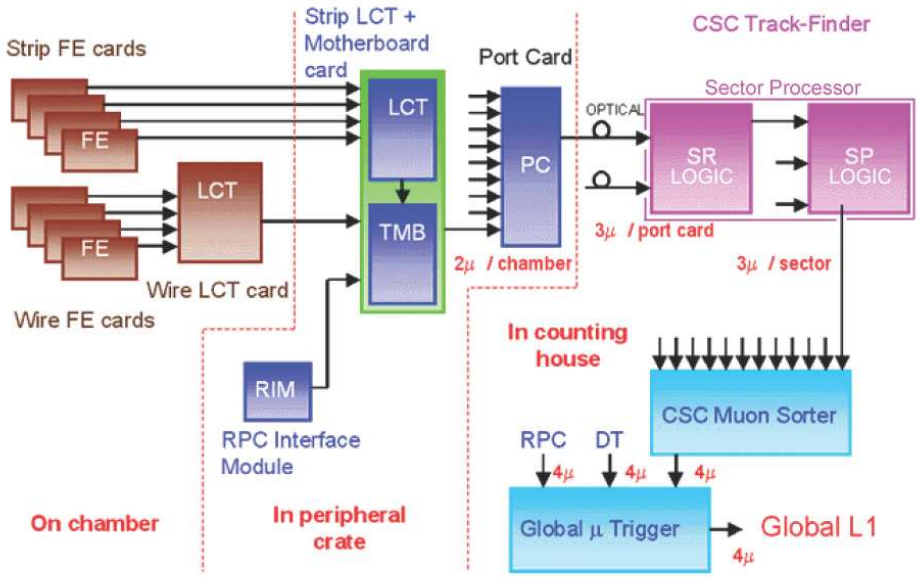

Figure 4.3: Architecture of the Level-1 CSC trigger.

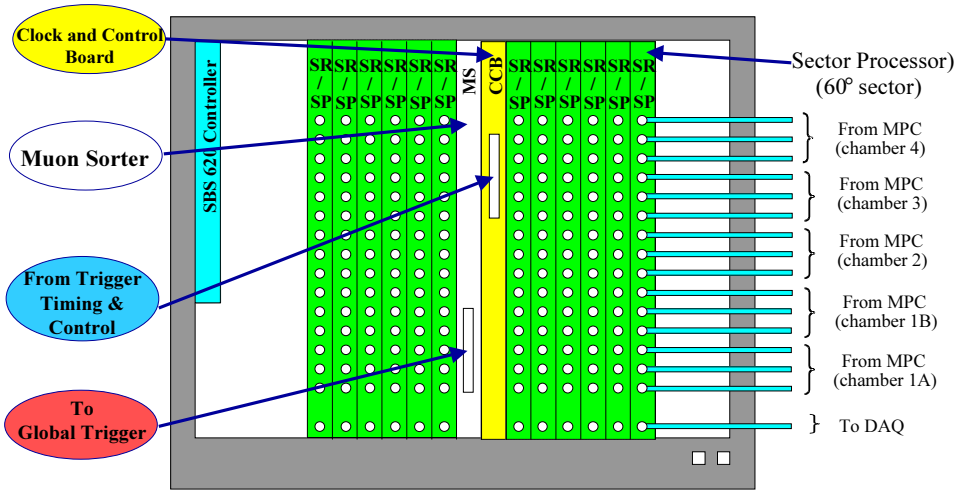

Figure 4.4: Diagram showing Track-Finder layout.

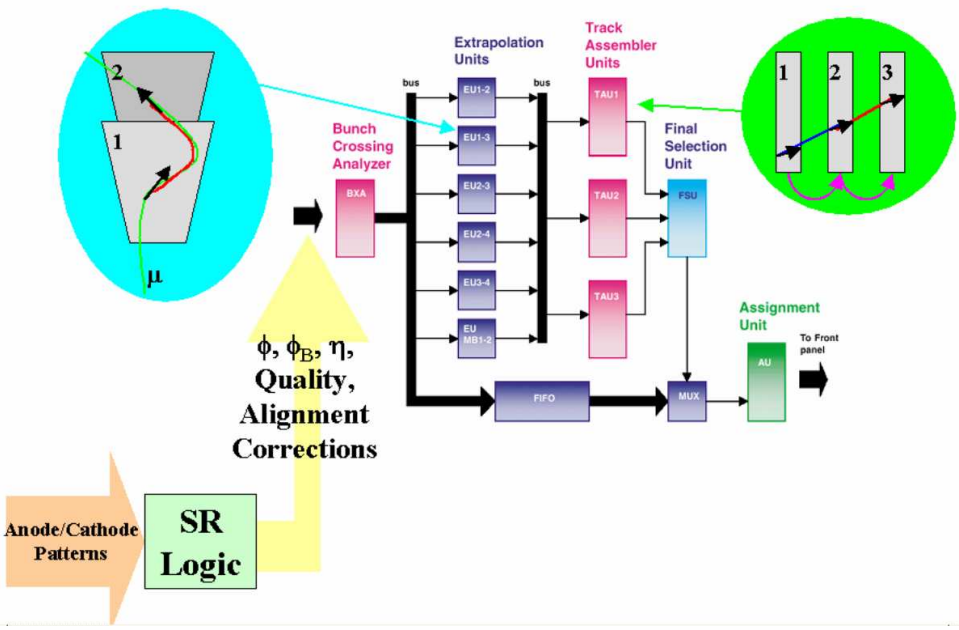

Figure 4.5: Sector Processor logic principle.

The track-finding process is partitioned into several steps. A given station within a sector may have as many as three LCTs reported to the SP. These LCTs are then converted into track-segments, which are described in terms of their ϕ and η coordinates. Each track-segment in each station should be checked against the segments in other stations to determine the likelihood to have originated from the same muon. Therefore, each track-segment is extrapolated through to other stations and compared against existing segments. If an extrapolation is successful, these segments are linked to form a single track. Each possible pairwise combination is tested in parallel. After extrapolation, doublets are then linked to assemble full tracks. Redundant tracks are canceled, the best three tracks are selected, and the track parameters are then measured.

The SP has the ability to handle LCTs received out of step from the bunch crossing time in which the actual muon traversed the detector volume: this can be the result of slight time shifts in electronic synchronization or because of electron drift time effects within the chambers. Handling these out of time LCTs is accomplished by

the Bunch Crossing Analyzer, which allows the Sector Processor to form tracks from LCTs received up to one bunch crossing later than the earliest LCT.

The first step in the track-finding process is to extrapolate pairwise combinations of track-segments. This is accomplished by requiring the two segments to be consistent with a muon originating from the collision vertex and with an appropriate curvature induced by the non-uniform magnetic field. A successful extrapolation is assigned when two track-segments lie within allowed windows of $\Delta\eta$ and $\Delta\phi$ - neither LCT should be parallel to the beam axis, and both should appear to originate from the interaction region.

The Track Assembler Units (TAUs) examine successfully extrapolated track-segment pairs to see if a larger track can be formed. If so, those segments are combined and a code is assigned to denote which muon stations are involved. For example, Figure 4.5 illustrates three LCTs (in stations "1", "2", and "3") being linked to form a single muon track. These tracks are first formed in pairwise combinations: an extrapolation of stations "$1 \rightarrow 2$" is successfully made, as well as a successful extrapolation of stations "$2 \rightarrow 3$". From the illustration, it is evident that these smaller tracks actually originate from the same muon, therefore, the TAU will combine the smaller tracks together to form a larger "$1 \rightarrow 2 \rightarrow 3$" association.

A list of nine possible tracks is sent to the Final Selection Unit (FSU). Since different data streams may contain data from the same muons, the FSU must cancel redundant tracks, and select the best three distinct candidates.

The final stage of processing in the TF, performed by the Assignment Unit, is the measurement of the track parameters which includes the ϕ and η coordinates of the muon, the magnitude of the transverse momentum p_T, the sign of the muon, and an overall quality (interpreted as the uncertainty of the momentum measurement). The most important quantity to calculate accurately is the muon p_T, as this quantity has

a direct impact on the trigger rate and on the efficiency. The total latency of the Sector Processor is 13 bx (Fig 4.6).

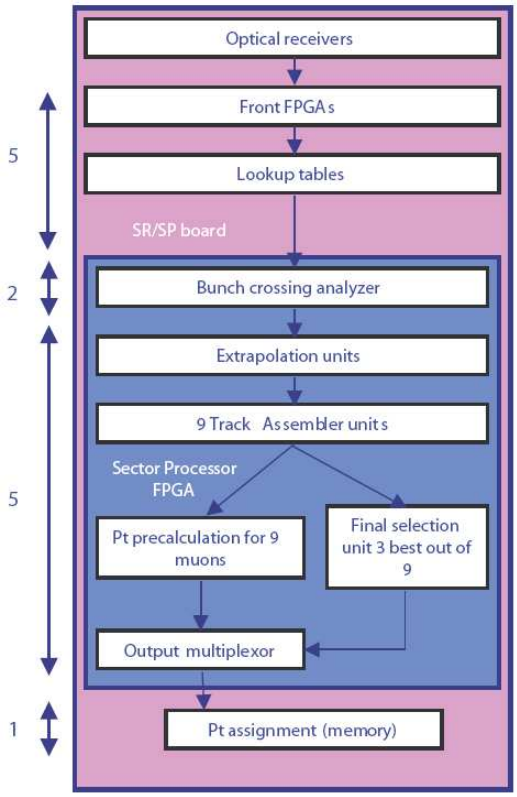

Figure 4.6: Diagram showing time required to complete each stage of track-finding process.

The Sector Processor board (Fig. 4.7) accepts fifteen optical links from five Muon Port Cards, where each link carries information corresponding to one muon track segment each bunch-crossing, which is described by a 32-bit word. Each link transmits a 32-bit word every 25 ns serialized over a 1.6 Gb/s optical link. Optical transceivers are used by the MPC for transmission, and by the SP for reception of LCT data. Additionally, the board receives up to 8 muon track segments, sent synchronous to the 40 MHz LHC clock, from the Barrel Muon system via a transition card behind the Track-Finder crate's custom backplane.

Because the track segment information arrives from 15 different optical links, it is aligned to the proper bunch crossing number by use of front-end FIFOs and syn-

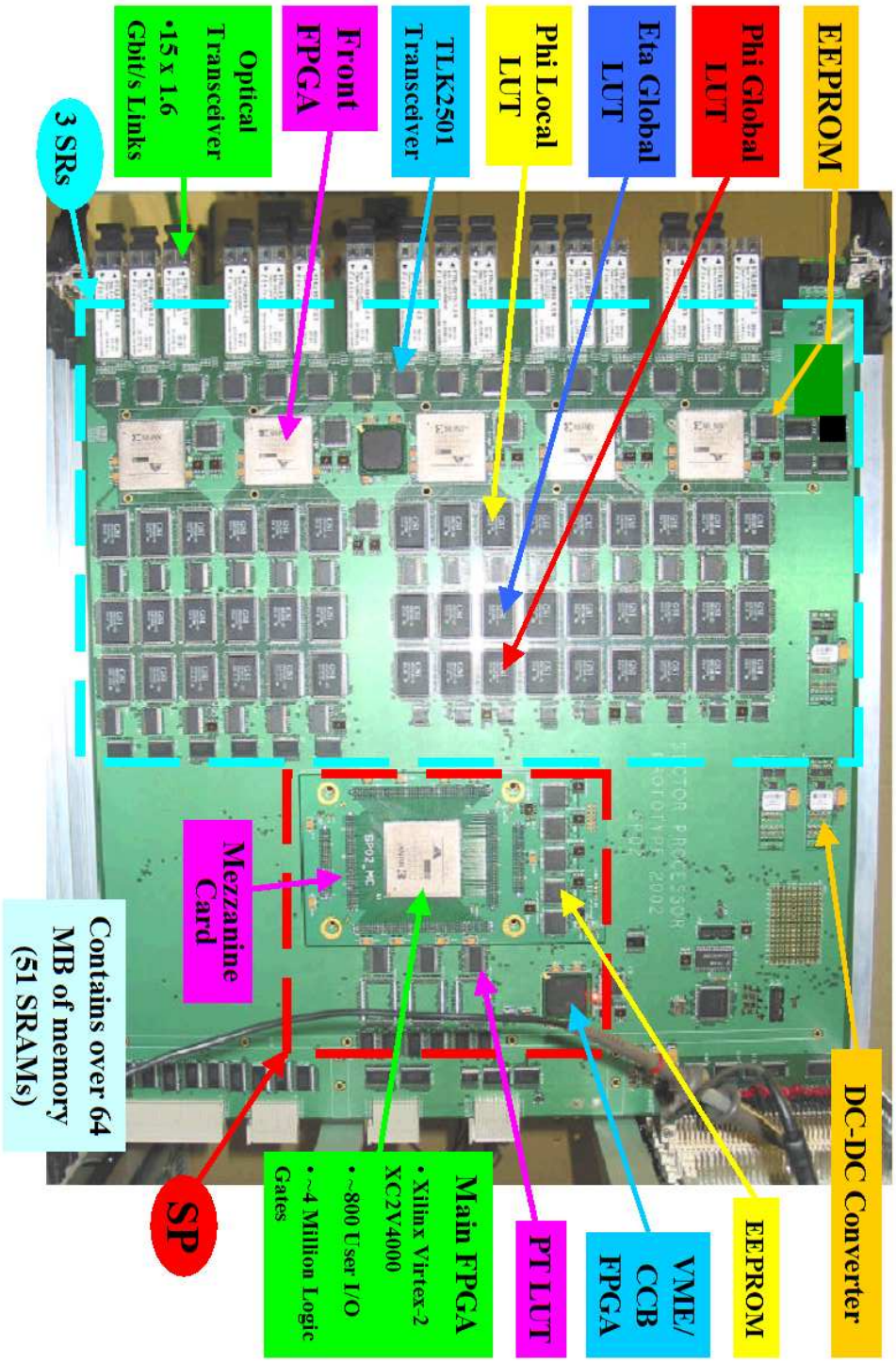

Figure 4.7: Photograph of the SP2002 pre-production prototype board.

chronization procedures. The Sector Receiver algorithm is implemented in a series of cascaded look-up memories, in order to minimize the size of static memories (SRAM) chips required: chamber specific LCT data is sent to the first memory, this memory then sends a local ϕ measurement to two more memories which then use this local ϕ measurement along with the original LCT data to form a global ϕ and η measurement for the given sector.

The angular information for all track segments is then passed to the main FPGA, which executes the entire 3-dimensional tracking algorithm of the Sector Processor. This FPGA sits on a mezzanine card on the SP, thus allowing for maximum design flexibility for future improvements. The output of the Sector Processor FPGA is sent to the p_T assignment lookup tables, also SRAMS, and the results of the p_T assignment for the three best muons are sent via the custom backplane to the Muon Sorter.

Upon receiving a "Level-1 Accept" command from the Global Trigger, the SP will send data that is useful for diagnostics as well as for seeding HLT candidates to a Data Acquisition (DAQ) readout board over the SPs sixteenth optical link. This board receives the LCT data received by the SP from the MPC, and the final results completed by the SP. Communication between the SP and the DAQ readout board is currently undergoing tests.

4.2 Simulated Performance of the Sector Processor

In order to test the hardware functionality against the expectations during LHC running, an object-oriented software emulation of the Track-Finder was written. Each of the stages involved in the muon track finding process was programmed so as to faithfully emulate the electronic data-flow and operation. This method has the advantage of allowing the track-finding algorithms to be developed and verified in a simulation environment. The results of the simulation can then guide the overall design and demands of the hardware.

The contents of the p_T look-up-tables used on the Sector Processor is derived from a parameterization of two- and three-station p_T measurements obtained through simulation studies. These studies show that the sagitta of the muon tracks induced by the magnetic field can be determined by taking the differences between the ϕ coordinates of track-segments at given stations. Because the sagitta is inversely proportional to the muon p_T, a two-station functional relation $\Delta\phi_{ij} = A[\eta]/p_T + B[\eta]/p_T^2$ can be defined such that p_T is uniquely determined for possible $\Delta\phi$ values. Alternatively, information from three stations may be used so that $p_T = f(\Delta\phi_1, \Delta\phi_2, \eta)$. The function can be found by studying the correlated distributions of $\Delta\phi$ between stations for particular p_T and η bins (Fig. 4.8).

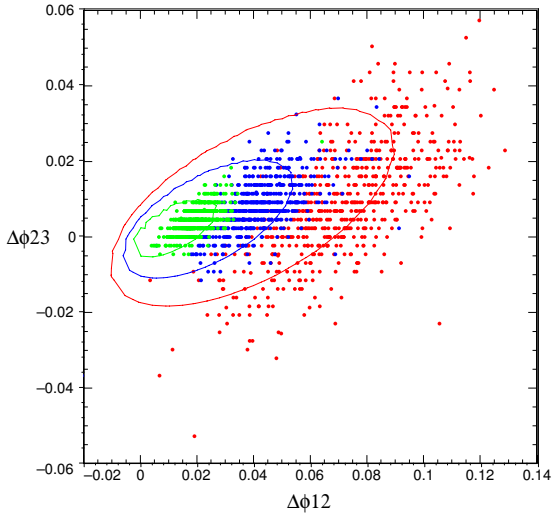

Figure 4.8: A scatter plot of the difference in measured phi coordinates between stations 2 and 3 versus stations 1 and 2 in radians for fixed transverse momentum bins of 3 GeV/c (red), 5 GeV/c (blue), and 10 GeV/c (green) in $2 < |\eta| < 2.1$. The three-station parameterization contours are shown in the same colors [46].

For either two- or three-station measurements, the parameters may be found by using simulated muon data that is uniformly distributed over the detector volume in η and ϕ for fixed p_T values. These parameters can then be stored in memories on the SP and used in the AU. Depending on which stations are used, the track-finder is at best able to reconstruct muons with a p_T resolution of 22% (Fig. 4.9).

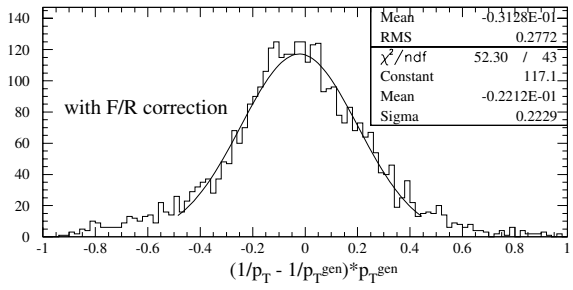

Figure 4.9: Residual distribution of $1/p_T$ measured for generated sample of single-muon events with $3 < p_T < 35$ GeV/c in $1.2 < \eta < 2$ [46].

The current performance of the track-finder is such that the single-muon p_T threshold applied by the Global Trigger is set at 19 GeV/c and di-muon thresholds at 7 GeV/c, while the track-finder still satisfies the Level-1 Trigger rate requirements.

The past six years have been extremely active for those involved in designing and testing the Sector Processor. The first prototype (SP2000) board design was significantly different than the production model [47]. The Sector Receiver portion of the track-finding logic was housed on three separate 9U VME boards. The SP2000 received track-stub data from these three boards and executed the tracking logic using a variety of memories and FPGAs on a single board. A total of six 9U VME crates are required to house the total Track-Finder design. Although a prototype track-finder for a single sector was successfully built and tested to be in complete agreement with offline emulation, the bunch-crossing latency exceeded the allowed budget. New technologies, such as small and fast optical transceivers and new high-density FPGAs, allowed the overall design of the track-finder to be greatly simplified such that the Sector Receiver logic could be contained on the same 9U VME board as the Sector Processor logic. The Sector Receiver logic could then be implemented by on-board memory-chips (SRAMS), and the entire Sector Processor algorithm could be executed by a single FPGA and some SRAMs. This has lead to the design of the SP2002 board. This board has undergone numerous tests over the past two years,

which are described below. With a few more improvements, the production level SP2004 board has now been completed and is currently undergoing tests.

Below is a summary of the tests completed on the SP2002 board. These tests began with simple bench tests at the University of Florida followed by a series of cosmic ray tests and four muon beam-tests at CERN over a two year period. With each new beam-test, the number of detectors used for triggering and readout generally increased which allowed the trigger and data acquisition hardware and event-building software to be stress-tested.

4.3 Hardware Bench Tests

During the first half of 2003, testing began on the second prototype Sector Processor hardware. In order to test the Sector Processor's functionality, custom software was needed to communicate through the VME interface. This interface consists of a bus adaptor card on a PCI bus connected through optical fiber to a VME control card which communicates to the SP through the VME backplane. The Hardware Access Library (HAL), which is part of the XDAQ software package from CMS DAQ [48], facilitated this purpose by providing a generic set of read and write commands independent of the particular bus adapter used for VME communication, thus maximizing the portability of command sequences generated to control a given VME hardware module. All tests performed on the MPC and SP used special C++ classes developed from the same primitive commands.

The SP control and readout software modules were created to be used within a XDAQ environment. This allowed communication of VME modules in multiple VME crates over a network. With these XDAQ classes, one can control multiple modules in multiple crates with the use of a single interface, therefore concealing the control register layer, offered by the firmware of each hardware module, from the user. These tools can then be used for the development of a run-control system of the endcap system.

During this initial test period, the following tasks were completed:

- The FPGAs were successfully programmed.
- Both the VME interface and the on-board databus were validated.
- All I/O were tested.
- The Sector Processor was also successfully interfaced with a Muon Port Card.
- Test routines were written which load test LCT patterns into the MPC input buffer, and transmit a subset of these patterns over the optical links into the SP.
- The output LCTs from the MPC were checked against the SP input LCTs, and were found to be in agreement.

4.4 Hardware Tests using Cosmic Ray Muons

In July 2003, the University of Florida hosted a cosmic ray test stand (Fig. 4.10). The cosmic test stand consisted of two CSCs fixed with faces pointing vertically. Scintillators were positioned above and below the two CSCs to provide a primitive trigger to the CSC electronics and SP. The scintillators were connected to a NIM analog-to-digital converter and then a coincidence unit which provided a trigger when a muon caused coincident signals between scintillator layers. This trigger allowed the CSC data to be read out of the front-end and SP electronics.

Figure 4.10: Photograph of University of Florida Cosmic test stand.

Some of the successes of this stand include:

- Both the trigger and DAQ data streams were checked and compared for consistency.
- A common data read out and configuration software package to be debugged which could be used to configure the whole CSC trigger system, read out data, and store the data to disk using a single data format.

4.5 Hardware Tests using Particle Beams

4.5.1 First Beam-Test

During the time from May 15 through July 1, 2003, the SP2002 front-end optical communication was tested using both muon and pion beams in the X5A area at CERN. Periods of both time-unstructured and time-structured muon beams were provided. The time-structured beam muon was divided into bunches, and arrived synchronously to the machine clock (Fig. 4.11).

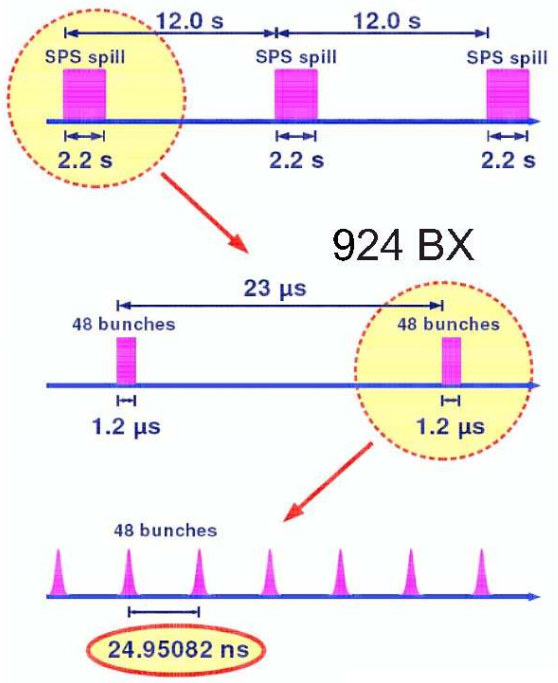

Figure 4.11: Time structure of test beam.

Figure 4.12 illustrates the configuration of the detector and electronics used during the test. It consisted of two CSCs placed in the beam-line along with three scintillators used to externally trigger the detector readout. The TTC crate contained a TTC module, which served the CCB cards in the Peripheral and Track-Finder crates, both the clock and control signals. The Peripheral Crate also contained two DAQ Mother Boards (DMBs) used to serve the precision DAQ data to the DDU board, two TMBs used to serve the trigger primitives to the MPC, and one MPC used to sort and send the best three trigger primitives to the Track-Finder crate through optical-links.

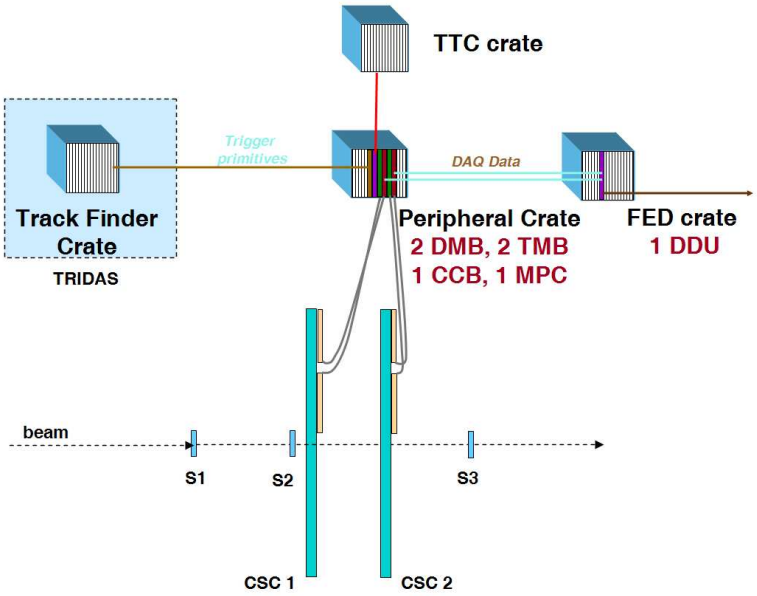

Figure 4.12: Detector and electronics configuration used during beam-test.

While proving useful for understanding the procedures needed to properly configure the numerous delay settings of the electronic modules in the trigger and DAQ paths, LCT data could not be retrieved from the SP front-end FIFOs. This beam-test period demonstrated that using the CCB clock (phased locked to the TTC system clock) to drive SP optical link transceivers can be problematic as link synchronization between the MPC and SP was not possible. The original design for the SPs optical links called for a common clock, provided by the TTC system and distributed by the CCB module, for the operation of transceivers and for trigger logic. An adequate

solution developed after the beam-test was to have a low-jitter clock (e.g. from a crystal phase locked to the TTC clock) operating at the transmitter frequency, which acts as a reference for the transceivers, and a second clock driving the SP logic; this design allowed the links to operate more robustly with respect to clock jitter in the distributed LHC clock.

4.5.2 Second Beam-Test

The period from September 9 to September 24 2003 marked another beam-test with the same configuration as in May. The primary purpose was to demonstrate synchronous operation of the trigger system up to through the SP2002 optical links. The front-end electronics formed LCTs and sent them to a MPC, which then sent the best three of a possible four LCTs to the SP over optical links. Using custom data acquisition software, the SP's input data buffers were read out, and the results were compared event-by-event with the front-end electronics data. Because the front-end data contained a possible four LCTs, the MPC sorting logic was simulated and 100% agreement between front-end and SP data was found.

During this same period at CERN (separate from the beam-test), interface tests were successfully conducted with the Drift-Tube Track-Finder electronics. The SP communicates with this DT Track-Finder through a special backplane connection. Random track data was successfully sent and received by both the DT track-finder and the SP.

4.5.3 Third Beam-Test

CERN hosted another beam-test period from May 18 to June 14 2004. The first half of this time was detected for asynchronous beam and the second half for synchronous beam. The goals for this period were to test the final CSC production electronics, demonstrate self-triggering by use of the track-finder, and to increase the system complexity over the previous test beams in order to more closely approximate

actual running conditions. These test were very important as the next steps were production and installation. Two extra CSCs were added in the beam line (ME1/1 and ME1/2) and a RPC was mounted onto the ME1/2 chamber (Fig. 4.13 and Fig. 4.14). In addition, for some runs an iron block was placed in the beam line to scatter the muon beam in a similar manner as the iron disks on which the CSCs are mounted.

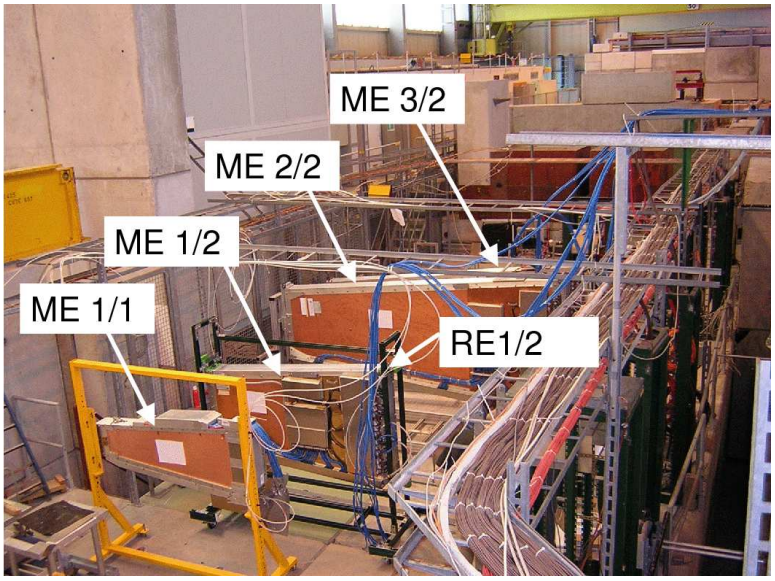

Figure 4.13: Photograph of June 2004 test beam configuration.

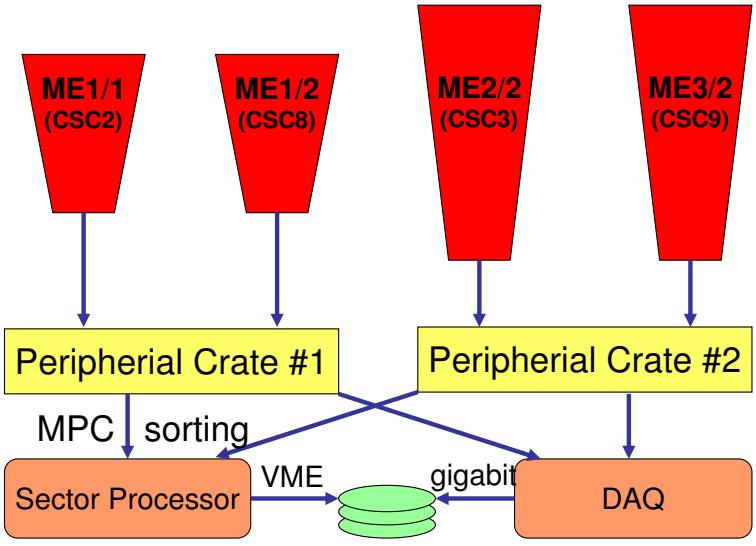

Figure 4.14: Diagram of May 2004 test beam configuration.

During this four week time, many additional tests were completed and include:

- The Track-Finder run control was integrated with the Peripheral Crate software.
- Multiple peripheral crates were used to send LCT data to either one or two Sector Processors.
- New logic configurations of the front end electronics were tested.
- Communication between the SP and Muon Sorter card was tested. The raw data was injected into the hardware emulation and successfully tested against hardware performance.
- Using the SP2002, the system was able to self-trigger.

This beam-test period marks the first time the Track-Finding logic was used to form tracks from front-end data. From these tracks, the Track-Finder was able to provide a trigger to the full system to readout the DAQ data. This required the time alignment of LCT data coming over optical links (Fig. 4.15).

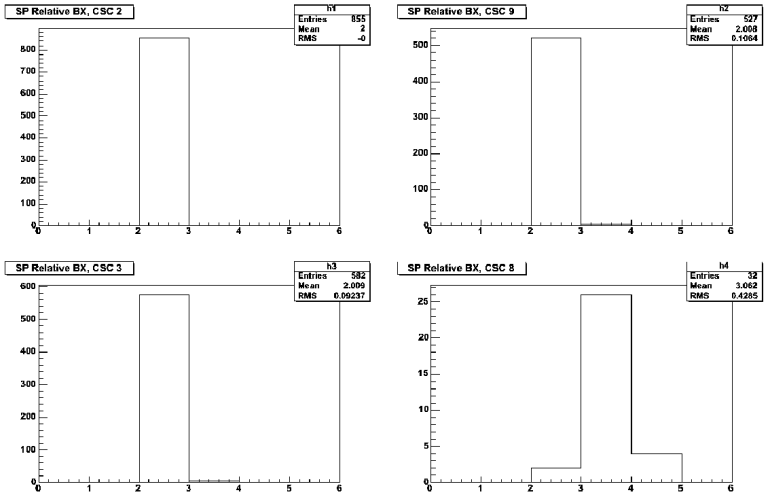

Figure 4.15: Track-Finder event display showing the relative bunch-crossing on which LCT data was collected after L1A signal. The bottom right plot shows a mistimed CSC with respect to the other three.

In addition to tests of data flow and hardware functionality, the trigger logic was checked by sending LCT data into the hardware emulation. The final list of LCT inputs and linked track outputs were compared between emulation and hardware, and perfect agreement was found between the two (Fig. 4.16).

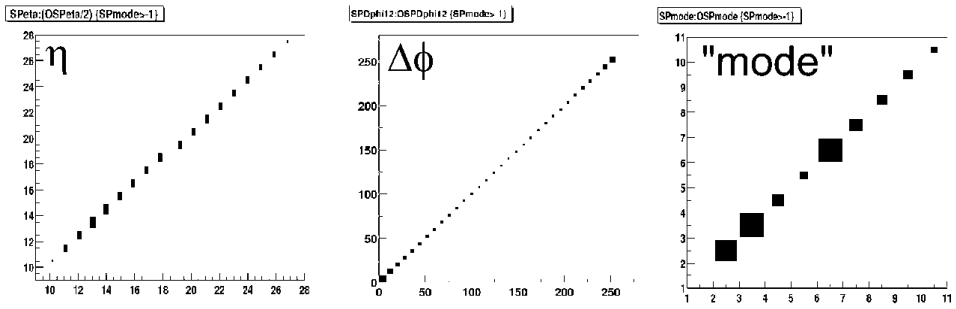

Figure 4.16: Plots showing comparison of track-finder data found in hardware vs results of emulation.

Because four chambers were used during this test, it was possible to track-find and therefore trigger using two Sector Processor cards in the same crate. Each Sector Processor received LCT data from two of the four chambers. This allowed the Muon Sorter card to be checked by sending it tracks from two Sector Processor cards across the custom backplane.

4.5.4 Fourth Beam-Test

From September 22 to October 11, 2004, the H2 area at CERN hosted a time-structure test beam. During this period, a full trigger detector slice-test was conducted using one HCAL wedge, four CSCs (plus one additional CSC not used in the CSC trigger), and three RPCs (Fig. 4.17 and Fig. 4.18).

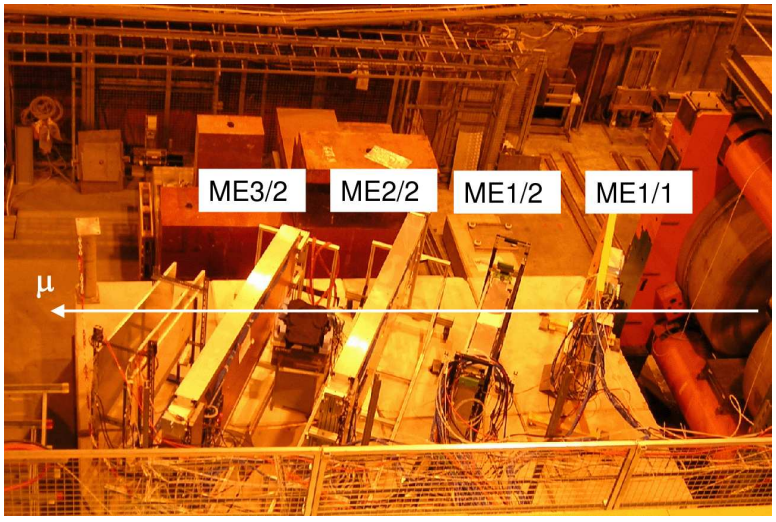

Figure 4.17: Photograph of October 2004 Testbeam.

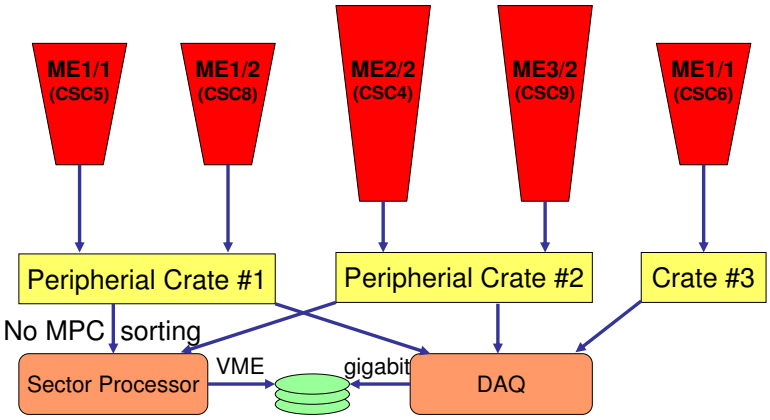

Figure 4.18: October 2004 test beam configuration.

Three peripheral crates were used, and therefore three independent MPCs synchronously sent LCT data to the Sector Processor. The MPCs were programmed not to sort the LCTs so that the data from each chamber could be routed to a specific SP input link. The simultaneous operation of two SP2002 boards was also tested during this period such that one received LCT data from the ME1/1 and ME1/2 chambers, and the other received LCT data from the ME2/2 and ME3/2 chambers.

The Muon Sorter card was also tested by examining the output in both one and two Sector Processor cards. Comparisons between the MS winner bits of best SP tracks, and those reported by the emulation show perfect agreement in 270,000 events. The SP functionality was also tested and found to be in perfect agreement with the software emulation. Figure 4.19 shows the (η, ϕ) coordinates of hits that occured in various chambers. In order for data to be recorded to disk, the trigger bit must be set which requires at least two chambers have LCTs in coincidence. Therefore, figure 4.19 demonstrates it is possible to see the "profile" of one chamber with respect to the other in a given pair.

Figures 4.20 and 4.21 show the LCT "global-" ϕ and η coordinates of the hits in the various chambers. These coordinates are calculated using the SP front FPGA's, which contain a rough mapping of wire group and strip number to global- ϕ and η.

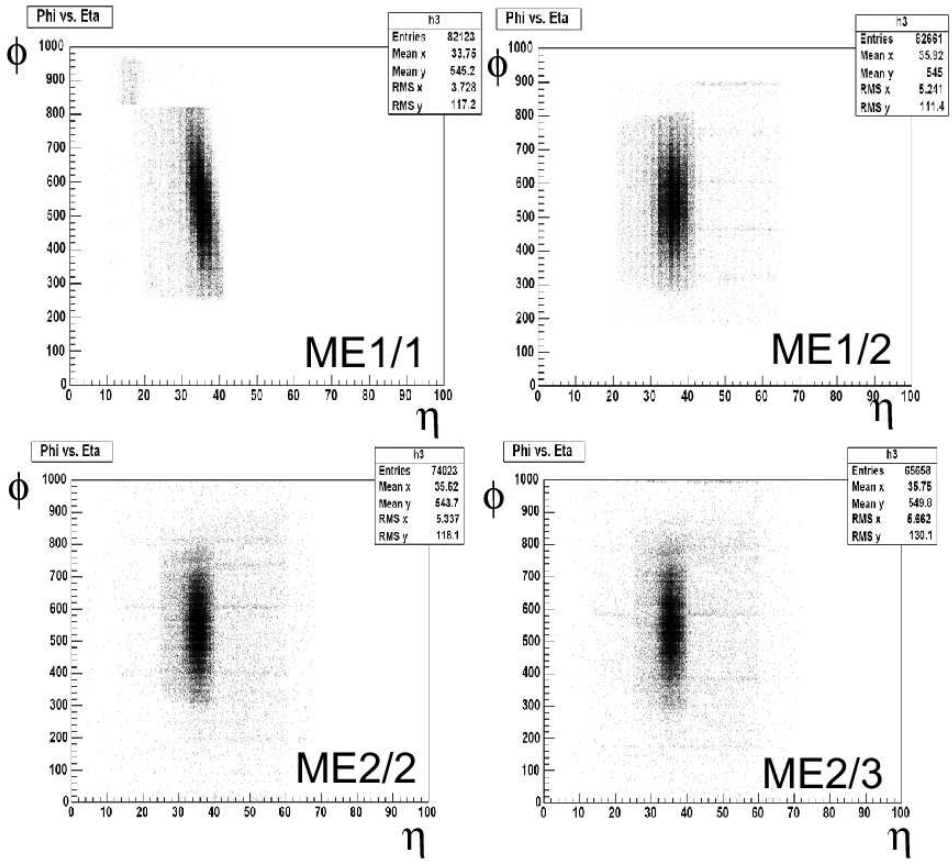

Figure 4.19: Plots showing "η" vs "ϕ" distributions for various chambers. ME1/1 shows a position offset in the upper left side of distribution due to ganged strips in chamber, resulting in small ϕ positions being mapped to larger values.

For beam-test purposes, these are programmed such that the η and ϕ coordinates roughly corresponded to wire-group and strip number in the CSCs.

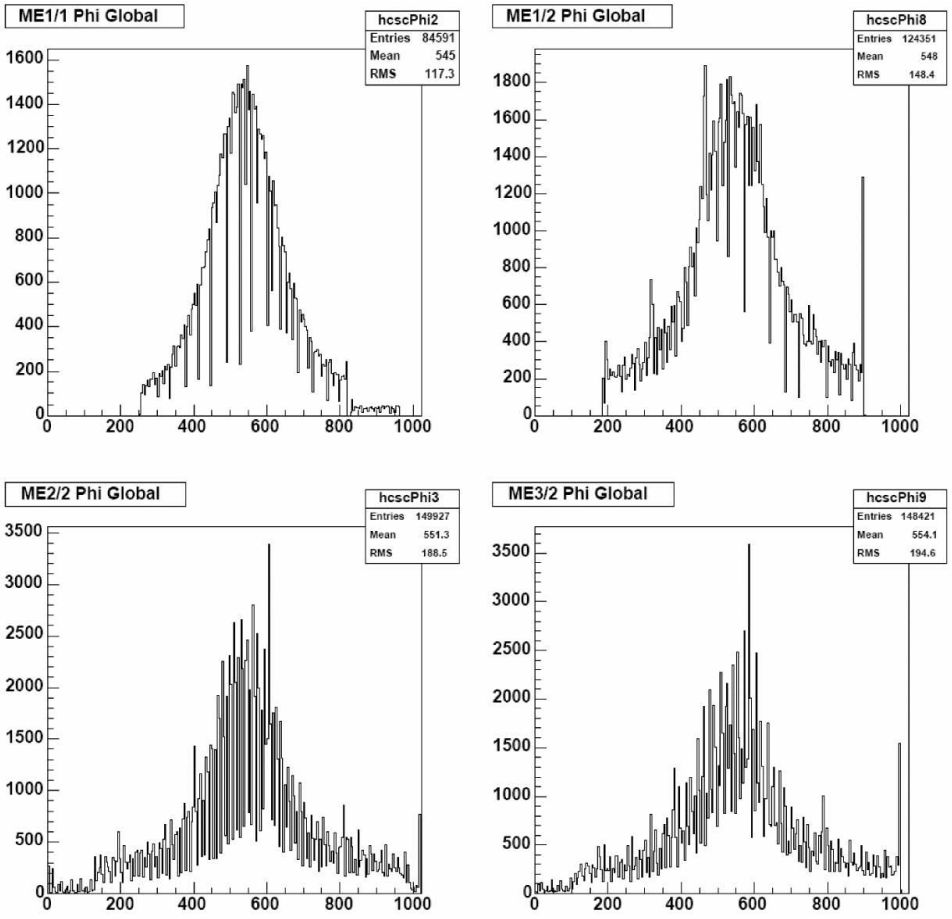

Figure 4.20: Global "ϕ" distributions.

The differences in "ϕ" and "η" positions between chambers for these hits are shown in figures 4.22 and 4.23. These distributions demonstrate that the beam indeed traverses roughly the same linear path through all chambers in the beam line.

4.6 Current Status

In Mid 2005, the first two SP pre-production grade boards (SP04) were completed (Fig. 4.24). While remaining fully compatible with the prototype SP2002 board, the SP04 design includes the following improvements:

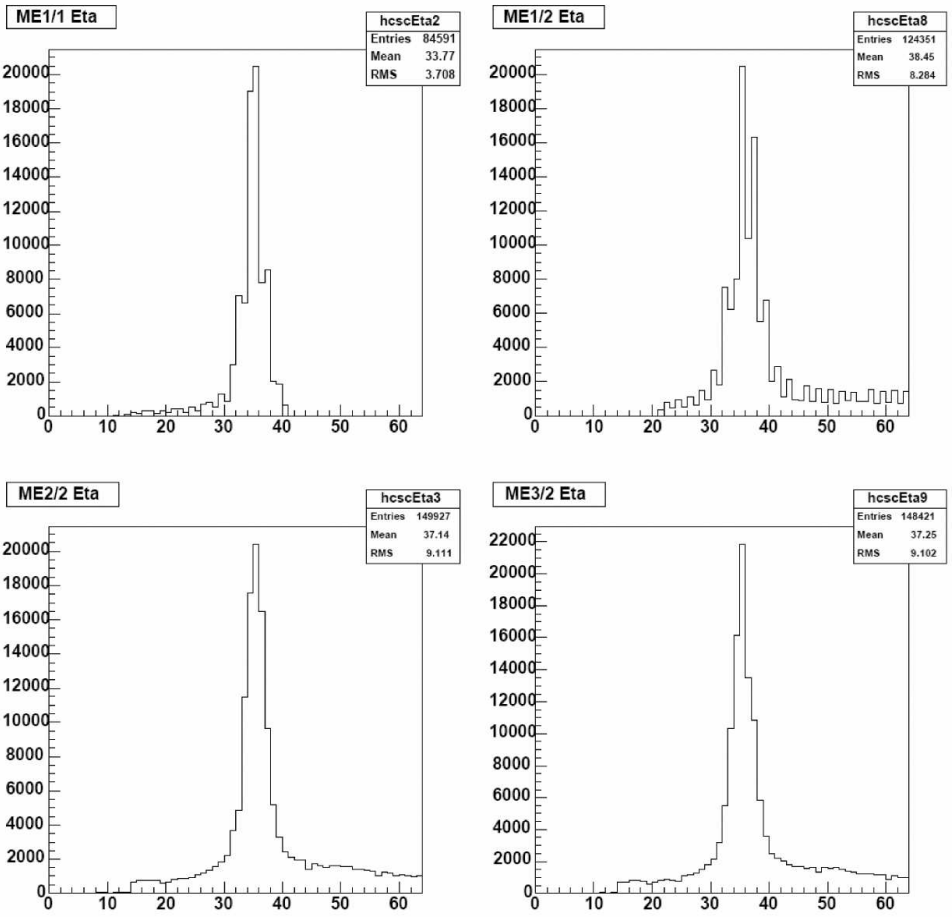

Figure 4.21: Global "η" distributions.

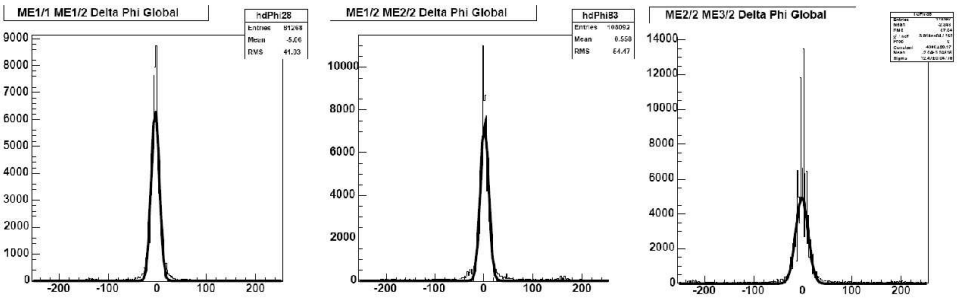

Figure 4.22: Distributions of differences in "ϕ."

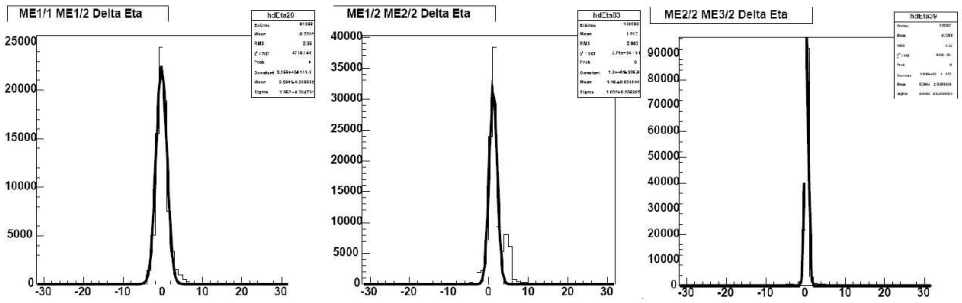

Figure 4.23: Distributions of differences in "η."

- 256 Mbit flash RAM now allows all LUTs to load on power-up. This saves the user from having to reprogram all memories after each hard reset.
- QPLL daughterboard is now used to provide a stable clock to the optical links.
- On-board 40 MHz crystal oscillator is used for DDU optical link.
- LEDs specifically to indicate the arrival of LCTs to the SP front-end.
- Board i.d. switches.

These two SP04 boards required extensive repair as a result of the vendors used to build them. After switching vendors, 26 final SP05 boards have been completed as of this writing (Fig. 4.25). Each board has undergone a series of validations including:

- Basic chip, link, and clocking validations.
- Verify data injections and readouts.
- Comparison of streamed random data through boards with emulation software using real LUTs and random LUTs.
- Muon Sorter interface test. This includes checking clock synchronization between two boards, as well as verification of MS winner bits.

Other CSC Track-Finder modules have been produced and tested in addition to the SP05:

- 26 SP Mezzanine cards have been completed and tested. These cards are also used on the Muon Sorter board.

- The QPLL daughterboards used to provide a stable clock to the optical links have been tested.
- 21 transition cards which send data to and receive data from the Drift Tube Track-Finder have been tested.
- The DAQ interface card, which serves the DAQ system with CSC Track-Finder data, has been tested.

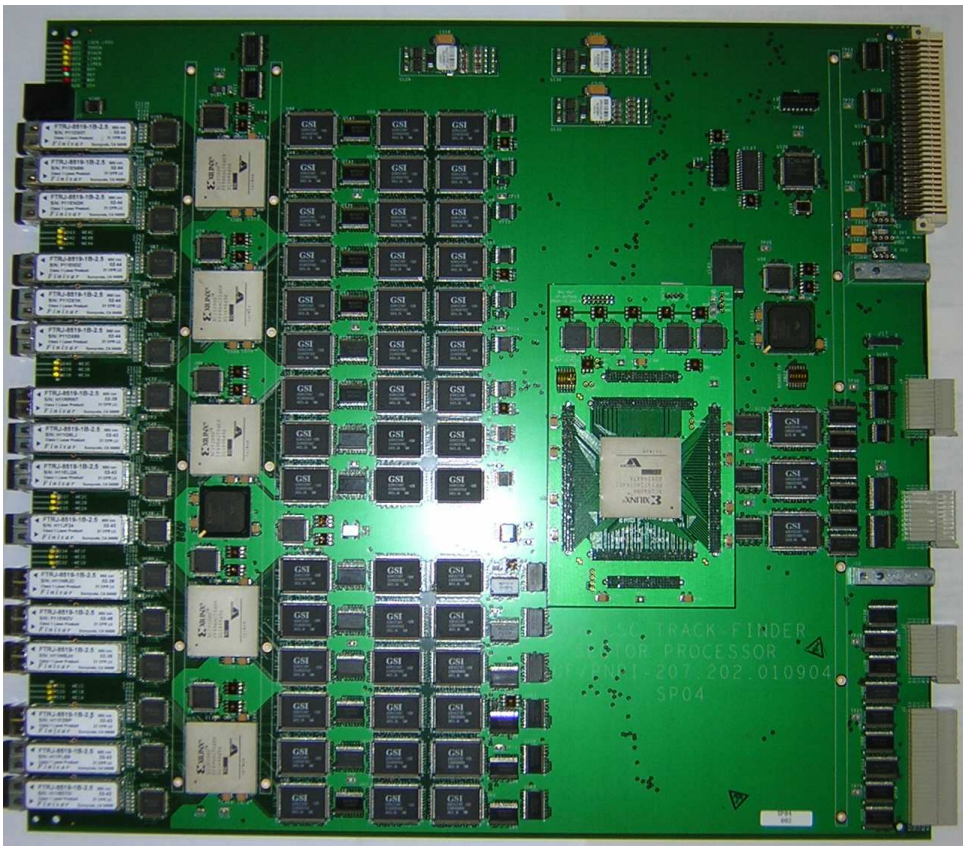

Figure 4.24: Photograph of the SP04 board.

A final CSC Track-Finder crate has been installed at SX5 for the MTCC and will provide a CSC trigger for cosmic ray muon data coming from a single sector used in the test. The goals of the MTCC are to check the magnet functionality, including cooling, power supply and control systems, as well as commission the RPC, CSC, DT, HCAL, ECAL, and Tracker systems.

Figure 4.25: Photograph of the final SP05 cards to be used at CMS.

CHAPTER 5
SIMULATION SOFTWARE

This study is executed using simulated CMS detector data which is simulated in three steps: *event generation*, *trigger and detector simulation*, and *event reconstruction*. Ultimately, the final product of this simulation chain is a dataset containing reconstructed physics objects such as muons and electrons, whose kinematic parameters faithfully match what reality will provide not only in magnitude, but in its systematic limitations.

5.1 Event Generation

Because the dynamics of particle interactions is fundamentally probabilistic, *Monte Carlo* techniques can be used to simulate physics from the initial state proton-proton collisions to the final state which contains the outgoing stable particles to be detected [49]. In this study the PYTHIA 6.225 [50] generator is used to simulate the proton-proton collisions in various steps. First, the initial proton, which is composed of *partons* (quarks and gluons), is characterized by its parton density function (PDF). This function defines what fraction of a proton's momentum is carried by a particular parton. These partons will usually radiate (e.g. $q_i \rightarrow q_i + g$) color-charged particles, which make up the event's *initial state radiation* (ISR). A parton from each proton then interacts in a *hard scattering* process, which could typically lead to a resonance such as Z or exotic particle production that ultimately decay according to the branching ratios obtained using the *matrix element* (ME) calculations. Electrically charged particles may further radiate photons throughout the process. The other partons that are left in the protons may participate in semi-hard interactions giving rise to *multiple parton interactions*. The remaining portion of the protons which did not

interact (*beam remnant*) are hadronized to form a shower of color singlet states. The unstable heavy hadrons with short lifetimes are decayed to their final state particles which traverse the detector volume. A list of these final state particles and their momenta are passed up stream to the detector simulation package.

The ISASUGRA 7.69 package is used to calculated the mSUGRA spectrum of SUSY masses and mixings, and is part of the event generator ISAJET 7.69 [51]. This generator takes the five mSUGRA parameters as inputs, evolves the SUSY parameters down to the electroweak scale in order to get the mass spectrum and branching ratios. Cross sections and decay widths are then derived by PYTHIA 6.225. The CTEQ5L [52] library is used for the parton distribution functions.

5.2 Full Detector Simulation

This work simulates the response of the CMS detector to simulated incident particles using a Geant4 [53] based framework, known as the Object-oriented Simulation for CMS Analysis and Reconstruction (OSCAR) [33]. The OSCAR framework is used to simulate the response of the CMS detector. It includes a description of the CMS detector geometry, materials, and magnetic field. It takes the list of generated particles in each event and propagates them through the detector material. In doing so, energy loss, multiple scattering, and showering are taken in to account. A particle's deposited energy in a particular portion of the detector, location, time of interaction, entry and exit points, and species are stored as "hits" data which are then used in simulated detector response and reconstruction of the event.

The Object-oriented Reconstruction for CMS Analysis (ORCA) [33] software framework is used to simulate the readout electronics, which for example converts energy deposits into digital ADC counts to form so-called "digis." The inclusion of pile-up, the conversion of "digis" to reconstructed detector objects ("hits"), the reconstruction of analysis objects (muons, jets, etc) from hits, and the trigger simulation are also performed by ORCA.

5.3 Fast Detector Simulation

Running the full CMS detector simulation package can be very CPU intensive. As not all studies need to be done using this full simulation in order to obtain reasonable results of CMS simulated performance, a fast detector simulation package known as the CMS FAst MOnte Carlo Simulation (FAMOS) framework [33] has been developed which includes a parameterization of the full Geant based simulation and reconstruction. This allows the most time consuming part of full reconstruction, the propagation of particles through the detector material, to be substituted by parameterizations of energy loss. $\mathcal{O}(100)$ seconds per event is saved by not simulating the detailed propagation. FAMOS is used in this work to facilitate simulations involving "scans" of the mSUGRA parameter space.

Because the fully simulated mSUGRA study points are simulated using pile-up conditions that include diffractive processes (corresponding to ~ 5 min-bias collisions per beam crossing instead of the default 3.5), the amount of pile-up included in FAMOS is tuned to 5 min-bias collisions per beam crossing in order to achieve good agreement between ORCA and FAMOS with respect to the average of the sum of the transverse energy measured from calorimetry.

CHAPTER 6
SIGNAL

6.1 SUSY Test Points

This dissertation presents the feasibility to discover Supersymmetry using the CMS detector by using simulated SUSY signal data generated under the mSUGRA scenario. Ideally, it is desirable to provide general experimental limits that are model-independent; however, because of the extensive number of free SUSY parameters, the only hope of obtaining experimentally useful results is to work with the limited number of free parameters offered by SUSY scenarios such as mSUGRA. As many studies have been conducted to this end, the model parameters have been standardized such that a set of "benchmark" points have been defined in mSUGRA parameter space to facilitate comparisons and discussions of results [54]. These points of interest are generally chosen in such a way as to be consistent with current experimental constraints such as the current value of the muon anomalous magnetic moment $(g_\mu - 2)$ [55], the branching ratios of $b \to s\gamma$ processes [56], and the relic LSP density $\Omega_\chi h^2$ [16].

The benchmark points are generally chosen by constraining all five mSUGRA parameters. These points, cross sections, mass contours, and 5σ reach-contours are usually displayed in the $(m_0, m_{1/2})$ plane. This is usually convienient as sparticle masses and production cross-sections generally scale strongly with these two model parameters: Figure 6.1 illustrates some common features of these plots.

A brief review of mSUGRA is given in Section 2.2. For all signal points studied, ORCA is used to fully reconstruct the digitized information into objects (such as muons, jets, etc) used for analysis. Table 6.1 displays the different parameters for all Geant based simulated and reconstructed mSUGRA points used in this analysis and

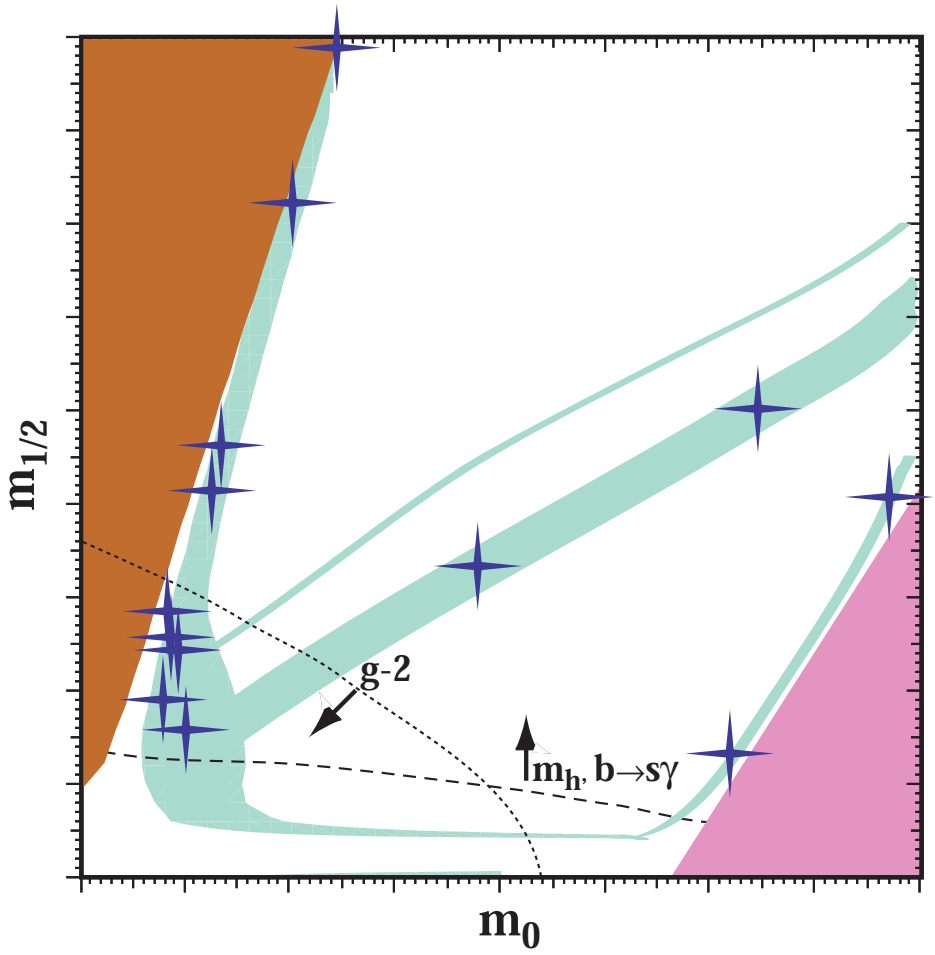

Figure 6.1: Cartoon showing qualitative features of benchmark points in the (m_0, $m_{1/2}$) plane. The light turquoise region shows the region most consistent with $\Omega_\chi h^2$. The left red region is excluded by because the LSP is the charged stau. The lower pink region is excluded as points in this region do not allow for electroweak symmetry breaking. Experimental constraints on the Higgs mass, rare B decays, and ($g_\mu - 2$) are shown to favor bottom left region in the plane. The blue crosses show potential benchmark points [54].

Figure 6.2 shows the mSUGRA cross section as a function of the universal mSUGRA scalar m_0 and gaugino $m_{1/2}$ masses.

Table 6.1: Parameters of fully simulated and reconstructed SUSY benchmark points studied in this work. The number of simulated events and the equivalent integrated luminosity are given.

	m_0 (GeV/c^2)	$m_{1/2}$ (GeV/c^2)	$\tan\beta$	A_0	sign(μ)	σ_{LO} (pb)	N_{Gen}	ΔL (fb^{-1})
LM1	60	250	10	0	+	41.9	98 250	2.3
LM4	210	285	10	0	+	19	96 500	5.1
LM5	230	360	10	0	+	6	84 000	13.9
LM6	85	400	10	0	+	4	99 250	24.6
HM1	180	850	10	0	+	0.052	80 000	1538.5

These points were selected in order to examine different experimental signatures. The so-called low mass points (points labeled "LMx"), were chosen such that they are suited for early discovery, whereas the high mass points (points labeled "HMx") are suited for later discovery after a few years of data have been collected. The points LM1, LM2, and LM6 are compatible with constraints given by WMAP Cold Dark Matter limits [57]. The other points, while not compatible with these limits, can be made so by modifying certain theoretical assumptions [58].

These points can be seen along with other benchmark points in Figure 6.3. The mass spectrum for each point is shown in Figure 6.4. Unless stated otherwise, the LM1 benchmark point is used for selection optimization in this study. This point is interesting as it is close to the current Tevatron limit, and therefore its signature would present itself very early during LHC running. Using LM1 as point of reference, an optimization is performed to select events with LM1 like signature, and its applicability to neighboring points in the common region of parameter space is demonstrated in the following sections.

The selection cuts derived for LM1 are applied across the $(m_0, m_{1/2})$ plane. A fast, parameterized, simulation and reconstruction is performed by FAMOS in order to scan the $(m_0, m_{1/2})$ plane for fixed mSUGRA parameters $\tan\beta = 10$, $\mu > 0$,

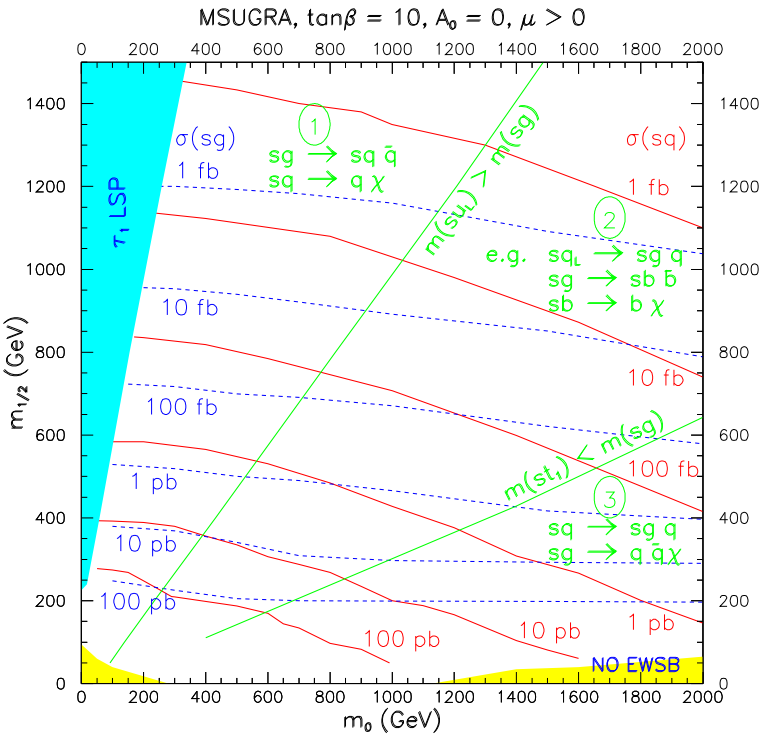

Figure 6.2: mSUGRA cross section in the (m_0, $m_{1/2}$) plane. Other mSUGRA parameters are fixed. The dashed line indicates the gluino cross-section, the solid line indicates the squark cross-section [30].

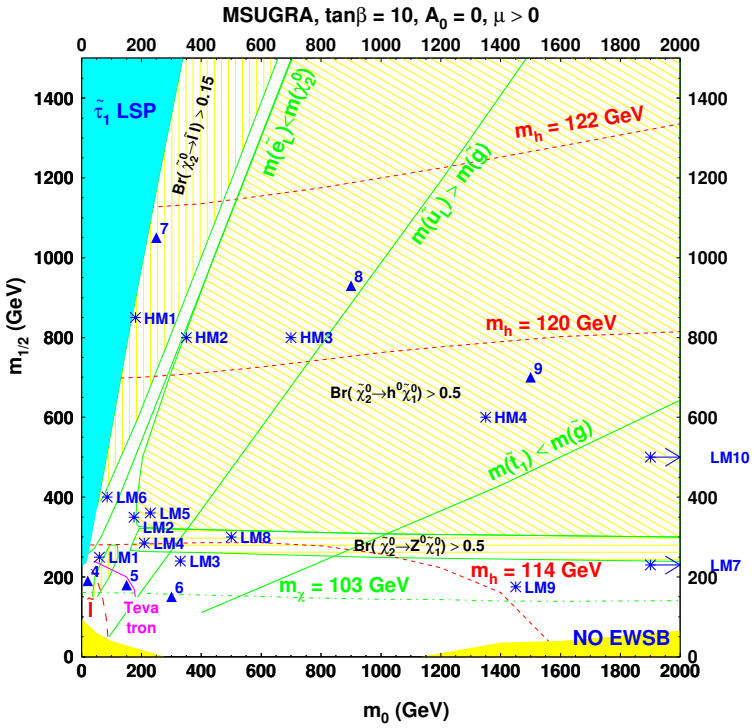

Figure 6.3: Studied CMS mSUGRA benchmark points are shown as stars. Excluded regions by theory (charged LSP and no electroweak symmetry breaking — shaded areas) and particle experiments (LEP mass of Higgs boson — long dashed line, LEP mass of chargino — dot-dashed line, LEP direct search for sleptons — solid line, Tevatron direct search for superpartners — short dashed line) are also shown [30].

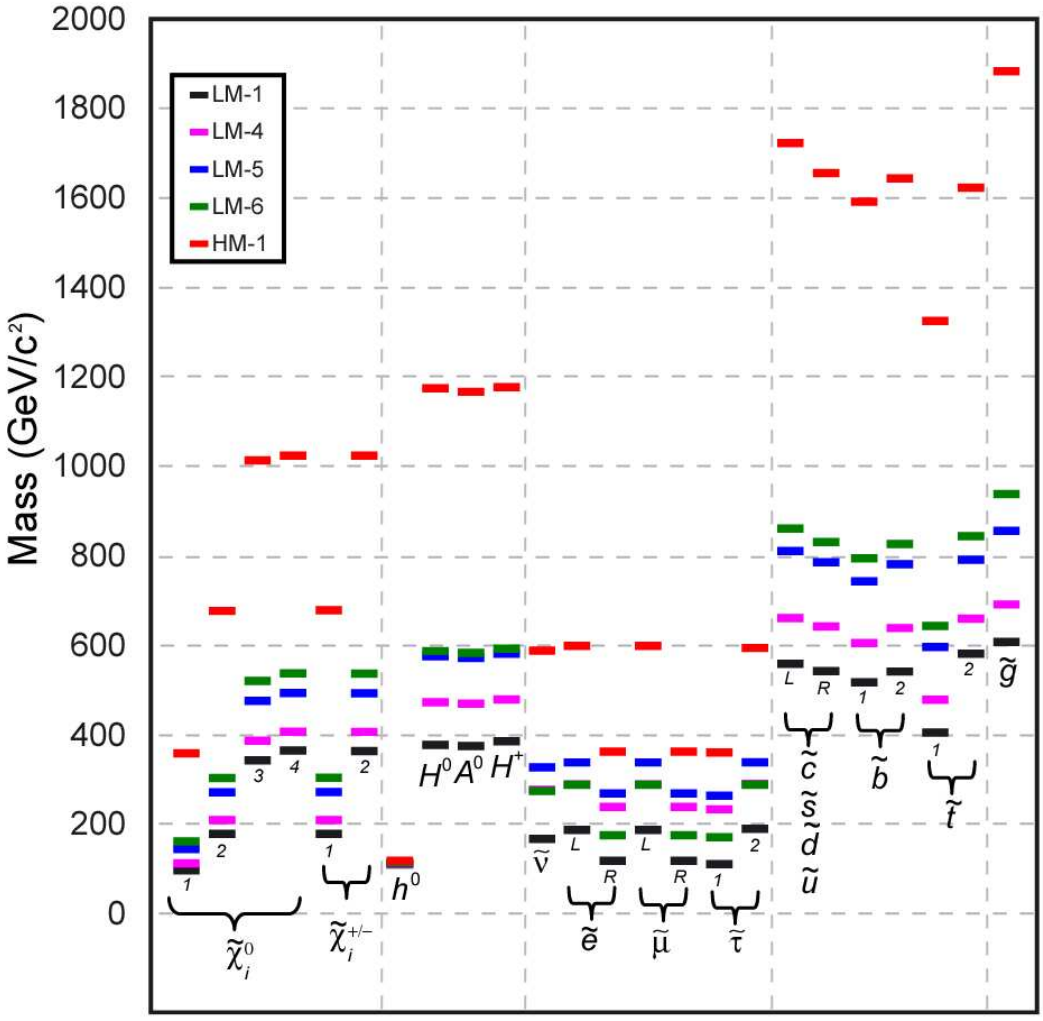

Figure 6.4: Comparison of SUSY mass spectra of the benchmark points fully simulated for this study.

and $A_0 = 0$. Points were generated on a coarse grid with $\Delta m_0 = 100$ GeV/c^2 and $\Delta m_{1/2} = 100$ GeV/c^2, starting from the point $m_0 = 100$ GeV/c^2, $m_{1/2} = 100$ GeV/c^2. For validation purposes, samples of the five benchmark points LM1, LM4, LM5, LM6, and HM1 are also produced with fast simulation, and compared with the Geant based simulated data. Some basic properties of these points are listed below [30].

LM1:

- Same as post-WMAP benchmark point B'.
- $m(\tilde{g}) \geq m(\tilde{q})$, therefore making $\tilde{g} \to \tilde{q}q$ dominant.
- $B(\tilde{\chi}_2^0 \to \tilde{l}_R l) = 11.2\%$, $B(\tilde{\chi}_2^0 \to \tilde{\tau}_1 \tau) = 46\%$, $B(\tilde{\chi}_1^\pm \to \tilde{\nu}_l l) = 36\%$.

LM4:

- $m(\tilde{g}) \geq m(\tilde{q})$, therefore making $\tilde{g} \to \tilde{q}q$ dominant, where $B(\tilde{g} \to \tilde{b}_1 b) = 24\%$.
- $B(\tilde{\chi}_2^0 \to Z^0 \tilde{\chi}_1^0) = 97\%$, $B(\tilde{\chi}_1^\pm \to W^\pm \tilde{\nu}_1) = 100\%$.

LM5:

- $m(\tilde{g}) \geq m(\tilde{q})$, therefore making $\tilde{g} \to \tilde{q}q$ dominant, where $B(\tilde{g} \to \tilde{b}_1 b) = 19.7\%$ and $B(\tilde{g} \to \tilde{t}_1 t) = 23.4\%$.
- $B(\tilde{\chi}_2^0 \to h^0 \tilde{\chi}_1^0) = 85\%$, $B(\tilde{\chi}_2^0 \to Z^0 \tilde{\chi}_1^0) = 11.5\%$, $B(\tilde{\chi}_1^\pm \to W^\pm \tilde{\chi}_l^0) = 97\%$.

LM6:

- Same as post-WMAP benchmark point C'.
- $m(\tilde{g}) \geq m(\tilde{q})$, therefore making $\tilde{g} \to \tilde{q}q$ dominant.
- $B(\tilde{\chi}_2^0 \to \tilde{l}_L l) = 10.8\%$, $B(\tilde{\chi}_2^0 \to \tilde{l}_R l) = 1.9\%$, $B(\tilde{\chi}_2^0 \to \tilde{\tau}_1 \tau) = 14\%$, $B(\tilde{\chi}_1^\pm \to \tilde{\nu}_l l) = 44\%$.

HM1:

- $m(\tilde{g}) \geq m(\tilde{q})$, therefore making $\tilde{g} \to \tilde{q}q$ dominant.
- $B(\tilde{g} \to \tilde{t}_1 t) = 25\%$, $B(\tilde{q}_L \to q\tilde{\chi}_2^0) = 32\%$, $B(\tilde{t}_1 \to t\tilde{\chi}_2^0) = 6\%$, $B(\tilde{t}_1 \to t\tilde{\chi}_3^0) = 18\%$, $B(\tilde{t}_1 \to t\tilde{\chi}_4^0) = 9\%$.
- $B(\tilde{\chi}_2^0 \to \tilde{l}_L l) = 27\%$, $B(\tilde{\chi}_2^0 \to \tilde{\tau}_1 \tau) = 14\%$, $B(\tilde{\chi}_1^\pm \to \tilde{\nu}_l l) = 37\%$.

The sparticle mass spectra for the mSUGRA points are approximately given by the following relations [30]:

$$\begin{aligned}
m_{\tilde{g}} &\simeq 2.7 m_{1/2} \\
m_{\tilde{\chi}_2^0} &\simeq m_{\tilde{\chi}_1^\pm} \simeq 2 m_{\chi_1^0} \simeq 0.8 m_{1/2} \\
m^2_{\tilde{u_L}} &\simeq m_0^2 + 5.0 m_{1/2}^2 + 0.35 M_Z^2 \cos 2\beta \\
m^2_{\tilde{d_L}} &\simeq m_0^2 + 5.0 m_{1/2}^2 - 0.42 M_Z^2 \cos 2\beta \\
m^2_{\tilde{u_R}} &\simeq m_0^2 + 4.5 m_{1/2}^2 + 0.15 M_Z^2 \cos 2\beta \\
m^2_{\tilde{d_R}} &\simeq m_0^2 + 4.4 m_{1/2}^2 - 0.07 M_Z^2 \cos 2\beta \\
m^2_{\tilde{e_L}} &\simeq m_0^2 + 0.49 m_{1/2}^2 - 0.27 M_Z^2 \cos 2\beta \\
m^2_{\tilde{\nu}} &\simeq m_0^2 + 0.49 m_{1/2}^2 - 0.50 M_Z^2 \cos 2\beta \\
m^2_{\tilde{e_R}} &\simeq m_0^2 + 0.15 m_{1/2}^2 - 0.23 M_Z^2 \cos 2\beta
\end{aligned} \tag{6.1}$$

The masses of third generation scalars cannot be put into this convenient form as they have more complex relations dependant on the Yukawa couplings and off-diagonal matrix elements which mix left and right states. The squark and gluino isomass contour lines in the $(m_0, m_{1/2})$ can be seen in Figure 6.5.

6.2 Sparticle Decays

The squark and gluino production cross-section in the $(m_0, m_{1/2})$ plane assuming $\tan\beta = 10$, $A_0 = 0$, $\mu > 0$ is shown in Figure 6.2. In this plane, the dominate features are determined by being in one of three regions [30]:

- Region 1: As shown in Figure 6.5, in this region the gluino mass is heavier than the squarks. Therefore, the decay topology is dominated by $\tilde{g} \to \tilde{q}\bar{q}$ and $\tilde{q} \to q\chi$.
- Region 2: In this region, the gluino is lighter than at least one squark, and therefore the squarks can decay through complex chains.

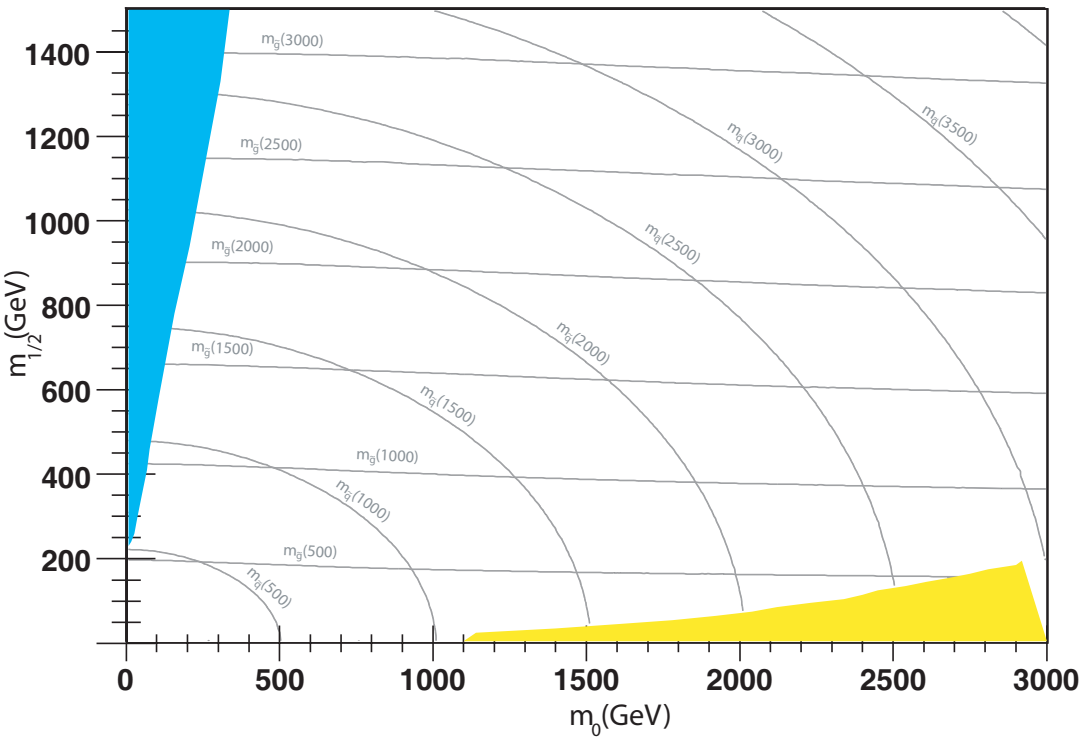

Figure 6.5: Squark and gluino isomass contours in the (m_0, $m_{1/2}$) plane.

- Region 3: in this region, the gluino is lighter than all squarks. Therefore, the gluino can only lead to the LSP through a three-body decay mediated by a virtual squark.

6.2.1 Charginos and Neutralinos

At the LHC charginos and neutralinos can usually be produced through the cascade decays of strongly interacting sparticles. They can also be directly produced through Drell-Yan processes. The decay of the lightest chargino will generally lead to an isolated lepton plus missing transverse energy. The $\chi_1^{\pm}$ will typically decay in one of the following ways depending on choice of model parameters:

$$\begin{aligned}\tilde{\chi}_1^{\pm} &\rightarrow \tilde{l}\nu \\ &\rightarrow \tilde{\nu}l \\ &\rightarrow W^{\pm}\tilde{\chi}_1^0 \\ &\rightarrow H^{\pm}\tilde{\chi}_1^0 \\ &\rightarrow l^{\pm}\nu\tilde{\chi}_1^0 \end{aligned} \tag{6.2}$$

The second-lightest neutralino will typically decay to two isolated leptons plus missing transverse energy. In particular, the $\tilde{\chi}_2^0$ will usually decay in one of the following ways:

$$\begin{aligned}\tilde{\chi}_2^0 &\rightarrow \tilde{l}l \\ &\rightarrow \tilde{\nu}\nu \\ &\rightarrow h^0\tilde{\chi}_1^0 \\ &\rightarrow Z^0\tilde{\chi}_1^0 \\ &\rightarrow l^+l^-\tilde{\chi}_1^0 \end{aligned} \tag{6.3}$$

The dominant $\tilde{\chi}_2^0$ and $\tilde{\chi}_1^{\pm}$ with respect to position in the $(m_0, m_{1/2})$ plane are shown in Figure 6.6.

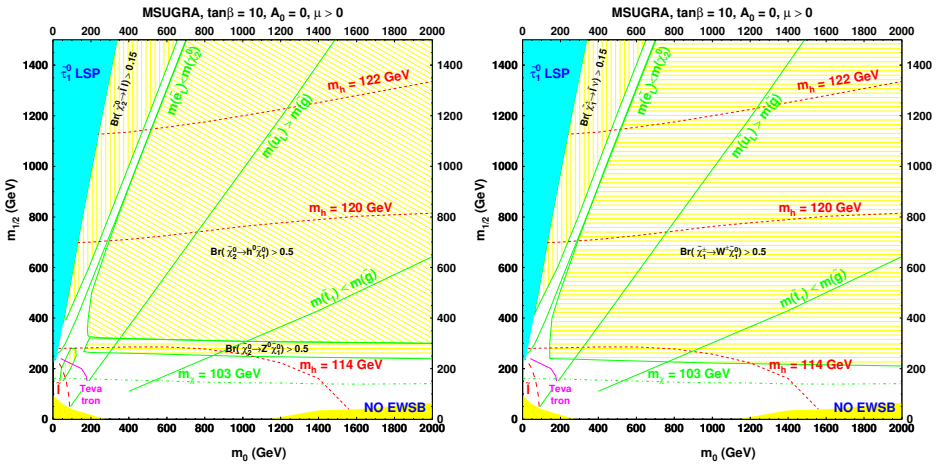

Figure 6.6: Regions of the $(m_0,\ m_{1/2})$ plane with main χ_2^0 decays (left) and main decays of $\chi_1^{\pm}$ (right) [30].

6.2.2 Sleptons

As seen in Section 6.1 and in Figure 6.4, the left sleptons are more massive than the right sleptons at any given point in the $(m_0, m_{1/2})$ plane. Because the mass splitting between left- and right- sleptons is proportional to $m_{1/2}$, as is the chargino and neutralino masses, the allowed decays of the sleptons will strongly depend on the region of mSUGRA parameter space. In the region where $m_0 > 0.4m_{1/2}$ the direct production of left sleptons can occur only through Drell-Yan interaction via W or Z as the left sleptons are heavier than the $\tilde{\chi}_1^{\pm}$ and $\tilde{\chi}_2^0$. The left sleptons then can decay to leptons plus chargino or neutralino, while the right slepton will decay to the LSP plus a Standard Model lepton. In the region $m_0 < 0.4m_{1/2}$, slepton production can proceed through chargino or neutralino decay [30].

6.2.3 Squarks and Gluinos

Because they strongly interact, squarks and gluinos are expected to dominate the SUSY production cross-section at the LHC. The resulting cascade decays through the sparticles ultimately lead to two LSPs, and results in the standard SUSY detector signature of leptons, multiple jets, and missing transverse energy. The typical gluino decays are discussed above. The $\tilde{q}_R$ will typically decay to a quark and the mostly Bino $\tilde{\chi}_1^0$, while the $\tilde{q}_L$ will typically decay through the $\tilde{\chi}_1^{\pm}$ or mostly Wino χ_2^0 [30].

6.3 Trigger Efficiency to Select LM1

The CMS trigger system is described in Section 3.3. At Level-1, the trigger is more than 90% efficient for leading muon p_T values above 20 GeV/c (Fig. 6.7). At Level-2, requirements on the muon chamber hits, vertex extrapolation, p_T, and η remain over 90% efficient. However, the Level-2 calorimeter isolation requirement reduces the trigger efficiency for LM1 to just above 60% at a muon p_T of 20 GeV/c, which may be the result of muons from semi-leptonic decays of b-jets often characteristic of SUSY at LM1. The remaining requirements at Level-3 on tracker hits, p_T, η, and

tracker isolation do not have strong differential effects on the HLT efficiency, but do reduce the overall efficiency for LM1 to just under 60% above a muon p_T of 20 GeV/c and improving to about 80% at a muon p_T close to 200 GeV/c.

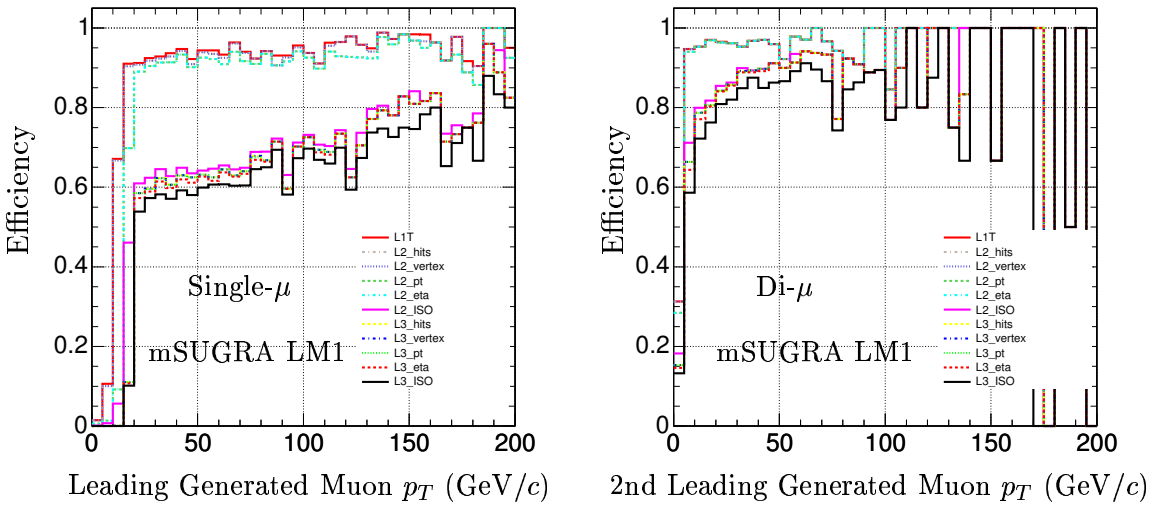

Figure 6.7: Left: Inclusive Muon Trigger Efficiencies for Level-1, Level-2, and Level-3 (HLT) versus the leading generated muon transverse momentum in mSUGRA LM1 events (for generated muons within the detector acceptance). Right: Di-muon Trigger Efficiencies for Level-1 (red), Level-2 (magenta), and HLT (black) versus the 2nd leading generated muon transverse momentum in mSUGRA LM1 events.

While this analysis does not use information from a possible second muon in the event, the effect of muon isolation requirements in the high-level trigger is clearly evident (Fig. 6.7). The Level-1 trigger efficency is excellent, above 95% for muon p_T above 10 GeV/c. However, after the Level-2 calorimeter isolation requirement, the efficiency drops to 70% for a muon p_T of 10 GeV/c, increasing to about 90% at 50 GeV/c. The additional tracker isolation requirement at Level-3 reduces the efficiency to 60% at a muon p_T of 10 GeV/c and 85% at a muon p_T of 50 GeV/c.

The leading muon behavior of the di-muon trigger compared with the inclusive muon trigger is qualitatively different, with a delayed Level-1 "turn-on" curve (Fig. 6.8). This is because there is little (but still non-zero) correlation between the leading and second leading muon and, even though the leading muon may be well

above the di-muon trigger threshold, the second leading muon may still lie below the di-muon trigger threshold for a large range of leading muon p_T values. The inefficiency of the calorimeter isolation requirement at Level-2 for LM1 is also evident in the di-muon trigger.

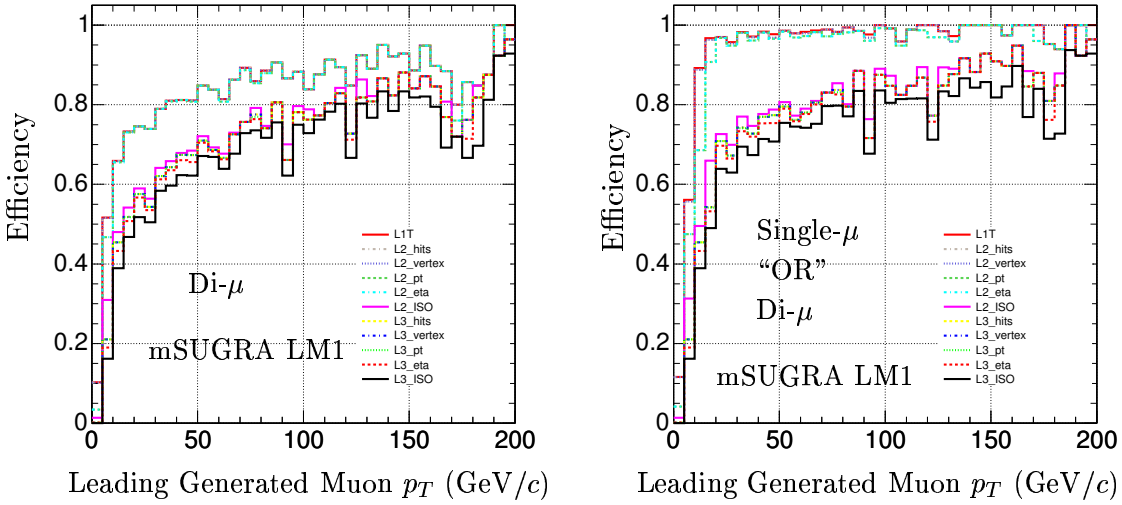

Figure 6.8: Left: Di-Muon Trigger Efficiencies for Level-1, Level-2, and Level-3 (HLT) versus the leading generated muon transverse momentum in mSUGRA LM1 events (for generated muons within the detector acceptance). Right: Efficiency for the "OR" of the single- and Di-muon Triggers for Level-1, Level-2, and Level-3 (HLT) versus the leading generated muon transverse momentum in mSUGRA LM1 events.

This analysis applies the "OR" of the single-muon trigger and the di-muon trigger and Figure 6.8 shows the resulting trigger efficiency for Level-1, Level-2, and Level-3 (HLT) versus the leading generated muon p_T for mSUGRA LM1 events. Table 6.2 shows the decomposition of the two triggers. Because the mSUGRA LM1 muon spectrum falls rapidly with increasing p_T, the overall trigger acceptance for the signal event is only 29.6 %. In 39.0 % of the triggered events, the single- and di-muon triggers come together. Inclusively, the single-muon trigger accounts for 80.2 % of the sample, whilst exclusively it accounts for 41.2 %. The di-muon trigger inclusively accounts for 58.8 % of the sample, whilst 19.8 % of the sample belongs exclusively to the di-muon triggered events.

Table 6.2: Decomposition for single- and di-muon triggers for the mSUGRA LM1 point.

Condition	Trigger	Events (%)
None	None	98 250 (100%)
At least one μ	None	38 966 (39.7%)
Inclusive	Single-μ "OR" Di-μ	11 550 (11.8%)
Inclusive	Single-μ "AND" Di-μ	4 501 (4.6%)
Inclusive	Single-μ	9 262 (9.4%)
Inclusive	Di-μ	6 789 (6.9%)
Exclusive	Single-μ	4 761 (4.8%)
Exclusive	Di-μ	2 288 (2.3%)

CHAPTER 7
STANDARD MODEL BACKGROUNDS

Several standard model processes contribute to final states with at least one muon accompanied by multiple jets and missing E_T. The main backgrounds studied in this analysis are multi-jet QCD production, $t\bar{t}$ production, and single- and di-boson electroweak production. The expected rates for these backgrounds are shown in Figure 3.2.

Because full next-to-leading (NLO) calculations do not yet exist for all background processes, this work uses only leading order (LO) cross sections consistently for both signal and all backgrounds. Further, PYTHIA is used to simulate all background processes studied in this work. Because the PYTHIA parton shower model for initial/final state radiation (ISR/FSR) is only realistic in the collinear approximation, the effect of high E_T ISR/FSR jets can be significantly underestimated in the backgrounds used by this study. Generators such as ALPGEN [59] and MC@NLO [60], which use a matrix element approach, provide a more realistic description of ISR/FSR jets. To account for this underestimation of some backgrounds due to high E_T ISR/FSR jets, a systematic uncertainty representing the difference between the parton shower model and the matrix element approach is estimated in Section. 10.

For all backgrounds considered, the Geant based OSCAR framework is used to fully simulate the response of the CMS detector to simulated particles from Pythia, and the ORCA framework is used to simulate the digitization of the detector hits and simultaneously super-impose pile-up at a luminosity of 2×10^{33} cm^{-2} s^{-1}.

7.1 Multi-Jet QCD Production

Multi-jet QCD events do not intrinsically involve Feynman diagrams producing final states similar to the topological signature required by this analysis (Fig. 7.1). Owing to its enormous cross section ($\sigma_{jj} \sim 55$ mb), however, multi-jet events can produce configurations which are experimentally close. For example, in addition to multiple jets, significant $\not\!\!E_T$ can be faked by mis-measurement of jet energies and muons can be produced in heavy flavor events or faked in several ways such as punch-through or charged pion/kaon decays.

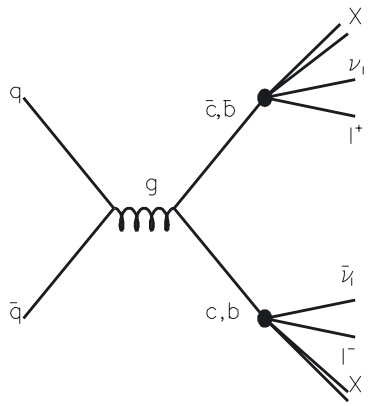

Figure 7.1: Diagram showing typical QCD process.

The number of multi-jet events expected for 10 fb^{-1} (Table 7.1 and Fig. 7.2) is so large at small $\hat{p}_T$ (defined as the transverse momentum of one of the two original hard scattered partons) that it is practically impossible to generate and simulate such a large amount of events. Consequently, events were generated almost uniformly in not less than 21 $\hat{p}_T$ bins (Fig. 7.2) and were given a weight equal to the ratio of the number of events expected to that actually generated in the corresponding bin.

7.2 Top ($t\bar{t}$) Production

Another particularly important source of background is $t\bar{t}$ production (Fig. 7.3), due to its modestly large cross section ($\sigma_{t\bar{t}} \sim 490$ pb at leading order) and its intrinsic multi-jet, high missing transverse energy, and significant leptonic final state nature. A

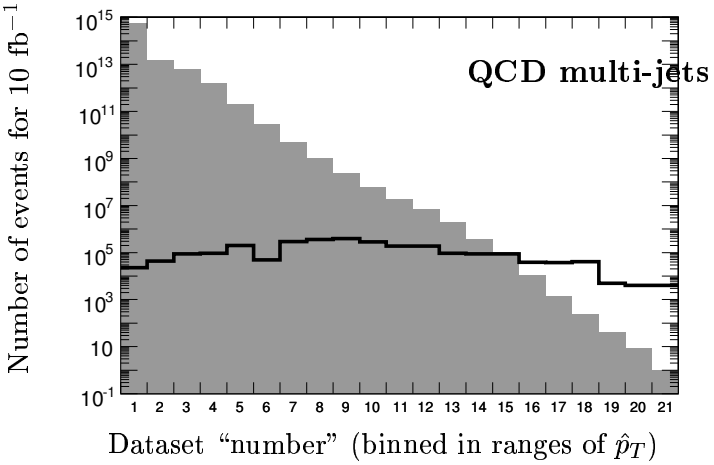

Figure 7.2: Numbers of events expected for 10 fb^{-1} (shaded area), and numbers of events produced (full curve) as a function of $\hat{p}_T$.

Table 7.1: Geant based, fully simulated QCD multi-jet background samples used in this work.

Process	Bin	p_T range (GeV/c)	$\sigma_{\mathtt{LO}}$ (pb)	N (10^3 events)	ΔL (fb^{-1})
QCD	1	$0 < \hat{p}_T < 15$	5.5×10^{10}	23	4.2×10^{-10}
QCD	2	$15 < \hat{p}_T < 20$	1.5×10^{9}	44	2.9×10^{-8}
QCD	3	$20 < \hat{p}_T < 30$	6.4×10^{8}	89	1.4×10^{-7}
QCD	4	$30 < \hat{p}_T < 50$	1.6×10^{8}	92	5.9×10^{-7}
QCD	5	$50 < \hat{p}_T < 80$	2.1×10^{7}	198	9.5×10^{-6}
QCD	6	$80 < \hat{p}_T < 120$	2.9×10^{6}	49	1.7×10^{-5}
QCD	7	$120 < \hat{p}_T < 170$	5.0×10^{5}	291	5.8×10^{-4}
QCD	8	$170 < \hat{p}_T < 230$	1.0×10^{5}	355	3.5×10^{-3}
QCD	9	$230 < \hat{p}_T < 300$	2.4×10^{4}	389	1.6×10^{-2}
QCD	10	$300 < \hat{p}_T < 380$	6.4×10^{3}	283	4.4×10^{-2}
QCD	11	$380 < \hat{p}_T < 470$	1.9×10^{3}	186	9.8×10^{-2}
QCD	12	$470 < \hat{p}_T < 600$	6.9×10^{2}	190	2.8×10^{-1}
QCD	13	$600 < \hat{p}_T < 800$	2.0×10^{2}	94	4.6×10^{-1}
QCD	14	$800 < \hat{p}_T < 1000$	3.6×10^{1}	89	2.5×10^{0}
QCD	15	$1000 < \hat{p}_T < 1400$	1.1×10^{1}	89	8.2×10^{0}
QCD	16	$1400 < \hat{p}_T < 1800$	1.1×10^{0}	39	3.7×10^{1}
QCD	17	$1800 < \hat{p}_T < 2200$	1.4×10^{-1}	38	2.6×10^{2}
QCD	18	$2200 < \hat{p}_T < 2600$	2.4×10^{-2}	41	1.7×10^{3}
QCD	19	$2600 < \hat{p}_T < 3000$	4.3×10^{-3}	5	1.2×10^{3}
QCD	20	$3000 < \hat{p}_T < 3500$	8.4×10^{-4}	4	4.7×10^{3}
QCD	21	$3500 < \hat{p}_T < 4000$	9.7×10^{-5}	4	4.1×10^{4}

total of approximately 3.3 million $t\bar{t}$ events were simulated and used in this analysis, as shown in Table 7.2.

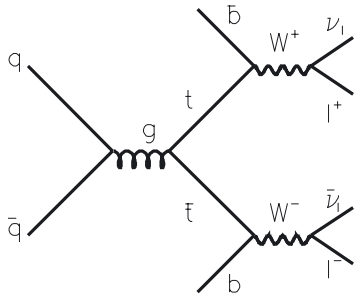

Figure 7.3: Diagram showing typical $t\bar{t}$ diagram.

Table 7.2: Geant based, fully simulated $t\bar{t}$ background samples used in this work.

Process	Bin	p_T range (GeV/c)	σ_{LO} (pb)	N (10^3 events)	ΔL (fb^{-1})
$t\bar{t}$	-	inclusive	4.9×10^2	3371	6.9

7.3 Single-Boson Electroweak Production with Jets

The production of single W and Z bosons is expected to be plentiful at the LHC due to their high cross sections (Fig. 7.4), $\sigma_{\text{W}} \sim 1.2 \times 10^5$ pb and $\sigma_{\text{Z}} \sim 3.3 \times 10^4$ pb (at leading order). Because it is nearly impossible to generate and simulate all the needed events for 10 fb^{-1}, the single-boson electroweak events (Fig. 7.5 and Table 7.3) were generated uniformly in 20 $\hat{p}_T$ bins, and were given a weight equal to the ratio of the number of events expected to the number of events generated for that bin.

Jets accompany single W and Z production due to, for example, t-channel-like ISR/FSR diagrams where one outgoing leg is teh W/Z and the other leg is a radiated gluon. As the PYTHIA parton shower model for initial/final state radiation is only realistic in the collinear approximation, the effect of high E_T jets fromr ISR/FSR can be significantly underestimated for this type of background.

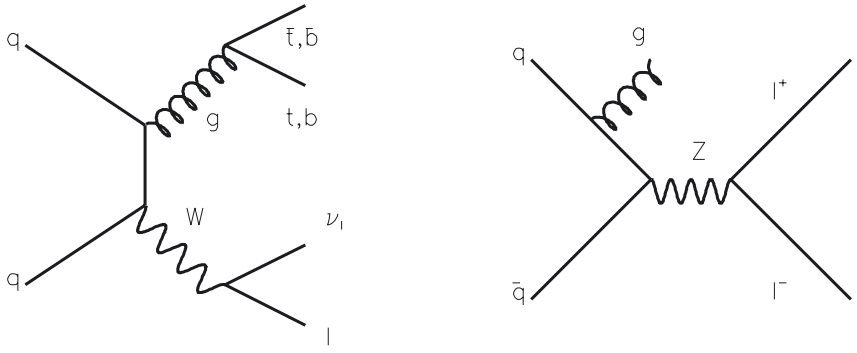

Figure 7.4: Typical W+jets diagram (left) and Z+jets diagram (right).

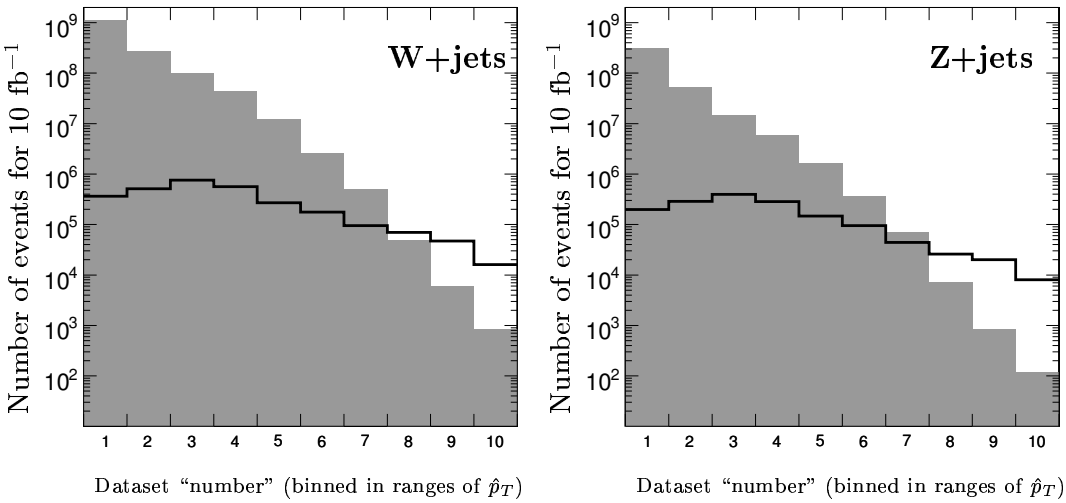

Figure 7.5: Numbers of events expected for 10 fb^{-1} (shaded area), and numbers of events produced (full curve) as a function of $\hat{p}_T$.

Table 7.3: Geant based, fully simulated Electro-Weak background samples used in this work.

Process	Bin	p_T range (GeV/c)	$\sigma_{\mathtt{LO}}$ (pb)	N (10^3 events)	ΔL (fb^{-1})
W+jets	1	$0 < p_T(W) < 40$	1.1×10^5	365	3.3×10^{-3}
W+jets	2	$10 < p_T(W) < 100$	2.7×10^4	513	1.9×10^{-2}
W+jets	3	$25 < p_T(W) < 170$	1.0×10^4	759	7.5×10^{-2}
W+jets	4	$42.5 < p_T(W) < 300$	4.3×10^3	565	1.3×10^{-1}
W+jets	5	$75 < p_T(W) < 500$	1.2×10^3	270	2.2×10^{-1}
W+jets	6	$125 < p_T(W) < 800$	2.6×10^2	177	6.7×10^{-1}
W+jets	7	$200 < p_T(W) < 1400$	4.9×10^1	95	1.9×10^0
W+jets	8	$350 < p_T(W) < 2200$	4.9×10^0	70	1.4×10^1
W+jets	9	$550 < p_T(W) < 3200$	5.9×10^{-1}	47	7.9×10^1
W+jets	10	$800 < p_T(W) < 4400$	8.3×10^{-2}	16	1.9×10^2
Z+jets	1	$0 < p_T(Z) < 40$	3.2×10^4	198	6.3×10^{-3}
Z+jets	2	$10 < p_T(Z) < 100$	5.2×10^3	288	5.6×10^{-2}
Z+jets	3	$25 < p_T(Z) < 170$	1.5×10^3	396	2.7×10^{-1}
Z+jets	4	$42.5 < p_T(Z) < 300$	5.8×10^2	283	4.9×10^{-1}
Z+jets	5	$75 < p_T(Z) < 500$	1.6×10^2	147	9.1×10^{-1}
Z+jets	6	$125 < p_T(Z) < 800$	3.7×10^1	95	2.6×10^0
Z+jets	7	$200 < p_T(Z) < 1400$	7.0×10^0	44	6.3×10^0
Z+jets	8	$350 < p_T(Z) < 2200$	7.1×10^{-1}	26	3.6×10^1
Z+jets	9	$550 < p_T(Z) < 3200$	8.5×10^{-2}	20	2.4×10^2
Z+jets	10	$800 < p_T(Z) < 4400$	1.2×10^{-2}	8	6.8×10^2

The primary contribution of W+jets as a background process to this study is due to leptonic decays of the W into a muon and a neutrino, thus mimicking the muon-plus-missing-energy-plus-jets signature of the signal. The primary contribution of Z+jets is due to leptonic decays of the Z into either di-muons, di-taus, or neutrinos, leading to large missing E_T (as measured in the calorimeters) accompanied by jets. The number of fully simulated and reconstructed electro-weak, single-boson events used in this work may be found in Table 7.3.

7.4 Electro-Weak Di-Boson + Jets

Di-boson production, such as WW + jets, WZ + jets, and ZZ + jets, also contributes as a source of background to this study, due to the existence of several final states involving muons, jets and large missing E_T (Fig. 7.6). Because of the additional weak vertex, the cross sections, while significant with respect to this study, are much less than for single boson production: $\sigma_{WW} \sim 190$ pb, $\sigma_{WZ} \sim 27$ pb, and $\sigma_{ZZ} \sim 10$ pb (all given at leading order). The number of fully simulated and reconstructed electro-weak di-boson events used in this work may be found in Table 7.4.

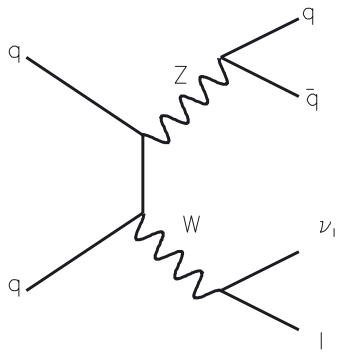

Figure 7.6: Diagram showing typical electroweak di-boson production of ZW + jets.

Table 7.4: Geant based, fully simulated di-Electro-Weak background samples used in this work.

Process	Bin	p_T range (GeV/c)	$\sigma_{\mathtt{LO}}$ (pb)	N (10^3 events)	ΔL (fb^{-1})
WW+jets	-	inclusive	1.9×10^2	483	2.6
WZ+jets	-	inclusive	2.7×10^1	276	10.3
ZZ+jets	-	inclusive	1.1×10^1	478	43.0

CHAPTER 8
PHYSICS OBJECT RECONSTRUCTION AND PRE-SELECTION

In this work, an excess of sypersymmetric events containing multi-jets, at least one μ, and large $\not\!\!E_T$, over that expected by Standard Model is sought. Below, a description of the reconstruction algorithms for each of these physics objects is given.

8.1 Muons

At CMS, muon reconstruction is performed in three steps: first the muon-detector-level track segments are found. For example, in the CSCs this is accomplished by using six layers of two-dimensional measurements in the anode wire group and cathode strip views. The wire groups provide coarse information in the η direction. The ϕ coordinate in each layer can be found by analyzing the charge distribution of a cluster of three neighboring strips, which is fitted to the "Gatti function" from which the precise position of the center of the charge distribution can be found. From the resulting six measurements within a chamber, a straight track-segment can be formed.

In the second step in muon reconstruction the track-segments are linked to form full muon tracks; third, these muon tracks are extended to include tracker data. The muon system provides the Level-1 trigger system four candidate tracks using the first two steps, completed with spatially coarse detector information suitable for fast track reconstruction. The reconstructed muons from the Level-1 system are then used to seed the High-Level trigger muon candidates. Track *seeds* define regions in the CMS detector volume of interest subject to more careful reconstruction. Using the full precision offered by the muon system, the HLT first performs *Standalone* muon reconstruction in the muon system only, and then extends these results to include the tracker in the *Global* muon reconstruction. The offline muon reconstruction seeds

muon candidates by using the full detector information in the muon system. A "forward" Kalman-filter technique is used, moving from the inner muon chambers to the outer muon chambers, followed by a "backward" Kalman-filter (moving outside to inside). The track is extrapolated to the nominal interaction point and a vertex constrained fit is performed. Next, the track is extrapolated to include hits in the silicon and pixel trackers. The list of final muon candidates is then made by cutting on the χ^2 of each trajectory. The selected candidates are then refit, excluding hits with high residual values in muon stations with high occupancy. Figures 8.1 and 8.2 show the reconstruction performance of the muon reconstruction algorithms.

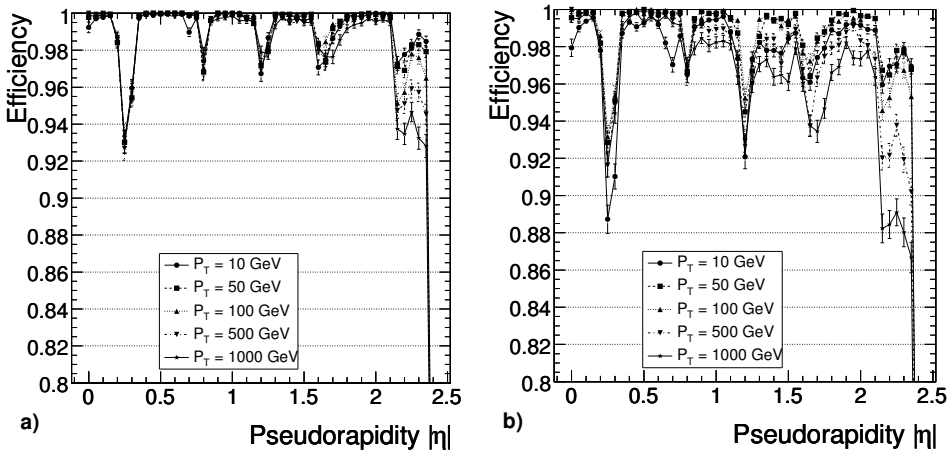

Figure 8.1: Muon reconstruction efficiency as a function of η for a) the Standalone reconstruction and b) the Global reconstruction [33].

Figure 8.3 shows that the efficiency to reconstruct muons for LM-1 as a function of both generated muon p_T and η is excellent: above 90% for p_T above 10 GeV/c and above 90% for most of $|\eta| < 2.4$.

8.2 Jets

Jets are reconstructed using an iterative cone algorithm applied to calorimeter towers in which the energy from electro-magnetic calorimeter (ECAL) and hadronic calorimeter (HCAL) are added together. Because the HCAL has a significantly coarser granularity than ECAL, a single HCAL tower in the barrel corresponds to 25

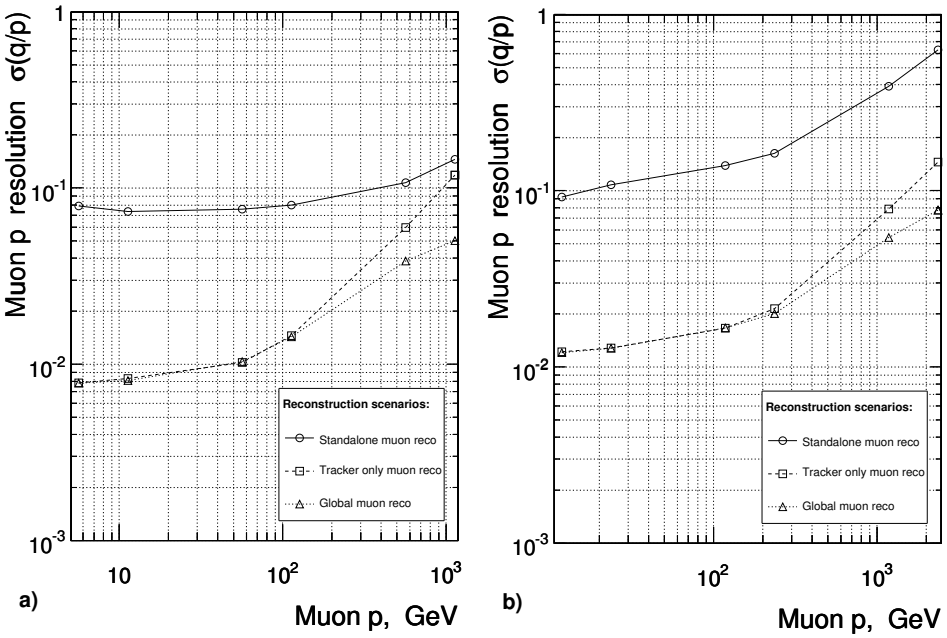

Figure 8.2: Muon reconstruction $1/p_T$ resolution as a function of momentum using the Global reconstruction in the region a) Barrel and b) Endcap [33].

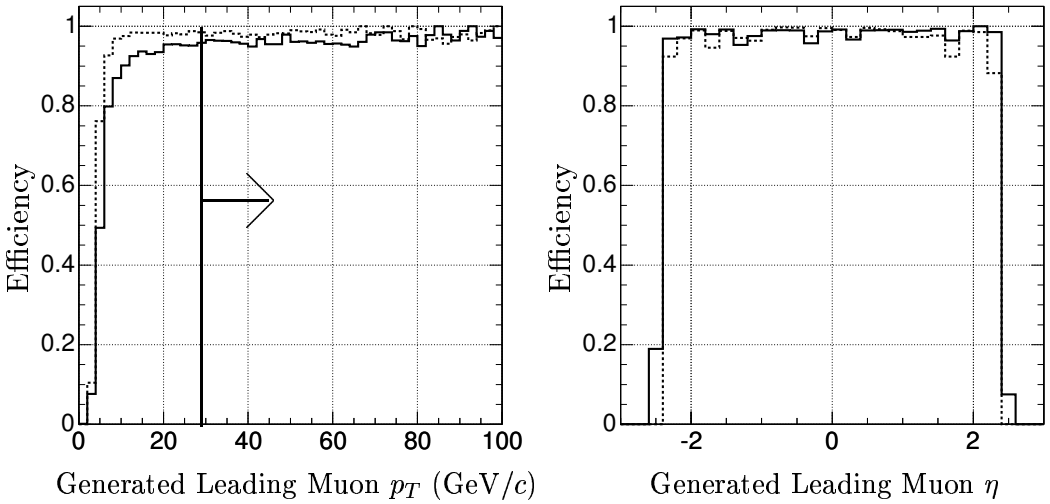

Figure 8.3: Global muon reconstruction efficiencies for ORCA (solid line) and FAMOS (dotted line) versus the generated transverse momentum (left) and eta (right).

(5x5) ECAL crystals; due to geometry considerations, a more complex association of HCAL towers to ECAL crystals is required in the end-caps. In this work, thresholds are applied to the input tower energy according to the expected η-dependent activity from underlying event (UE) effects.* A cone of size $R = 0.5$ in η, ϕ space around an input tower seed of at least 0.5 GeV is used to define a "proto-jet" and the so-called E_T scheme is used to calculate jet momenta, that is:

$$\begin{aligned} E_T &= \Sigma E_{T,i}, \\ \eta &= \frac{1}{E_T}\Sigma E_{T,i}\eta_i, \\ \phi &= \frac{1}{E_T}E_{T,i}\phi_i. \end{aligned} \tag{8.1}$$

An iterative procedure is then applied in which the direction of "proto-jets" seed new "proto-jets". Convergence to a "jet" is defined to occur once the change between iterations in proto-jet energies is less than 1% and $\Delta R < 0.01$. The list of towers used to define the "jet" is then removed from further consideration and the procedure is repeated until either no more seed towers exist with an E_T above 0.5 GeV or no jets with at least an E_T above 10 GeV can be formed. Each reconstructed jet is then calibrated using average corrections from photon-jet balancing, tuned for UE tower thresholds and low-luminosity pile-up [61]. Figure 8.4 shows the E_T resolution for the iterative cone algorithm.

The iterative cone algorithm does not allow for "splitting" or "merging" of jets. These features can be accomplished by the Midpoint-Cone algorithm, which is not used in this study. In the midpoint algorithm an iterative cone procedure is used to find proto-jets about towers above 0.5 GeV. After a proto-jet is defined, all input

*Low energy and instrumental background rates can effect jet reconstruction performance. For example, without the application of tower thresholds this noise can seed proto-jets, and unreasonably large number of jets can be formed, which may not actually correspond to actual particle jets. Therefore, thresholds need to be applied to towers to limit such effects. The so-called "underlying event" scheme applies thresholds as a function of η, based on the average noise contained in towers outside of reconstructed jets. The list of thresholds can be found in Reference [61].

objects remain on the input list, and therefore overlapping proto-jets. For overlapping proto-jets, the mid-point is calculated between them, and this is used to define a new proto-jet axis. After the full list of proto-jets is formed, overlapping pairs are checked to see if they share a large fraction of their respective E_Ts. If so, these objects are merged [61].

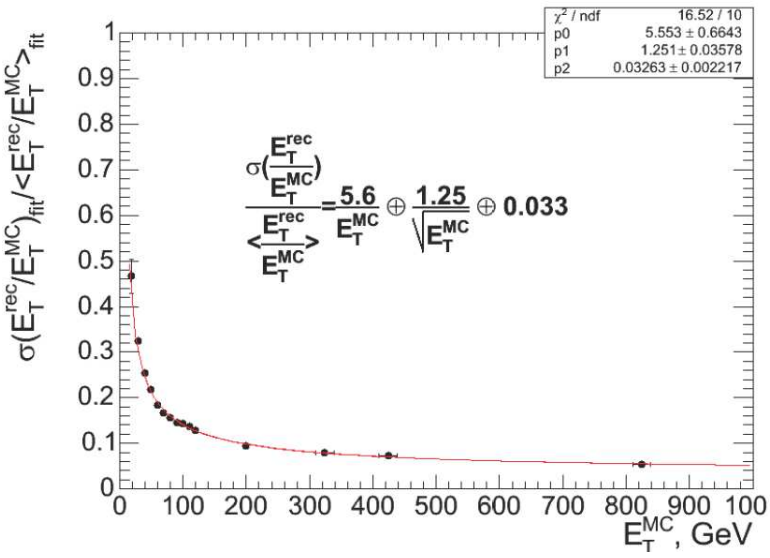

Figure 8.4: Jet transverse energy resolution plot for iterative cone algorithm (R = 0.5) for barrel region. Here the Monte Carlo jet calibration is applied. The resolution function has three coefficients: the first due to energy fluctuations in the cone from electronic noise, pile-up, and UE energy; the second is the stochastic response of the calorimeter measurements; the third is the constant term from non-uniformities and non-linearities in the detector response [61].

Figure 8.5 demonstrates that the ORCA efficiency to reconstruct interative cone jets is above 95% for E_T above 50 over a broad range of η using LM-1 data. Further, the FAMOS efficiency to reconstruct iterative cone jets is comparable to ORCA for jet E_T above 50 GeV.

8.3 Missing Transverse Energy

The missing transverse energy ($\not\!\!E_T$) of each event is constructed by taking the negative of the vector sum over all calorimeter towers projected in the plane transverse

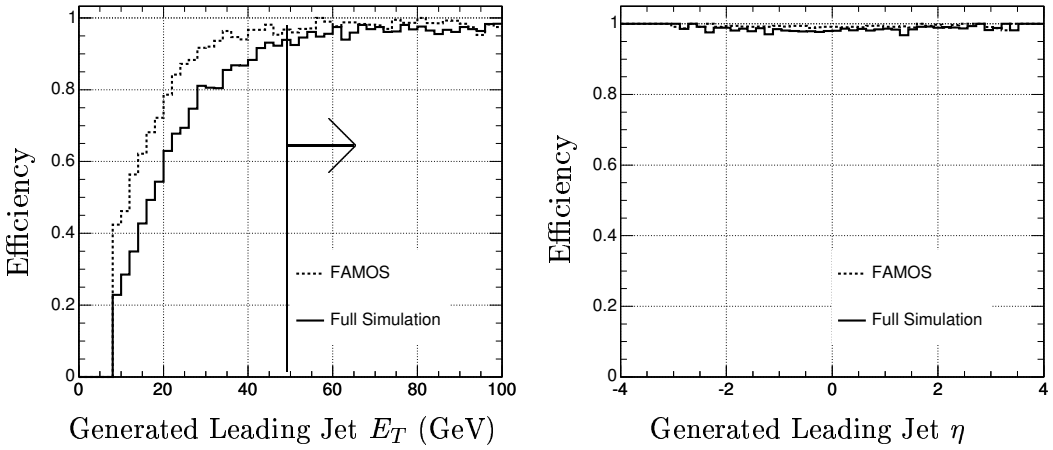

Figure 8.5: Left: Jet reconstruction efficiency for ORCA (solid line) and FAMOS (dotted line) versus the generated transverse energy. Right: Jet reconstruction efficiency for ORCA (solid line) and FAMOS (dotted line) versus the generated jet eta.

to the beam axis:

$$\begin{aligned} \not\!\!E_T &= -\Sigma(E_i \sin\theta_i \cos\phi_i \hat{i} + E_i \sin\theta_i \sin\phi_i \hat{j}) \\ &= \not\!\!E_x \hat{i} + \not\!\!E_y \hat{j}, \end{aligned} \tag{8.2}$$

where the sum runs over individual calorimeter towers with energy E_i, polar angle θ_i, and azimuthal angle ϕ_i. $\not\!\!E_T$ is a measure of the momentum imbalance of the event from long-lived particles escaping detection in the calorimeters, such as neutrinos, muons, or the lightest super-symmetric partner (LSP). Indeed, the missing transverse energy of the event is one of the most powerful discriminators for R-parity conserving SUSY models. Corrections to the $\not\!\!E_T$ due to minimum ionizing muons were investigated, but rejected due to uncertainties in the behavior of questionable high-p_T reconstructed muons which lead to long (sometimes unphysical) tails in the $\not\!\!E_T$ distribution (Fig. 8.6). Such "questionable" (or poorly reconstructed muons) may be due to punch-through as they tend to be non-isolated (well contained within a jet) and fake (without any match to a generated muon). Hence only the "raw" uncorrected calorimeter information is used to form the $\not\!\!E_T$.

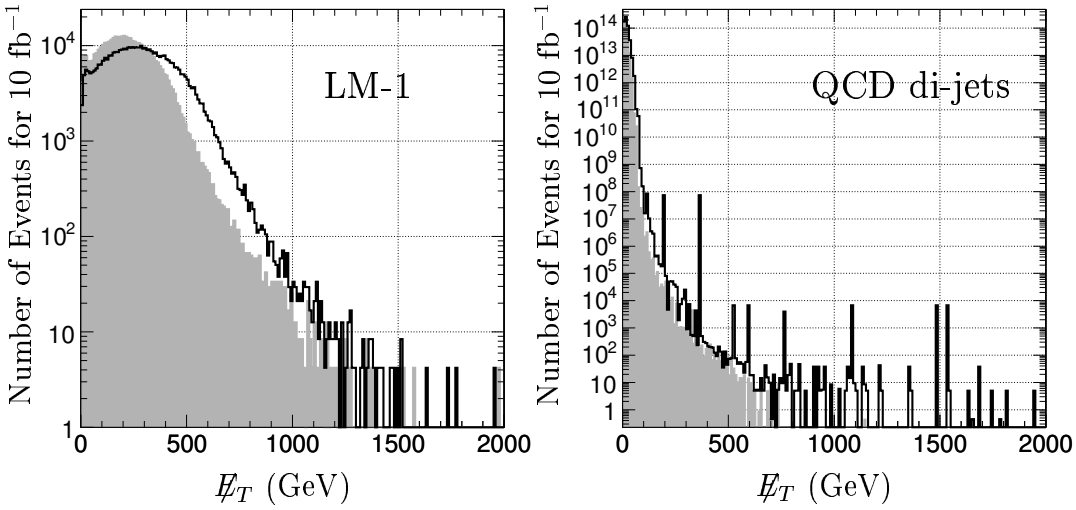

Figure 8.6: Comparison of Missing Transverse Energy with no corrections (shaded area) and with muon corrections (solid black line) for (left plot) mSUGRA LM-1 events and (right plot) QCD di-jet events. While the signal to background discrimination power of $\not\!\!E_T$ is greater when muon corrections are included, the spikes in the QCD di-jet plot correspond to highly weighted pthat QCD di-jet events which are dangerously promoted to high $\not\!\!E_T$ values due to badly reconstructed high transverse momenta muons.

In addition to well known resolution effects due to the sampling nature of the calorimeter, electronic noise and ambient environmental backgrounds (such as pile-up), as well as energy loss in the forward regions can also contaminate or contribute to fake $\not\!\!E_T$. Such effects, which are on average constant (or slowly varying), quickly fall in significance with increasing measured $\not\!\!E_T$. In order to minimize these effects, and because of the expected $\not\!\!E_T$ character of R-parity conserving SUSY, large measured $\not\!\!E_T$ is required in this study. Other important sources of fake $\not\!\!E_T$ are expected to arise from effects which are not included in the current simulations, including hot/dead calorimeter channels, cosmic muons, and non-collisional beam backgrounds due to halo particles. No quality pre-selection requirements are made on the $\not\!\!E_T$, instead requiring large $\not\!\!E_T$ in the event during the selection optimization. Cleaning $\not\!\!E_T$ at the LHC (due to non-collisional beam backgrounds, cosmic muons, electronic noise, hot/dead calorimeter channels, etc) is likely to be a challenging task, ultimately

requiring dedicated studies using real data. Some inspiration may be taken from the Tevatron [62, 63], however due to the 25 ns bunch spacing at the LHC and the large CMS detector volume, out-of-time effects become important in identifying non-collisional backgrounds and the applicability of the Tevatron methods can only be taken as suggestive strategies for cleaning $\not\!\!E_T$ at the LHC. To ensure a minimal understanding of the physics objects used in this work, quality criteria are applied to muons and jets. The leading muon is required to have a p_T above 30 GeV/c which ensures that the muon candidate is reconstructed with good efficiency, well above the thresholds of 19 GeV/c in the single-muon trigger and 7 GeV/c in the di-muon trigger (Figs. 6.7 and 8.3). Further, the leading muon is required to be isolated with less than 10 GeV of calorimeter energy within a cone of radius 0.3, reducing the effects due to fake muons, whilst preserving reasonable efficiency for signal acceptance (Fig. 8.7). The three leading jets must each have an E_T of at least 50 GeV which guarantees that jets are reconstructed with good efficiency (Fig. 8.5).

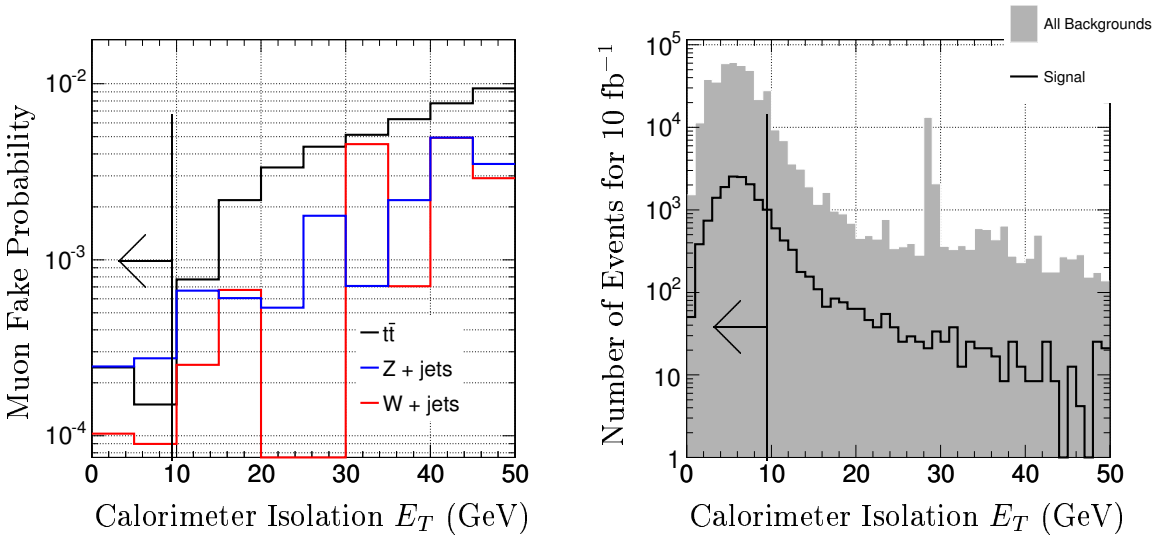

Figure 8.7: Left: Probability to reconstruct a fake muon versus the calorimeter transverse energy contained within a cone of radius 0.3 around the muon. Reconstructed muons are considered fake if they cannot be matched with a generator level muon in a cone of $R < 0.1$. The muon fake rate is determined by taking the ratio of the number of leading muons for each isolation transverse energy bin which cannot be matched, to the number of leading muons in each isolation transverse energy bin. Plot: Number of events for 10 fb^{-1} for signal and background having calorimeter transverse energy contained within a cone of radius 0.3 around the muon. The spike in backgrounds, just below 30 GeV, is due to a highly weighted event and does not correspond to any particular physical feature.

CHAPTER 9
DISCRIMINATING SIGNAL FROM BACKGROUND

This work uses the mSUGRA LM1 point as the signal benchmark for study and selection optimization. Figure 9.1 demonstrates some of the differences between the LM1 signal point (represented as a solid black line) and the sum of all Standard Model backgrounds (represented as the shaded area) before any trigger conditions and before any selection cuts have been applied. The soft QCD multi-jet background is clearly visible, producing 10 orders of magnitude more events than the signal. However, even with no trigger, the signal tends toward somewhat harder jets and particularly harder $\not\!\!E_T$ than the background. The observed spikes across the muon p_T spectrum are due to highly weighted (low $\hat{p}_T$) QCD multi-jet events.

Figures 9.2 and 9.3 display physics distributions relevant to this work, after the HLT trigger, event topology requirements, and physics object quality pre-selections have been applied: (1) HLT (single-muon "OR" di-muon) accept, (2) at least three reconstructed jets each with $E_T > 50$ GeV, and (3) at least one globally reconstructed muon with the leading muon satisfying $p_T > 30$ GeV/c and a calorimeter isolation requirement of $E_T < 10$ GeV within a cone of $R = 0.3$ around the muon. Owing to the relatively large LM1 cross section and the unlikelihood of QCD multi-jet events to match the above requirements, these simple pre-selection cuts already improve the signal to background ratio by roughly 7-8 orders of magnitude. The primary features which are exploited to separate signal from the remaining backgrounds are the distinctly harder jets and $\not\!\!E_T$ spectra, the centrality of the leading jets, as well as the azimuthal angles between the 1st and 2nd leading jets, and between the $\not\!\!E_T$ vector and the 1st and 2nd leading jets.

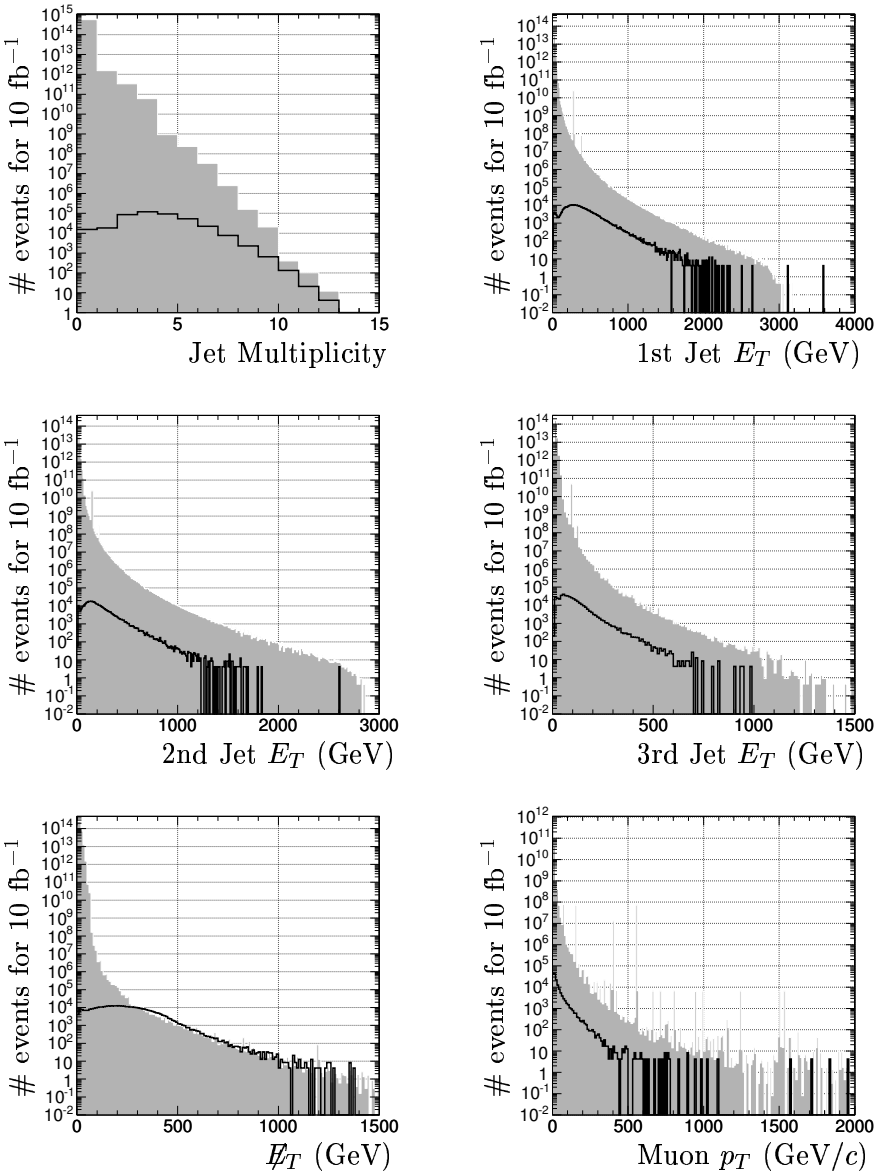

Figure 9.1: Physics distributions showing Standard Model background (shaded area) and the mSUGRA LM1 signal (solid black line) before any trigger or pre-selection cuts have been applied. The transverse energy of the three leading jets, the $\not\!\!E_T$ of the event, the transverse momentum of the leading muon, and the jet multiplicity are shown. In all plots, the number of events are luminosity scaled to 10 fb^{-1}. The spikes observed across the muon transverse momentum spectrum are due to highly weighted (low pthat) QCD multi-jet events.

Requiring central leading jets helps to distinguish heavy particles produced at rest from lighter mass particles, such as the W or Z, produced with a significant boost along the beam axis. The angular requirements are expected to be particularly effective against QCD multi-jets, since in such events the $\not\!\!E_T$ vector typically points in the direction of a mis-measured jet. Finally, as the muon p_T spectrum is relatively soft, when compared with the background, no additional tightening of the muon p_T cut is made when applying the final selection cuts.

The strategy employed in this analysis is to optimize the set of selection cuts based on an objective function which provides a reasonable estimate of the significance to exclude the Standard Model null hypothesis while explicitly including systematic uncertainties. By explicitly including the effect of systematic uncertainties in the optimization of selection cuts, the search will avoid regions of cut-space which are systematically challenging (e.g., require precise knowledge of backgrounds, energy scale, etc), optimizing the significance by minimizing both the statistical and systematic uncertainties simultaneously. Once an "optimal" cut-set is determined, the final significance to exclude the Standard Model null hypothesis is estimated using more robust statistical methods described in Section 11.2.

When background levels and systematic uncertainties are large, the significance (S_{OF}) is estimated for the number of signal and background events to be incompatible with a background only hypothesis as:

$$S_{OF} = \frac{N_{\mathtt{S}}}{\sigma_{\mathtt{B}}} = \frac{N_{\mathtt{S}}}{\sqrt{N_{\mathtt{B}} + (\delta N^1_{\mathtt{B}})^2 + (\delta N^2_{\mathtt{B}})^2 + ...}} \tag{9.1}$$

where $N_{\mathtt{S}}$ is the number of signal events passing all cuts, $N_{\mathtt{B}}$ is the total number of background events passing all cuts, and $\delta N^i_{\mathtt{B}}$ is an uncertainty in the total number of background events passing all cuts due to some systematic effect i. One clearly sees that the linear term underneath the square-root represents the square of the

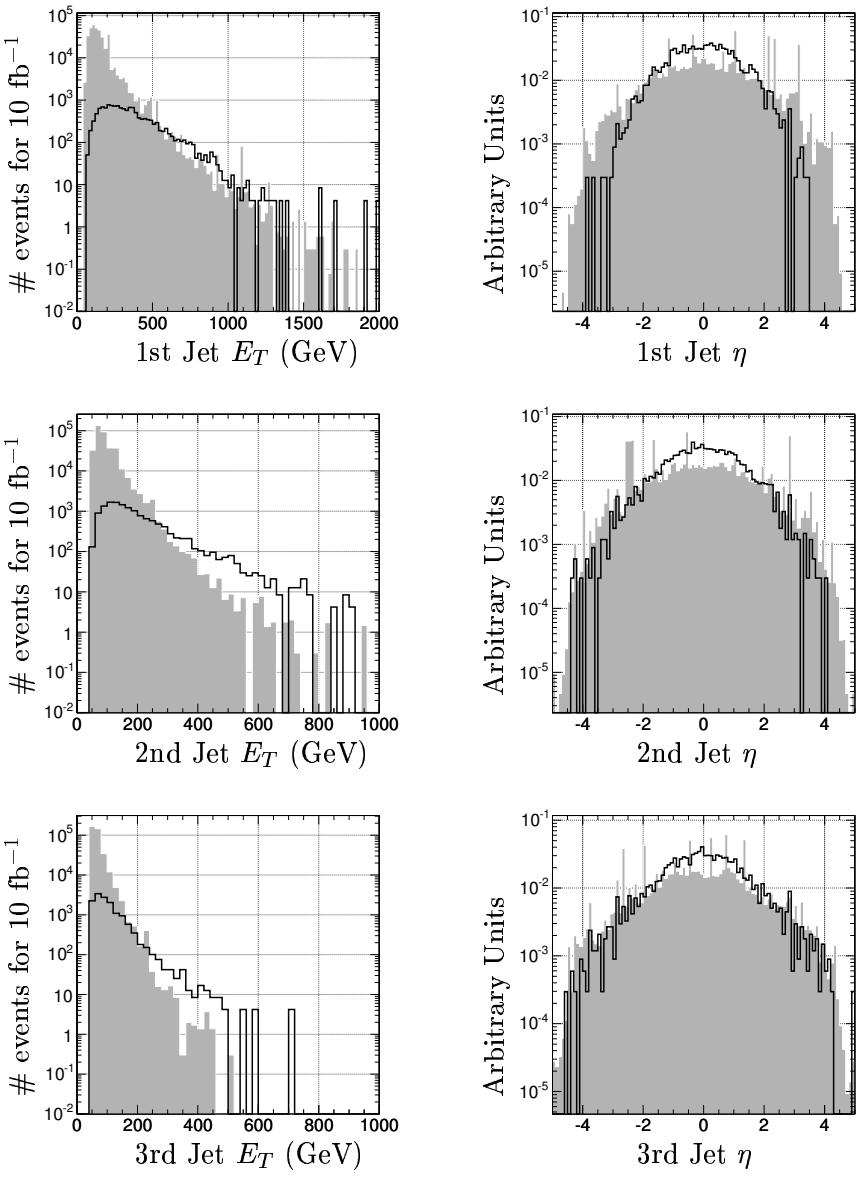

Figure 9.2: Physics distributions used for discriminating signal from background showing the Standard Model (shaded area) and the mSUGRA LM1 (solid black line) after the trigger and pre-selection cuts have been applied. The transverse energy of the three leading jets and their eta distributions are shown. In all plots, the number of events are luminosity scaled to 10 fb^{-1}. Spikes observed for the backgrounds in the angular plots are due to highly weighted events, and not to any particular physical feature.

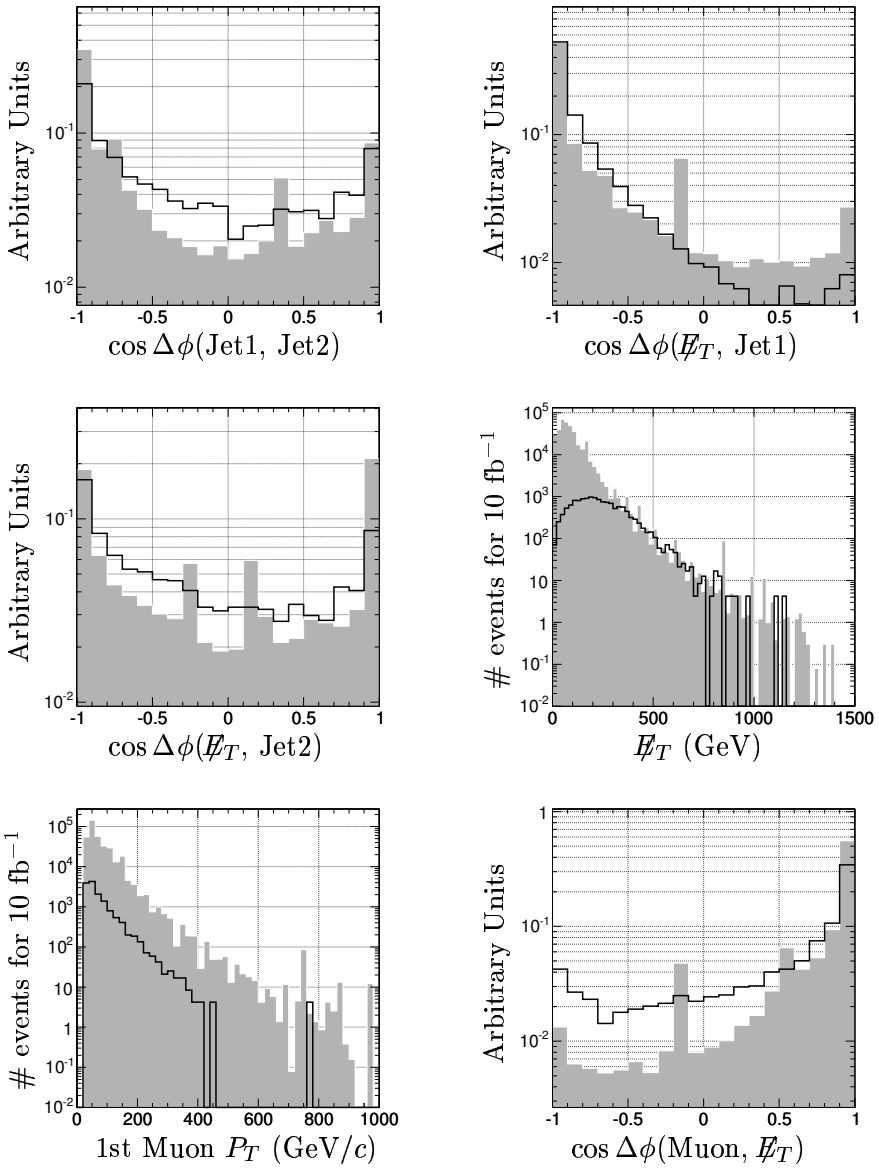

Figure 9.3: Physics distributions used for discriminating signal from background showing the Standard Model (shaded area) and the mSUGRA LM1 (solid black line) after the trigger and pre-selection cuts have been applied. The cosine of the difference in azimuthal angle between the two leading jets, the $\not\!\!E_T$ vector and the leading jet, and $\not\!\!E_T$ vector and the second leading jet are shown. The $\not\!\!E_T$ of the event, transverse momentum of the leading muon, and the cosine of the difference in azimuthal angle between the $\not\!\!E_T$ vector and the muon are also displayed. The distribution for cosine of the difference in azumathal angle between the leading muon and $\not\!\!E_T$ is only shown for reference and is not used in this work (since it is not well modeled in the CMS fast simulation). In all plots, the number of events are luminosity scaled to 10 fb^{-1}. Spikes observed for the backgrounds in the angular plots are due to highly weighted events, and not to any particular physical feature.

statistical uncertainty on the total background B while the quadratic terms represent the square of each systematic uncertainty, which are assumed to be both Gaussian and independent of each other.

CHAPTER 10
SYSTEMATIC UNCERTAINTIES

As systematic effects are explicitly included in the search for an "optimal" cut-set, the treatment of some systematic uncertainties before describing the final cut-set used to separate signal from background are discussed. As an example, the left plot of Figure 10.1 shows how systematic uncertainties can change with respect to, for example, a cut on $\not\!\!E_T$. In particular, one sees that there is a large uncertainty in the total number of events which pass low $\not\!\!E_T$ cut values. This can be due, for example, to events which carry a luminosity weighting of much greater than one; as one tightens the cut on $\not\!\!E_T$ to higher values, the systematic uncertainty (defined in the following sections) on the total number of background events decreases (1) because there are simply fewer events remaining, but also (2) because events which contribute a large uncertainty are removed. The left plot demonstrates that the effect of systematic uncertainties not only lowers the overall significance (sometimes dramatically), but also shifts the value of the optimal cut choice to regions which are better controlled.

10.1 Limited Amount of Simulated Data

Because the different Monte Carlo simulated samples used in this study were each produced with different integrated luminosities, the acceptance of each sample is determined after each sample has been scaled to an equivalent integrated luminosity of 10 fb^{-1}. The luminosity weighted number of events (for a given dataset) passing each cut is given by

$$N_w = \frac{\texttt{10fb}^{-1}}{L(\texttt{Gen})} N_{\texttt{Pass}} = w N_{\texttt{Pass}}, \tag{10.1}$$

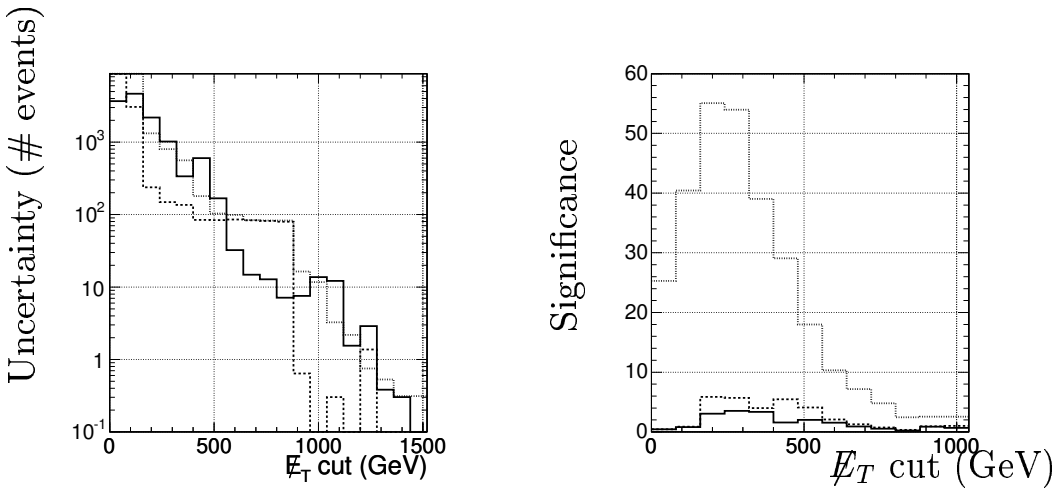

Figure 10.1: Left Plot: Systematic uncertainties (in total number of events passing) versus $\not\!\!E_T$ cut: jet energy scale (solid line), jet energy resolution (dashed line), and finite simulated events (dotted line). No other cuts have been applied, except the cut on MET. Right Plot: Significance after including different systematic effects versus $\not\!\!E_T$ cut and after pre-selection cuts: No systematic uncertainties (dotted line), systematic uncertainty due to using finite simulated events (dashed line), and systematic uncertainties due to jet energy scale and resolution (solid line). Not only do systematic effects lower the significance, they also shift the optimal cut choice for $\not\!\!E_T$ to higher values.

where $N_{\texttt{Pass}}$ is the unweighted number of events passing each cut assuming the luminosity of the generated sample, $L(\texttt{Gen})$, and w is the event weight. For high cross-section processes, it is difficult (sometimes impossible) to generate enough events. Hence, samples generated with a finite number of events, much less than the assumed 10 fb^{-1}, lead to highly weighted event samples and hence large uncertainties on the predicted background level

$$\delta N_w = \frac{\partial N_w}{\partial N_{\texttt{Pass}}} \delta N_{\texttt{Pass}} = w\sqrt{N_{\texttt{Pass}}} = \frac{N_w}{\sqrt{N_{\texttt{Pass}}}}. \tag{10.2}$$

As an example, Figure 7.2 shows that, while the QCD multi-jet cross section rapidly falls as a function of $\hat{p}_T$, the simulated QCD multi-jet datasets used in this analysis were generated approximately flat in $\hat{p}_T$. Indeed, one clearly sees the hopelessness of attempting to match the required 10 fb^{-1} luminosity by generating enough QCD multi-jet events at low $\hat{p}_T$. The uncertainty in predicting the QCD multi-jet events

background due to the finite amount of generated events for each QCD di-jets dataset is correspondingly large for events with low $\hat{p}_T$ values. By including δN_w in the objective function, the search for an optimal cut-set will thus avoid regions containing events belonging to Monte Carlo samples produced with very low luminosity. It is important to note that many of the Standard Model backgrounds, such as QCD multi-jet and electro-weak processes, will be measured at the LHC, and hence this systematic uncertainty represents our current ignorance which is expected to be mitigated somewhat by the time 10 fb^{-1} of data is collected.

10.2 Jet Energy Scale

This analysis uses the transverse energy of the three leading jets as well as the missing transverse energy of the event as variables which discriminate between the mSUGRA signal and the Standard Model background. Because the number of background events passing the $\not\!\!E_T$ cut falls steeply, while the number of signal events passing is flatter over a large range of $\not\!\!E_T$ cuts, even small uncertainties in the jets and $\not\!\!E_T$ scale can lead to large uncertainties in the background acceptance and the corresponding estimated significance for possible discovery. Reference [64] estimates that by 10 fb^{-1} of integrated luminosity, the CMS jet energy scale (JES) will be calibrated to within 3% via a W mass constraint in semi-leptonic $t\bar{t}$ events. Accordingly, a scaling of all reconstructed jet E_T's and the $\not\!\!E_T$ by 3% (assuming 100% correlation between the reconstructed jet E_T's and the reconstructed $\not\!\!E_T$ as supported by Figure 10.2) is applied.

The number of events which pass the systematically altered case is compared with the number of events which pass the unaltered case and the corresponding systematic uncertainty, due to jet energy scale, is then taken as the difference between the two cases:

$$\delta N_{\mathrm{B}}^{\mathrm{JES}\pm 3\%} \approx N_{\mathrm{B}}^{\mathrm{JES}\pm 3\%} - N_{\mathrm{B}}. \tag{10.3}$$

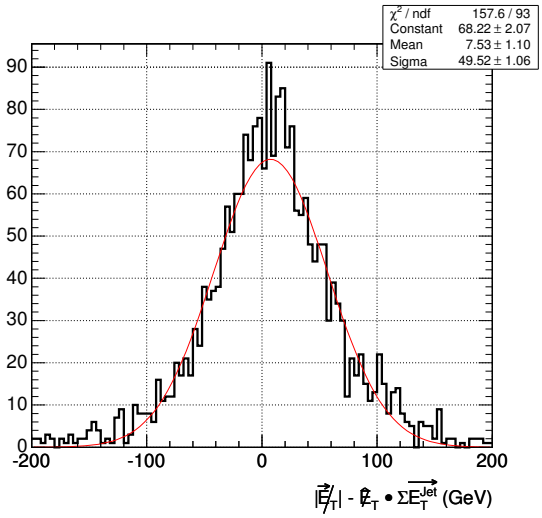

Figure 10.2: Distribution showing the difference between missing transverse energy and projected sum of jet transverse energies using LM1 data. If the $\not\!\!E_T$ is on average primarily determined by the Jet transverse energy values, then one expects that the vector sum of the $\not\!\!E_T$ with all other Jet transverse energy values should be, on average, be close to zero. The figure is centered around 7 GeV and demonstrates that, on average, the $\not\!\!E_T$ scale dominated by the Jet transverse energy scale. For high Jet transverse energies and high MET, assuming 100% correlation in the scale uncertainties also follows the CMS recommendation.

10.3 Jet Energy Resolution

Similar to the jet energy scale, uncertainties in the jet energy resolution can lead to systematic uncertainties in the estimated significance for possible discovery. With 10 fb^{-1} of integrated luminosity, the resolution of CMS jet energies are expected to be known to within 10% via di-jet balancing. Accordingly, a Gaussian smearing is applied to all reconstructed jet transverse energies, according to the below formula. The $\not\!\!E_T$ is assumed to be 100% correlated with the jets, and so the $\vec{\not\!\!E}_T$ two-vector is correspondingly modified, event-by-event, according to the smeared jet energy.

$$E_T^{\mathrm{Jet}i} \rightarrow E_T^{\mathrm{Jet}i} + 0.1 \;\; \mathtt{Gaussian}[1,0] \;\; \sigma(E_T^{\mathrm{Jet}i}) \tag{10.4}$$

$$\vec{\not\!\!E}_T \rightarrow \vec{\not\!\!E}_T - \sum_i \Delta\vec{E}_T^{\mathrm{Jet}i} \tag{10.5}$$

The number of events which pass in the systematically altered case is compared with the number of events which pass in the unaltered case and the systematic uncertainty, due to jet energy resolution, is then taken as the difference between the two cases.

$$\delta N_{\mathrm{B}}^{\mathrm{JER}\pm 10\%} \approx N_{\mathrm{B}}^{\mathrm{JER}\pm 10\%} - N_{\mathrm{B}} \tag{10.6}$$

10.4 Muon Identification Efficiency and Fake Rate

The systematic uncertainty in the muon p_T, due to uncertainties in the magnetic field, is $\delta p_T = 0.5\% p_T$ and translate to a negligible uncertainty in the efficiency to trigger and reconstruct muons (based on LM1) in this analysis.

The probability of fake muons which pass the calorimeter isolation cut and so contributing to this analysis is less than 3×10^{-4}. The systematic uncertainty on the fake muon rate is assumed, ad hoc, to be 10% of the probability observed in the simulation, which leads to a negligible uncertainty on the rate of backgrounds passing the selection cuts due to fake muons.

10.5 Effect of Fake $\not\!\!E_T$ due to Beam Halo Background

The amount of beam halo affecting physics event data, may arise primarily from either (1) a beam halo particle arriving in coincidence with an event triggered solely due an actual hard scattering process or (2) promoting a min-bias event, which would not have normally triggered the event. Since this work uses only the single- and di-muon triggers, the 2nd scenario (as it only affects the jets and $\not\!\!E_T$ triggers) is neglected. According to Reference [65], the rate of beam-halo events with $\not\!\!E_T$ above 25 GeV is estimated to be 1250 Hz and corresponds to a probability of 3×10^{-5} that any given (25 ns) bunch crossing contains such a beam halo particle. Since this analysis uses the muon triggers, the probability that any given bunch crossing contains a single- or di-muon triggered event *together* with a beam halo event is approximately 2×10^{-11}. By integrating over all bunch crossings up to 10 fb^{-1} of data and applying all

selection cuts, except those involving $\not\!\!E_T$, the total number of expected background events containing a superimposed beam halo particle is estimated to be 2×10^{-3}, or much less than one event. Hence, the systematic uncertainty associated with a superimposed beam-halo particle, which could possibly promote a background event originally having $\not\!\!E_T < 105$ GeV beyond the selection cut of $\not\!\!E_T > 130$ GeV, is negligible and taken to be zero.

10.6 Theory

Since this analysis is performed consistently at leading order, the inclusion of higher order effects involving ISR/FSR is not taken into account in this work. The parton shower method used by Pythia [50] to model ISR/FSR effects in this work is known to generate realistic ISR/FSR only in the collinear approximation. On the other hand, the matrix element method used by Alpgen [59], Comphep [66], etc, (which are not used in this work) generates a more realistic ISR/FSR spectrum for higher p_T, but is collinear divergent. Only a full NLO generator, such as MC@NLO [60], is able to treat both the infra-red and the ultra-violet parts of the ISR/FSR p_T spectrum realistically.

In order to roughly estimate the effect of NLO-like corrections from ISR/FSR, a generator-level comparison of the parton shower method for inclusive $t\bar{t}$ used by Pythia with the matrix element calculation for $t\bar{t}$ + 1−jet from Comphep [66] is performed. Since the two leading jets in this work are very hard (each above 440 GeV), it is assumed that differences in the modeling of ISR/FSR will primarily affect the efficiency of the E_T cut on the third leading jet. The effect the efficiency to select the third jet is then estimated by comparing inclusive $t\bar{t}$ events simulated with a parton shower method from PYTHIA with $t\bar{t}$ + 1−jet events simulated using a full matrix element calculation from CompHEP. The full matrix element calculation increases the relative acceptance of $t\bar{t}$ + 1−jet events by approximately 10%, which is taken as a systematic uncertainty due to ISR/FSR.

In addition to ISR/FSR, other theoretical effects involving (1) pile-up, (2) underlying event and (3) parton distribution function (PDF) uncertainties are each conservatively assumed to be at the level of 5% based on results from other CMS studies [67]. Hence, assuming all effects to be uncorrelated, a total systematic uncertainty of 13% is estimated due to theoretical uncertainties. The rough estimate of 13% theoretical uncertainty for this work primarily reflects the expectation that by the time CMS has collected 10 fb^{-1} of data, the QCD scale should be known to next-to-leading order and PDF uncertainties should be understood at a similar level as at the Tevatron, where uncertainties are also typically 5-10%. Appendix C briefly describes a strategy to normalize the electroweak background estimates to first data which allows these systematics to be avoided.

10.7 Luminosity

Reference [33] indicates that once approximately 10 fb^{-1} of integrated luminosity has been collected by CMS, the uncertainty in measuring that integrated luminosity is estimated to be $\sim 5\%$. Accordingly, a 5% smearing effect is included in the final significance calculation.

10.8 Differences Between the CMS Full and Fast Simulation and Reconstruction

Because the fast simulation, FAMOS, may not accurately simulate all aspects of the various physics distributions used by this work accurately as the detailed simulation as accurately as the detailed simulation (Figures 10.3 to 10.5), the signal selection efficiencies determined for a series of benchmark points (LM1, LM4, LM5, LM6, and HM1) with both simulations are compared. This comparison is displayed in Table 10.1, which shows that the average ratio between full and fast simulated efficiencies is found to be $(5.4 \pm 2.2)\%$. This difference does not appear to systematically depend on the benchmark point chosen, within the statistical accuracy of the test.

All FAMOS efficiencies were therefore reduced by 5.4% and a systematic uncertainty of 2.2% assigned to this number.

Table 10.1: Efficiencies to select different validation/benchmark mSUGRA points between FAMOS and OSCAR/ORCA.

	$\epsilon^{\mathtt{sel}}_{\mathtt{FAMOS}}$	$\epsilon^{\mathtt{sel}}_{\mathtt{ORCA}}$	$\epsilon^{\mathtt{sel}}_{\mathtt{ORCA}}/\epsilon^{\mathtt{sel}}_{\mathtt{FAMOS}}$
LM1	$(0.078 \pm 0.009)\%$	$(0.078 \pm 0.009)\%$	$(100.2 \pm 16.0)\%$
LM4	$(0.150 \pm 0.012)\%$	$(0.147 \pm 0.012)\%$	$(97.6 \pm 11.6)\%$
LM5	$(0.304 \pm 0.018)\%$	$(0.307 \pm 0.017)\%$	$(100.8 \pm 8.1)\%$
LM6	$(0.721 \pm 0.028)\%$	$(0.775 \pm 0.027)\%$	$(107.4 \pm 5.2)\%$
HM1	$(3.02 \pm 0.05)\%$	$(2.72 \pm 0.05)\%$	$(90.1 \pm 2.6)\%$
Average			$(94.6 \pm 2.2)\%$

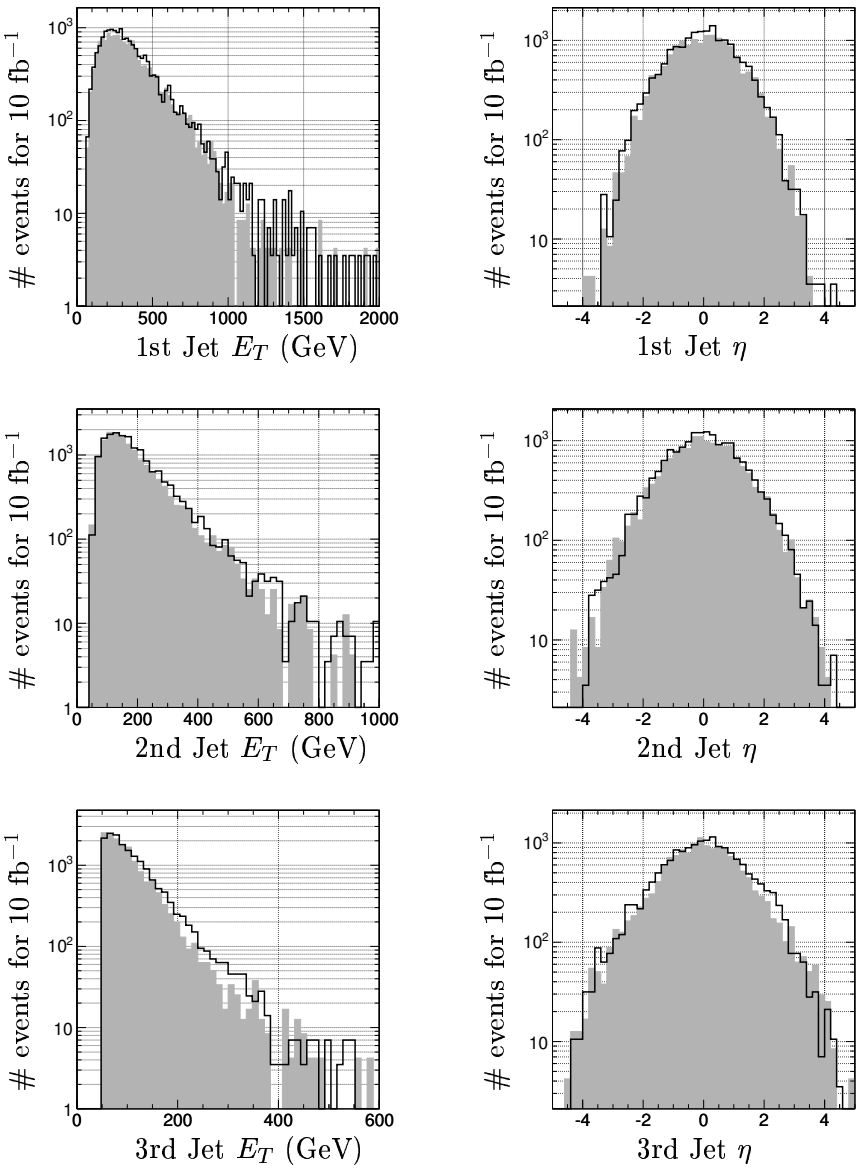

Figure 10.3: Comparison of FAMOS (shaded area) with ORCA (solid black line) for different reconstructed quantities used in this analysis. The Jet transverse energy for the first three leading jets and their eta distributions are shown. Quality pre-selection cuts have been applied.

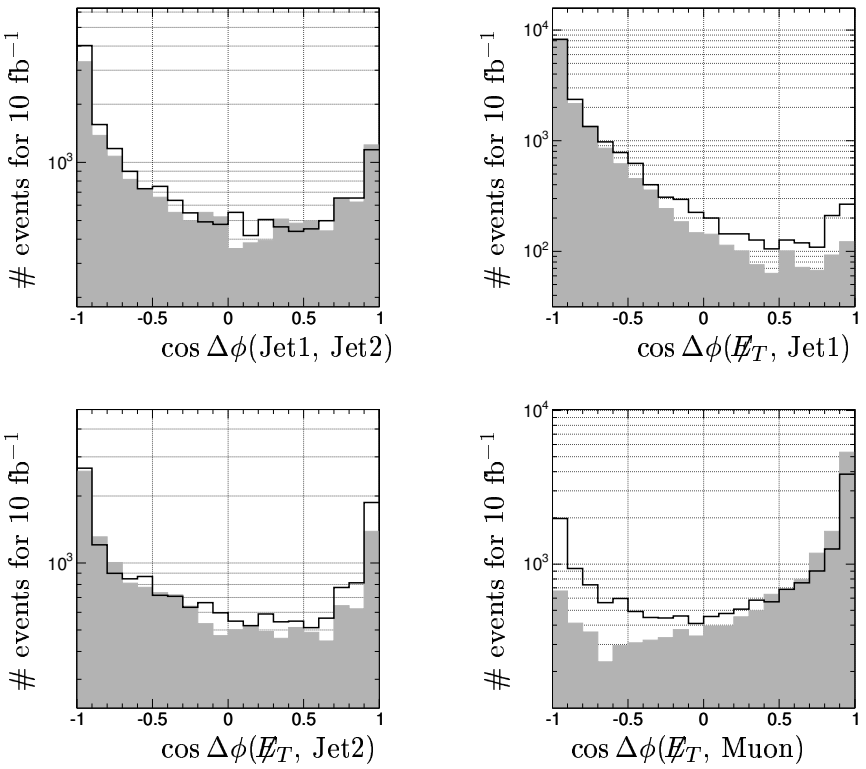

Figure 10.4: Comparison of FAMOS (shaded area) with ORCA (solid black line) for different reconstructed quantities used in this analysis. The cosines between the first two leading Jet transverse energies, missing transverse energy and the leading Jet transverse energy, missing transverse energy and the second leading Jet transverse energy, and missing transverse energy and the leading muon transverse momentum are shown. Quality pre-selection cuts have been applied. The cosine of the difference in azimuth between $\not\!\!E_T$ and the leading muon distribution is not used in this work because of the disagreement between FAMOS and ORCA.

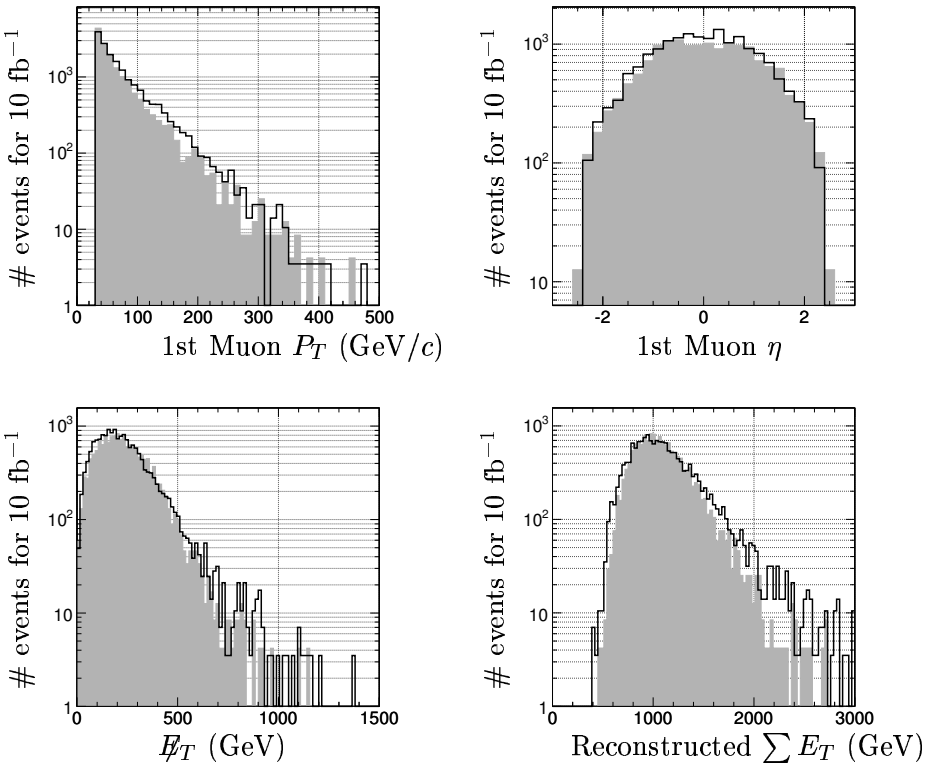

Figure 10.5: Comparison of FAMOS (shaded area) with ORCA (solid black line) for different reconstructed quantities used in this analysis. The leading muon transverse momentum and its eta distribution, the event missing transverse energy, and the sum of the transverse energy is shown. Quality pre-selection cuts have been applied. The cosine of the difference in azimuth between $\not\!\!E_T$ and the leading muon distribution is not used in this work because of the disagreement between FAMOS and ORCA.

CHAPTER 11
RESULTS

11.1 Search for Signal

There are several variables which may be used to help discriminate the SUSY signal from the Standard Model background as described in Section 9. A genetic algorithm tool, known as GARCON [68], is used to search the multi-dimensional space of cuts. The optimization is accomplished by maximizing the optimization function N_S/σ_B for potential discovery, where σ_B is the total uncertainty on the estimated number of background events passing a given cut-set. The systematic effects included in σ_B are described in the previous chapter.

The genetic algorithm randomly and coarsely samples the kinematic parameters used in the cut optimization, defining a space of particular combinations of cuts. Points in this space of cuts which result in the highest significance values are given priority. The priority cut sets are then used to further identify other potentially interesting points in the cut-space by either "crossing" (i.e. exchanging certain cuts between cut sets) or "mutating" (i.e. randomly changing a certain cut value in a single cut set). These new "generation" of cuts are then applied to the samples and the process is repeated until the cut-set which gives the maximum significance value is found, or until a "catastrophic event" occurs (i.e. start the entire process again, to escape from a local maximum). Further details can be found in [68].

This procedure for finding the best cut-set offers a good alternative to systematically probing every possible combination of cuts, which can be computationally prohibitive. Further, by including systematic uncertainties in quadrature with the statistical uncertainty on N_B, regions with large total uncertainties are avoided.

A total of 12 variables, corresponding to those displayed in Figures 9.2 and 9.3, are provided as input to the genetic algorithm, and the pre-selection described in 8.3 and the results of that search, are displayed in Table 11.1. The genetic algorithm probes points in cut-space by applying all cuts simultaneously. Nevertheless, in order to illustrate the plausibility and effectiveness of the genetic algorithm cut-set solution, Figure 11.1 show the effect of applying individual cuts in a particular (but arbitrary) sequence. Table 11.2 shows the cut efficiencies for LM1 and the Standard Model backgrounds: Appendix B contains a detailed accounting of the Signal and Background cut efficiencies.

Table 11.1: All selection cuts as applied in this work. First category: Trigger. Second Category: Event Topology and Quality Pre-selection Cuts. Third Category: Final signal selection cuts determined by the genetic algorithm. The effect of the cuts on the angles between the jets and $\not\!\!E_T$ vector is to require well separated quantities.

Trigger	single-μ "OR" di-μ	=	"Accept"
Pre-selection	N_μ	$\geq$	1
	$P_T^{\mu 1}$	$>$	30 GeV/c
	μ calo. iso. $(R = 0.3)$ E_T	$<$	10 GeV
	$N_{\texttt{jets}}$	$\geq$	3
	Jet E_T	$>$	50 GeV
Selection	$\not\!\!E_T$	$>$	130 GeV
	Jet1 E_T	$>$	440 GeV
	Jet2 E_T	$>$	440 GeV
	$\lvert\eta^{J1}\rvert$	$<$	1.9
	$\lvert\eta^{J2}\rvert$	$<$	1.5
	$\lvert\eta^{J3}\rvert$	$<$	3
	-1 $<$ cos $\left[\Delta\phi(\text{Jet1, Jet2})\right]$	$<$	0.2
	-0.95 $<$ cos $\left[\Delta\phi(\not\!\!E_T, \text{Jet1})\right]$	$<$	0.3
	-1 $<$ cos $\left[\Delta\phi(\not\!\!E_T, \text{Jet2})\right]$	$<$	0.85

11.2 Estimator used for Significance Calculation

Table 11.3 shows the final list of all systematics considered in this analysis. The dominant uncertainty in this work is from an inability to precisely predict the number

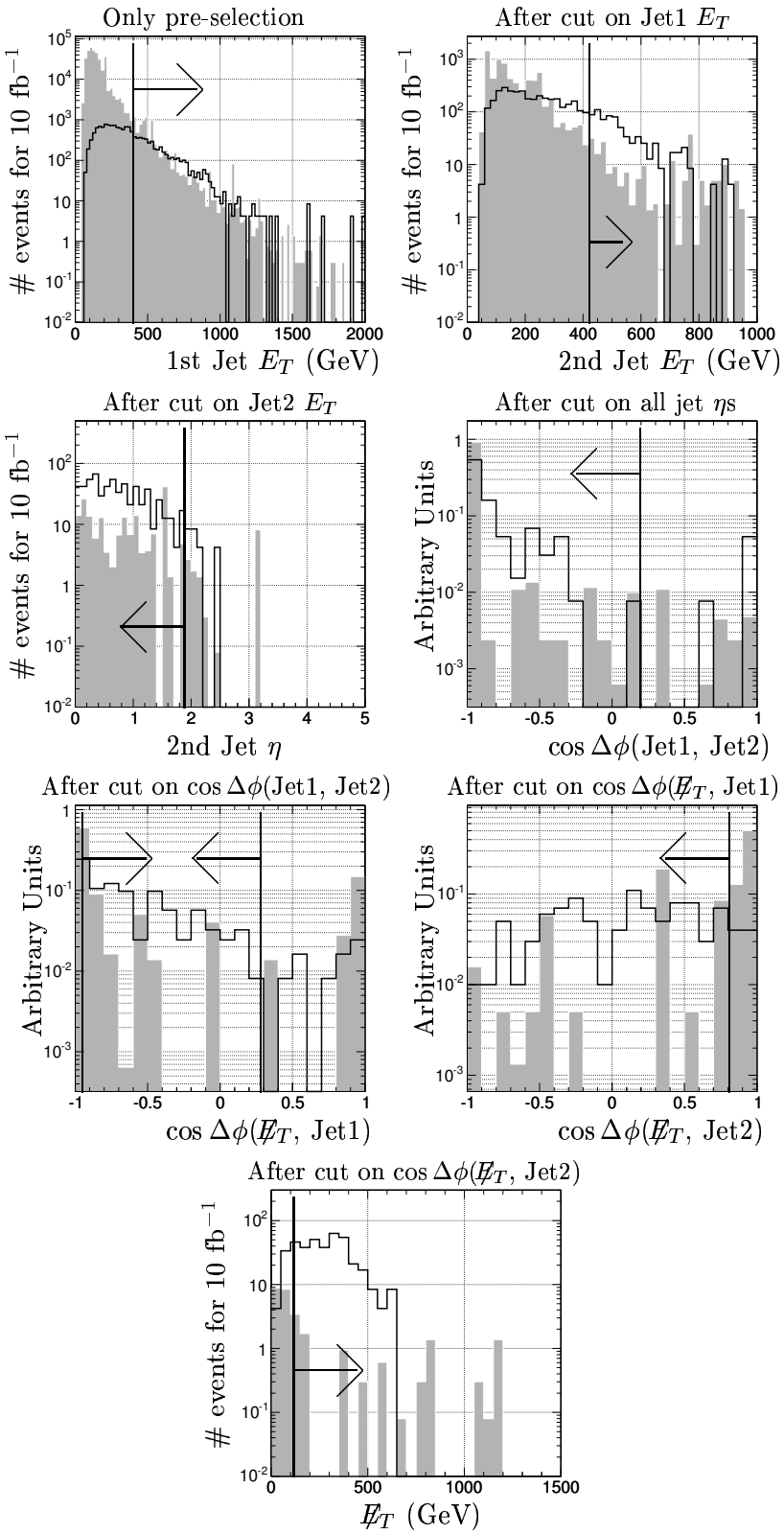

Figure 11.1: Sequence of plots (left to right, top to bottom) showing the effect of applying the cut-set solution as derived from the genetic algorithm.

Table 11.2: Summary of the efficiency to select the LM1 mSUGRA signal compared with the sum of all Standard Model backgrounds considered. The cuts are applied in the same sequence, moving down the table. The remaining cross section (given in fb) after cumulative cuts is shown along with the cut efficiency in parentheses. Systematic effects corresponding to the limited number of simulated events, jet energy scale, and jet energy resolution are explicitly included in the optimization function for the cut optimization. Hence, even though some cuts appear to have similar statistical efficiency for both the LM1 signal and SM background, they are still effective in reducing the systematic uncertainty.

	LM1	SM
x-sect[fb]	4.195×10^4	5.743×10^{13}
$P_T^{\mu 1}$	4545(10%)	$7.383 \times 10^7 (< 1\%)$
$\mu_1(ISOE_T < 10)$	2426(53%)	$5.26 \times 10^7 (71\%)$
$N_{jets}(E_T > 50)$	1566(64%)	$3.769 \times 10^4 (< 1\%)$
E_T^{J1}	406.2(25%)	327.1(1%)
E_T^{J2}	65.6(16%)	53.61(16%)
η^{J1}	63.92(97%)	50.09(93%)
η^{J2}	56.77(88%)	44.59(89%)
η^{J3}	55.93(98%)	31.34(70%)
$cos(\Delta\phi(J1, J2))$	52.56(93%)	31.13(99%)
$cos(\Delta\phi(\not{E}_T, J1))$	40.79(77%)	8.137(26%)
$cos(\Delta\phi(\not{E}_T, J2))$	38.69(94%)	3.397(42%)
$\not{E}_T$	32.8(84%)	0.3666(11%)
HLT	31.12(94%)	0.2544(69%)

of background events, due to the limited number of simulated events. It should be noted that by the time 10 fb^{-1} of data is collected, many of the contributing background processes will be measured from real data, thereby reducing the systematic uncertainty due to predicting background levels from a finite number of simulated events.

Table 11.3: List of systematic uncertainties considered in this work.

Systematic	Uncertainty ($\delta N/N$)
Jet Energy Scale	10%
Jet Energy Resolution	5%
Luminosity	5%
Theory	13%
ORCA vs FAMOS	2%
Simulation Statistical Uncertainty	32%
Background Total	36%
Background Total (no sim. stat. uncert.)	18%

The above systematic uncertainties are incorporated into the significance calculation in the following way. The Poisson probability to observe N events, assuming a Standard Model hypothesis of B, is:

$$p(N|N_{\text{B}}) = \frac{N_{\text{B}}^{N}}{N!}\exp[-N_{\text{B}}]. \tag{11.1}$$

It is assumed that the number of predicted background events N_{B} may be factor k different from the unknown "true" background b, due to some systematic uncertainty. Because the prediction for N_{B} is often close to zero, the number of "true" background events b is considered to have a log-normal distribution about the prediction N_{B}:

$$f(b|N_{\text{B}}) = \frac{1}{\sqrt{2\pi}\ \ln k}\exp\Big[-\frac{1}{2}\Big(\frac{\ln b - \ln N_{\text{B}}}{\ln k}\Big)^{2}\Big], \tag{11.2}$$

hence the probability density to observe N, assuming a Standard Model prediction for N_{B} and including uncertainties due to systematics, is:

$$\phi(N|N_{\mathrm{B}}) = \int_0^\infty p(N|b) f(b|N_{\mathrm{B}}) db. \tag{11.3}$$

The incompatibility of the signal plus background ($N_{\mathrm{S}} + N_{\mathrm{B}}$) with the background only hypothesis (N_{B}) is then estimated by converting the one-sided tail, $P(N_{\mathrm{B}})$,

$$P(N_{\mathrm{B}}) = \int_{N_{\mathrm{S}}+N_{\mathrm{B}}}^\infty \phi(N|N_{\mathrm{B}}) dN, \tag{11.4}$$

to a Gaussian equivalent significance using a look-up table.

11.3 Reach for 10 fb^{-1}

Table 11.4 shows the main results of this study. As indicated in Tables B.1 and B.2, the Standard Model backgrounds considered in this study have a very low efficiency, $\sim 10^{-7}$%, to pass the final selection cuts given in Table 11.1. However, due to their high cross sections, background contamination into the signal region is still possible and is estimated to be 2.5 Standard Model events, with a total systematic uncertainty of 18%, not including the statistical uncertainty due to the finite number of simulated events. It is anticipated that by the time 10 fb^{-1} of data has been collected, many of the backgrounds in question (such as W+jets) will have been measured (for example, using the method outlined in Appendix C), enabling the results to be calibrated to real data and thus reducing the statistical uncertainty due to simulated backgrounds. For the different fully simulated low mass mSUGRA points and 10 fb^{-1} of data, the selection cuts (which are optimized to select the LM1 point) achieve a separation of signal from background with a statistical significance of between $\mathcal{O}(20)\sigma$ and $\mathcal{O}(30)\sigma$, including systematic uncertainties. Such a large significance merely indicates that the low mass mSUGRA region will either have been discovered or excluded, long before 10

fb^{-1} of data is collected. Shortly after the LHC start-up, the systematic understanding of the CMS detector is expected to be quite different than what is presented in this work, which assumes $L = 10$ fb^{-1}. Nevertheless, if one assumes a similar systematic understanding and extrapolates the results of this work to early running, the expected luminosity required to discover the LM1 mSUGRA study point would be $\mathcal{O}(0.1)$ fb^{-1}. Hence, provided a sufficient understanding of detector systematic uncertainties is quickly achieved, low mass SUSY is a prime candidate for possible discovery during the very early running of the LHC. The significance for possible discovery for high mass SUSY, represented by the fully simulated HM1 point, with 10 fb^{-1} of data appears to be challenging, but possible with a potential of 5σ.

Table 11.4: Total number of background and signal events which pass the LM1 optimized selection cuts for 10 fb^{-1}, together with the corresponding significance (with and without systematic uncertainties) to discover the different signal benchmark points. "S_{CL}" represents the significance calculated according to the log-likelihood ratio method and "S" represents the significance calculated using the Lognormal-Poisson integration described in the text.

	Events (10 fb^{-1})	S_{CL} without syst.	S with syst. (no sim. stat. uncert.)	S with syst. (incl. sim. stat. uncert.)
QCD	0	-	-	-
$t\bar{t}$	0.7	-	-	-
W+jets	1.6	-	-	-
Z+jets	0.3	-	-	-
WW+jets	0	-	-	-
WZ+jets	0	-	-	-
ZZ+jets	0	-	-	-
Total	2.5	-	-	-
ORCA LM1	311	>37	34.1	32.3
ORCA LM4	246	>37	29.4	27.2
ORCA LM5	165	32.5	23.0	20.2
ORCA LM6	277	>37	31.7	29.5
ORCA HM1	13	5.4	5.0	4.2
FAMOS LM1	278	>37	33.1	29.8
FAMOS LM4	243	>37	29.1	27.0
FAMOS LM5	156	31.3	22.2	19.4
FAMOS LM6	244	>37	29.2	27.1
FAMOS HM1	13	5.4	5.0	4.2

Figure 11.2 shows the 5σ reach of this analysis, plotted in the mSUGRA (m_0, $m_{1/2}$) plane, assuming 10 fb^{-1}. Since by the time 10 fb^{-1} of data is collected additional events will have been simulated and many of the important backgrounds will have been measured using actual data, this plot displays the CMS reach when the uncertainty due to finite simulated events is not included. For low m_0, the 5σ contour (assuming 10 fb^{-1}) reaches approximately $m_{1/2} \approx 900$ GeV/c^2, rapidly dropping to ~ 700 GeV/c^2 near $m_0 = 500$ GeV/c^2 and slowly decreasing to $m_{1/2} \approx 600$ GeV/c^2 near $m_0 = 2$ TeV/c^2. By comparing with Figure 11.4, this result shows that CMS can observe SUSY mass scales of over ~ 1.5 TeV/c^2 given 10 fb^{-1} of data. For comparison, Figure 11.3 displays the CMS reach when the uncertainty due to finite simulated events is included.

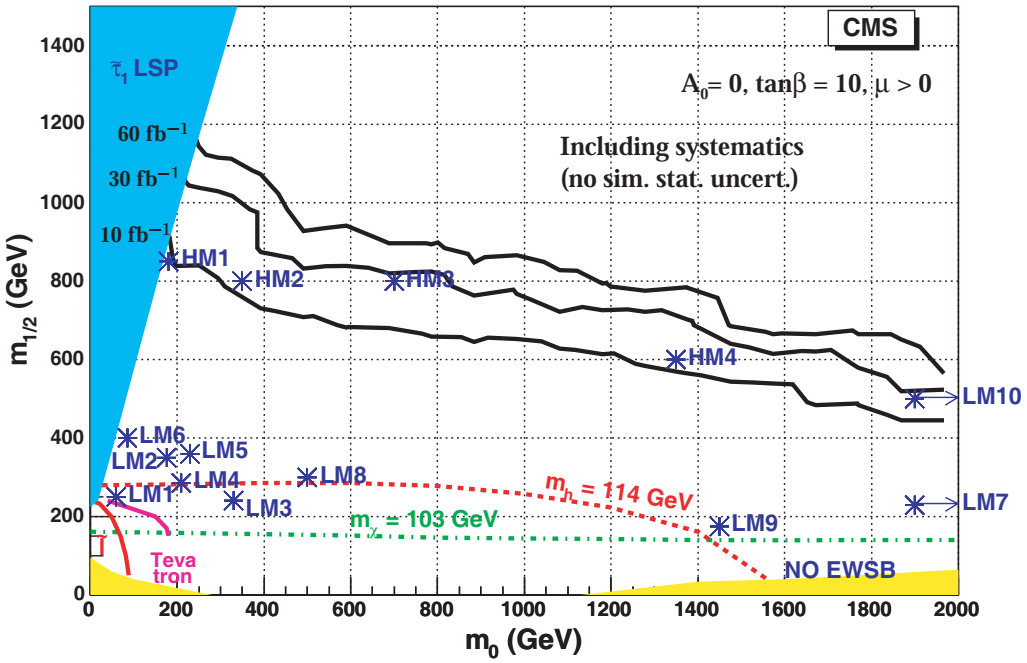

Figure 11.2: The inclusive muon 5σ CMS reach contours in the (m_0, $m_{1/2}$) plane for 10 fb^{-1}, 30 fb^{-1}, and 60 fb^{-1} including systematics, but without considering the uncertainty due to finite simulated events. The reach curve for 10 fb^{-1} is optimized to select the point LM1; the reach curves for 30 fb^{-1} and 60 fb^{-1} are optimized to select the point HM1. Both reach contour plots assume fixed mSUGRA parameters of: $A_0 = 0$, $\tan\beta = 10$, and $\mu > 0$.

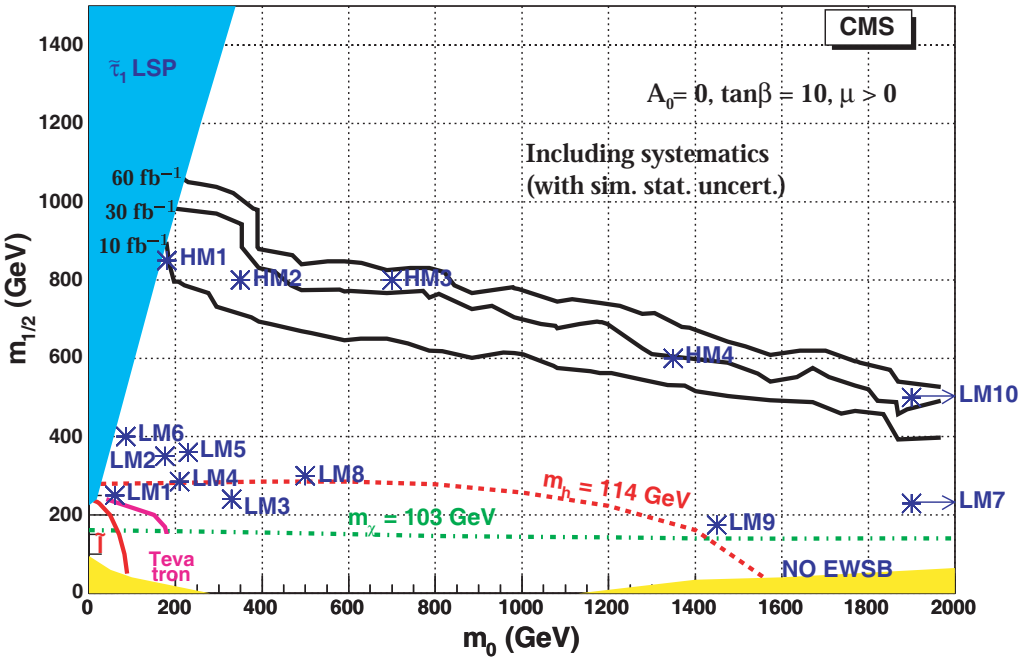

Figure 11.3: The inclusive muon 5σ CMS reach contours in the (m_0, $m_{1/2}$) plane for 10 fb^{-1}, 30 fb^{-1}, and 60 fb^{-1} including systematics (with the uncertainty due to finite simulated events). The reach curve for 10 fb^{-1} is optimized to select the point LM1; the reach curves for 30 fb^{-1} and 60 fb^{-1} are optimized to select the point HM1. Both reach contour plots assume fixed mSUGRA parameters of: $A_0 = 0$, $\tan\beta = 10$, and $\mu > 0$.

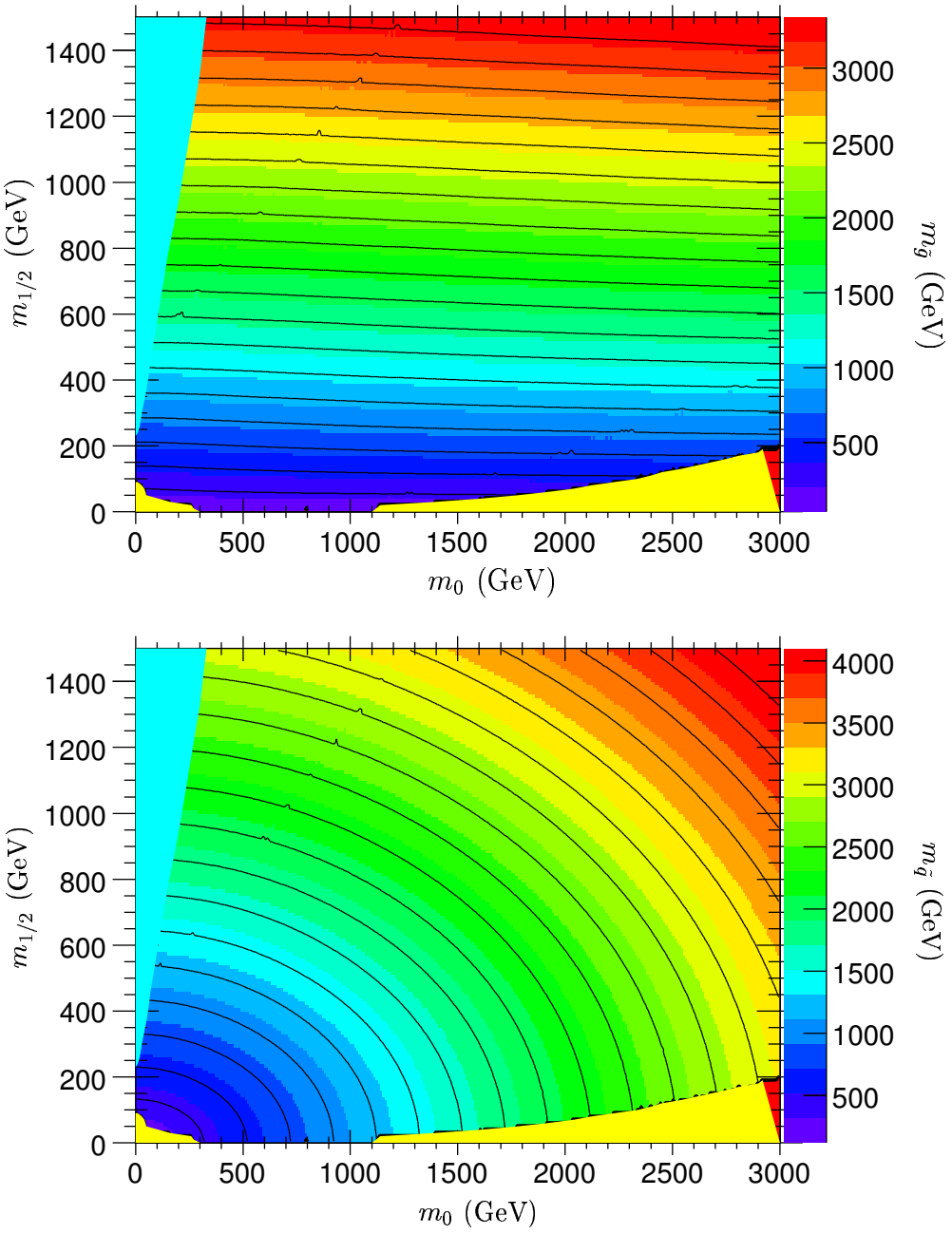

Figure 11.4: The top plot displays the iso-mass contours for different gluino masses as a function of universal scalar-gaugino mass. The bottom plot displays the iso-mass contours for different squark masses as a function of universal scalar and gaugino mass. Both plots assume fixed mSUGRA parameters of: $A_0 = 0$, $\tan\beta = 10$, and $\mu > 0$.

11.4 Reach beyond 10 fb^{-1}

As argued in the above section, CMS will have either discovered or excluded the lower mass region well in advance of the time required to collect 10 fb^{-1} of data. Therefore, a sensible approach to optimize the search in the mSUGRA plane for beyond 10 fb^{-1} integrated luminosity is to target regions near the 5σ contour which are just beyond detection for 10 fb^{-1} . Hence, the selection cuts are re-optimized to select the HM1 mSUGRA point assuming $L = 100$ fb^{-1} (to facilitate a comparison with Reference [69]) and the results are listed in Table 11.5. To estimate the reach for 30 fb^{-1} and 60 fb^{-1}, this same cut-set is applied. These cuts result in an estimated Standard Model background yield of $N_{\mathtt{B}} = 0.25$ for 30 fb^{-1}, and $N_{\mathtt{B}} = 0.49$ for 60 fb^{-1}. Hence, assuming, 30 fb^{-1} of integrated luminosity, several of the high mass CMS SUSY benchmark points become interesting for possible discovery (Fig. 11.2). Assuming 60 fb^{-1} of integrated luminosity and comparing Figure 11.4, CMS is able to reach SUSY mass scales of up to ~ 2 TeV/c^2.

Table 11.5: Cuts optimized to select HM1 as determined by the genetic algorithm for 100 fb^{-1}. The standard trigger and quality pre-selection cuts are implicit.

$\not\!\!E_T$	$>$	210 GeV
Jet1 E_T	$>$	730 GeV
Jet2 E_T	$>$	730 GeV
$\cos\left[\Delta\phi(\text{Jet1, Jet2})\right]$	$<$	0.95
$\cos\left[\Delta\phi(\not\!\!E_T, \text{Jet1})\right]$	$<$	-0.19
$\cos\left[\Delta\phi(\not\!\!E_T, \text{Jet2})\right]$	$<$	0.95

Even though pile-up conditions are expected to be different for 100 fb^{-1} of collected data, in order to compare with previous CMS studies, the 5σ reach for 100 fb^{-1} (neglecting systematics) is also plotted in Figure 11.5. This figure shows that the reach compares well with the results presented in Reference [69] (which did not include systematic uncertainties) for similar (but not exact) mSUGRA parameters ($A_0 = 0$,

$\tan\beta = 2$, $\mu > 0$); Reference [69] optimizes selection cuts for each point in the (m_0, $m_{1/2}$) plane, and therefore should have slightly better reach potential.

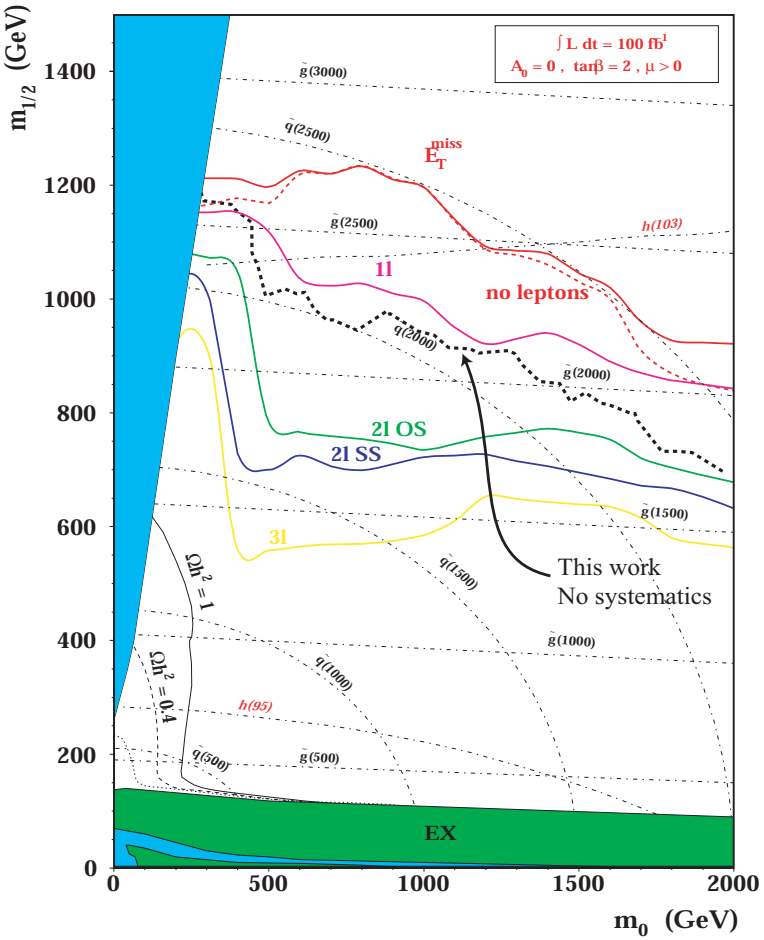

Figure 11.5: Comparison of this work to an earlier CMS study given in Reference [69] for 100 fb^{-1}. The plot displays the single lepton reach ("1l" curve given by the magenta line) in the (m_0, $m_{1/2}$) plane, for fixed mSUGRA parameters: A_0, $\tan\beta = 2$, and $mu > 0$. The dashed curve shows the inclusive muon reach of this work, for fixed mSUGRA parameters: A_0, $\tan\beta = 10$, and $mu > 0$. Whereas reference [69] optimized for all points in the plane, the reach presented in the lower plot is optimized for only one low universal scalar point (HM1). Indeed, one sees that the two studies agree quite well for universal scalar mass above 1200 GeV; for higher values, the reach presented in Reference [69] tends to be somewhat stronger.

11.5 Conclusion

This work demonstrates that the low mass mSUGRA benchmark point LM1 will be easily observable given 10 fb^{-1} of data. The optimized cuts for this point are

used to scan across $(m_0, m_{1/2})$ plane, and the results indicate that most of the low mass region for $A_0 = 0$, $\mu > 0$, and $\tan\beta = 10$ can be observed up to mass scales of ~ 1.5 TeV/c^2, including systematic effects. With 30 fb^{-1} of data, the high mass SUSY benchmark points become interesting for possible discovery and with 60 fb^{-1} of data, SUSY mass scales beyond 2 TeV/c^2 can be probed, including systematic uncertainties. It is noted that while the requirement of single muon events with large jet and missing E_T provides good separability between SUSY events and the Standard Model background, this signature, and therefore the selection cuts used in this dissertation are not necessarily unique to Supersymmetry and may be applicable to other theories beyond the Standard Model which contain particles of very high mass (Appendix D).

APPENDIX A
ORCA RECQUERIES USED FOR PHYSICS OBJECTS

```
%

%//RecQuery used for Muons

%//---------------------------

MuonRecQuery = new RecQuery("GlobalMuonReconstructor");


//RecQuery used for Jets

//---------------------------

JetRecQuery->setParameter<string>("JetInput", "EcalPlusHcalTowerUEInput");

JetRecQuery->setParameter("EcalPlusHcalTowerEt", 0.5);

JetRecQuery->setParameter<int>("JetAlgorithm", 2);

JetRecQuery->setParameter<int>("JetRecom", 4);

JetRecQuery->setParameter("ConeCut", 0.5);

JetRecQuery->setParameter("ConeSeedEtCut", 0.0);

JetRecQuery->setParameter<string>("JetCalibration", "GammaJet");

JetRecQuery->setParameter<string>("GammaJetCalibrationType",

"PartonScale_IterativeCone0.5_EtScheme_UEInput_Jets872pre3_2x1033PU761_TkMu_g133_OSC");

JetRecQuery->setParameter("JetEtCut", 10.0);

JetRecQuery->setParameter<string>("JetSortType", "byEt");


//RecQuery used for Missing ET

//---------------------------

MetRecQuery = new RecQuery("METfromCaloRecHit");
```

APPENDIX B
CUT-SET EFFICIENCIES

B.1 ORCA Cut-set Efficiencies for Standard Model Backgrounds

Table B.1: Efficiency of Electro-weak Standard Model backgrounds to pass selection cuts calculated using ORCA. Cuts are applied sequentially, moving down the table. The remaining cross section (fb) after cumulative cuts is shown along with the cut efficiency in parentheses.

	$W+jets$	$Z+jets$	$ZZ+jets$	$ZW+jets$	$WW+jets$
x-sect[fb]	1.542×10^{8}	3.901×10^{7}	1.111×10^{4}	2.686×10^{4}	1.881×10^{5}
$P_T^{\mu 1}$	$1.741\times10^{7}(11\%)$	$2.725\times10^{6}(6\%)$	641.2(5%)	2043(7%)	$2.274\times10^{4}(12\%)$
$\mu_1(ISOE_T<10)$	$1.647\times10^{7}(94\%)$	$2.572\times10^{6}(94\%)$	550.8(85%)	1836(89%)	$1.978\times10^{4}(86\%)$
$N_{jets}(E_T>50)$	$6859(<1\%)$	$2377(<1\%)$	9.967(1%)	18.49(1%)	3540(17%)
E_T^{J1}	72.69(1%)	$12.4(<1\%)$	$0.0697(<1\%)$	0.292(1%)	65.02(1%)
E_T^{J2}	0.7283(1%)	0.2875(2%)	0.0232(33%)	0	19.86(30%)
η^{J1}	0.7136(97%)	0.2875(100%)	0.0232(100%)	0	16.35(82%)
η^{J2}	0.4944(69%)	0.2244(78%)	0.0232(100%)	0	14.4(88%)
η^{J3}	0.4944(100%)	0.2244(100%)	0.0232(100%)	0	14.4(100%)
$cos(\Delta\phi(J1,J2))$	0.3107(62%)	0.1958(87%)	0.0232(100%)	0	14.4(100%)
$cos(\Delta\phi(\not\!\!E_T,J1))$	0.2106(67%)	0.0601(30%)	0	0	3.504(24%)
$cos(\Delta\phi(\not\!\!E_T,J2))$	0.2106(100%)	0.0459(76%)	0	0	2.725(77%)
$\not\!\!E_T$	0.1959(93%)	0.0247(53%)	0	0	0
Final Eff.	$1.27\times10^{-7}\%$	$6.321\times10^{-8}\%$	0%	0%	0%

Table B.2: Efficiency of QCD di-jet events and ttbar Standard Model backgrounds to pass selection cuts calculated using ORCA. Cuts are applied sequentially, moving down the table. The remaining cross section (fb) after cumulative cuts is shown along with the cut efficiency in parentheses.

	QCD	$t\bar{t}$
x-sect[fb]	5.754×10^{13}	4.92×10^{5}
$P_T^{\mu 1}$	$5.359 \times 10^{7} (< 1\%)$	$7.85 \times 10^{4} (15\%)$
$\mu_1(ISOE_T < 10)$	$3.345 \times 10^{7} (62\%)$	$5.641 \times 10^{4} (71\%)$
$N_{jets}(E_T > 50)$	$3631 (< 1\%)$	$2.125 \times 10^{4} (37\%)$
E_T^{J1}	$110.8 (3\%)$	$65.83 (< 1\%)$
E_T^{J2}	$28.77 (25\%)$	$3.941 (5\%)$
η^{J1}	$28.77 (100\%)$	$3.941 (100\%)$
η^{J2}	$26.09 (90\%)$	$3.357 (85\%)$
η^{J3}	$26.09 (100\%)$	$3.357 (100\%)$
$cos(\Delta\phi(J1, J2))$	$26.09 (100\%)$	$3.357 (100\%)$
$cos(\Delta\phi(\not\!\!E_T, J1))$	$5.457 (20\%)$	$0.5838 (17\%)$
$cos(\Delta\phi(\not\!\!E_T, J2))$	$1.291 (23\%)$	$0.2919 (50\%)$
$\not\!\!E_T$	0	$0.146 (50\%)$
Final Eff.	0%	$2.897 \times 10^{-5}\%$

Table B.3: This table shows the decomposition of the ORCA samples which contribute to the background estimate using LM1 optimized cuts. The HLT efficiencies are also estimated from ORCA and are applied. All numbers shown assume 10 fb^{-1}.

Process	Bin	p_T range (GeV/c)	$n_{pass}^{unweighted}$	weight	$< \epsilon_{HLT} >$	$< \epsilon_{HLT} > \cdot N_{pass}^{weighted}$	$\sigma(N_{pass}^{weighted})$
W+jets	9	$550 < p_T < 800$	7	0.147	80%	0.82	0.31
W+jets	10	$800 < p_T < 4400$	18	0.052	80%	0.74	0.18
Z+jets	10	$800 < p_T < 4400$	5	0.049	100%	0.24	0.11
$t\bar{t}$	-	inclusive	1	1.46	50%	0.73	0.73
Total						2.54	0.82 (32%)

B.2 ORCA Cut-set Efficiencies for mSUGRA Signal Benchmark points

Table B.4: Efficiency of mSUGRA signal points to pass selection cuts calculated using ORCA. Cuts are applied sequentially, moving down the table. The remaining cross section (fb) after cumulative cuts is shown along with the cut efficiency in parentheses.

	LM1	LM4	LM5	LM6	HM1
x-sect[fb]	4.197×10^4	1.894×10^4	6030	4034	52.03
HLT	4861(11%)	2055(10%)	668.9(11%)	784.3(19%)	13.79(26%)
$P_T^{\mu 1}$	2801(57%)	1692(82%)	552.2(82%)	619.9(79%)	12.63(91%)
$\mu_1(ISOE_T < 10)$	2189(78%)	1323(78%)	424.3(76%)	481.2(77%)	9.423(74%)
$N_{jets}(E_T > 50)$	1415(64%)	1049(79%)	334.9(78%)	330.9(68%)	5.102(54%)
E_T^{J1}	374.2(26%)	324.2(30%)	155.9(46%)	190.2(57%)	4.363(85%)
E_T^{J2}	59.71(15%)	56.54(17%)	31.78(20%)	45.39(23%)	2.58(59%)
E_T^{J3}	59.71(100%)	56.54(100%)	31.78(100%)	45.39(100%)	2.58(100%)
η^{J1}	58.87(98%)	54.98(97%)	30.98(97%)	44.89(98%)	2.564(99%)
η^{J2}	51.72(87%)	49.33(89%)	28.97(93%)	41.86(93%)	2.369(92%)
η^{J3}	51.72(100%)	48.94(99%)	27.96(96%)	40.85(97%)	2.346(99%)
$cos(\Delta\phi(J1, J2))$	48.36(93%)	46.6(95%)	25.95(92%)	37.83(92%)	1.767(75%)
$cos(\Delta\phi(\not{E}_T, J1))$	38.69(80%)	31.78(68%)	19.51(75%)	30.26(79%)	1.383(78%)
$cos(\Delta\phi(\not{E}_T, J2))$	36.58(94%)	29.64(93%)	18.71(95%)	30.26(100%)	1.319(95%)
$\not{E}_T$	31.12(85%)	24.57(82%)	16.5(88%)	27.74(91%)	1.27(96%)
Final Eff.	0.07416%	0.1295%	0.2733%	0.6875%	2.439%
Eff (No HLT).	0.07817%	0.1469%	0.3067%	0.775%	2.724%
HLT Eff.	94.9%	88.2%	89.1%	88.7%	89.5%

B.3 FAMOS Cut-set Efficiencies for mSUGRA Signal Benchmark points

Table B.5: Efficiency of mSUGRA signal points to pass selection cuts calculated using FAMOS. Cuts are applied sequentially, moving down the table. The remaining cross section (fb) after cumulative cuts is shown along with the cut efficiency in parentheses.

	LM1	LM4	LM5	LM6	HM1
x-sect[fb]	4.197×10^4	1.894×10^4	6030	4034	52.03
$P_T^{\mu 1}$	4077(9%)	2653(14%)	874.1(14%)	848.5(21%)	16.47(31%)
$\mu_1(ISOE_T < 10)$	2514(61%)	1625(61%)	506.5(57%)	598.6(70%)	12.33(74%)
$N_{jets}(E_T > 50)$	1709(68%)	1283(78%)	409.1(80%)	427.1(71%)	7.186(58%)
E_T^{J1}	443.2(25%)	396.3(30%)	165.4(40%)	219.1(51%)	5.84(81%)
E_T^{J2}	78.6(17%)	77.41(19%)	39.14(23%)	53.5(24%)	3.234(55%)
E_T^{J3}	78.6(100%)	77.41(100%)	39.14(100%)	53.5(100%)	3.234(100%)
η^{J1}	75.79(96%)	77.02(99%)	39.02(99%)	52.76(98%)	3.214(99%)
η^{J2}	69.82(92%)	67.4(87%)	34.83(89%)	48.83(92%)	2.999(93%)
η^{J3}	67.72(96%)	67.01(99%)	34.22(98%)	47.27(96%)	2.956(98%)
$cos(\Delta\phi(J1, J2))$	63.51(93%)	63.54(94%)	32.49(94%)	44.9(94%)	2.3(77%)
$cos(\Delta\phi(\not{E}_T, J1))$	42.81(67%)	38.13(59%)	22.4(68%)	33.92(75%)	1.702(73%)
$cos(\Delta\phi(\not{E}_T, J2))$	38.6(90%)	33.12(86%)	19.94(89%)	31.3(92%)	1.614(94%)
$\not{E}_T$	32.63(84%)	28.5(86%)	18.34(91%)	29.08(92%)	1.572(97%)
Final Eff.	0.07774%	0.1505%	0.3041%	0.721%	3.022%
ORCA Eff. (No HLT)	0.07817%	0.1469%	0.3067%	0.775%	2.724%
% Diff.	0.55%	−2.45%	0.85%	6.96%	−10.94%

APPENDIX C
BACKGROUND NORMALIZATION

In this analysis, the Z+jets and W+jets backgrounds are estimated to contribute a combined 76% of the total background predicted by simulation to pass the selection cuts given in Table 11.1. Because events from processes like $Z(\rightarrow \mu^+\mu^-)$+jets can be efficiently selected by the reconstruction of the Z mass, measurements made during early running can help normalize the background estimates from simulation. Each additional jet in Z+jets events can be attributed to an additional strong coupling vertex from which a parton results; therefore, we should expect $\sigma(Z + N\texttt{jets}) \propto \alpha_s^{\texttt{N}}$. This implies that a distribution such as $\frac{d\sigma}{dN_{jet}} \propto \alpha_s$ (Fig. C.1) measured in Z+jets event data can be used to normalize simulation predictions.

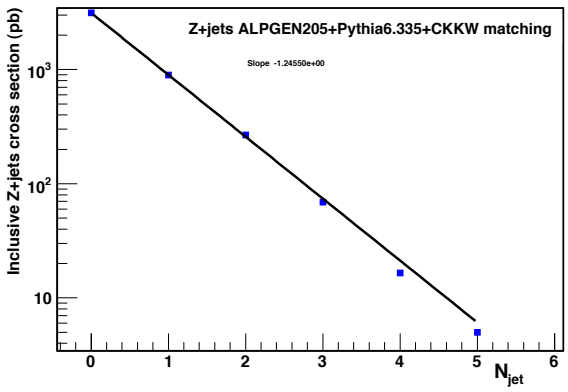

Figure C.1: Inclusive Z+jets cross section versus jet multiplicity [30].

Using the measured ratio $R = \mathcal{L}\frac{d\sigma}{dN_{\texttt{jets}}}$, which is expected to have minimal SUSY contamination in the low jet multiplicity region, and the observed number of events for $Z(\rightarrow \mu^+\mu^-)$ + 2jet events, the simulated number of events predicted for Z+$\geq$3jet events (in the signal region) can be normalized to data. Similarly, the measured ratio $\rho = \frac{\sigma(pp\rightarrow W(\rightarrow\mu\nu)+\texttt{jets})}{\sigma(pp\rightarrow\rightarrow Z(\rightarrow\mu^+\mu^-)+\texttt{jets})}$ can be used to normalize simulated W+jet events.

Therefore, by assuming flavor-independent gauge couplings to the leptons (lepton universality), the W and $Z + \geq 3$ jets events can be normalized to $Z(\rightarrow \mu^+\mu^-)+ \geq$ 2jet data. By normalizing the electroweak predictions from simulation, challenging systematic uncertainties such as the choice of PDF, ISR/FSR, and jet energy scale can be avoided, and the dominate source becomes the uncertainty on luminosity and on the measurement of R and ρ, the total of which is at the level of 5% [30].

APPENDIX D
OTHER THEORIES BEYOND THE STANDARD MODEL

The event topology of single muon events plus large jet and missing E_T is a generic signature of high mass particle decays introduced in many theories beyond the Standard Model. Because the Standard Model events that pass the selection cuts in this dissertation are due to W+jets, Z+jets, and $t\bar{t}$ events, other theories beyond the Standard Model which result in the production of heavy W- or Z-like bosons (W' or Z') or other heavy particles which couple to the top-quark might also result in similar topologies. These are discussed below.

Reference [70] provides an estimate on the ability of CMS to observe events containing the so-called heavy quark T given by Little Higgs Models. This TeV mass scale quark can decay to the Standard Model top by radiating a Z-boson and therefore cause events with high E_T jets and large missing E_T. Muons can be produced through the subsequent b-quark decays. CMS is estimated to have a sensitivity of $\mathcal{O}(1$ TeV) given 30 fb^{-1} by reconstructing the Z + top invariant mass.

Many extensions to the Standard Model, included Little Higgs models and Universal Extra Dimensions can give rise to so-called W's and Z's. These can be very massive ($\mathcal{O}$(TeV)) and have the same couplings as their Standard Model counterparts. This implies events which contain either W' or Z' decays will not only have a similar event topology as SUSY events (as evident by the number of Standard Model events which remain in the signal region), but the reconstructed objects will be typically more energetic, and therefore more mSUGRA-like. Reference [71] estimates that CMS should be able to detect Z's through decays to $\mu^+\mu^-$ up to $\mathcal{O}(4$ TeV) by reconstructing the invariant di-μ mass. Reference [30] indicates that by examining

the transverse mass distribution in single-μ events, the W' can be observed up to $\mathcal{O}(5$ TeV) with 10 fb^{-1}.

REFERENCES

[1] P.D.B. Collins, A.D. Martin, and E.J. Squires. *Particle Physics and Cosmology.* John Wiley & Sons, Inc., New York, 1989.

[2] N. Tagg (for the MINOS Collaboration). arXiv:hep-ex/0605058, 2006.

[3] S. Eidelman, K.G. Hayes, K.A. Olive, M. Aguilar-Benitez, C. Amsler, D. Asner et al. (Particle Data Group). *Phys. Lett.*, B592:1, 2004.

[4] J.L. Hewett. arXiv:hep-ph/9810316, 1998.

[5] A.D. Martin F. Halzen. *Quarks and Leptons: An Introductory Course in Modern Particle Physics.* John Wiley & Sons, Inc., New York, 1984.

[6] D. Griffiths. *Introduction to Elementary Particles.* John Wiley and Sons, Inc, New York, 1987.

[7] D.V. Schroeder M.E. Peskin. *An Introduction to Quantum Field Theory.* Addison Wesley, Reading, 1995.

[8] S. L. Glashow. *Nucl. Phys.*, 22:579–588, 1961.

[9] S. Weinberg. *Phys. Rev. Lett.*, 19:1264–1266, 1967.

[10] A. Salam. Originally printed in Svartholm: Elementary Particle Theory, Proceedings Of The Nobel Symposium Held 1968 At Lerum, Sweden, Stockholm 1968, 367-377.

[11] P.W. Higgs. *Phys. Lett.*, 12:132–133, 1964.

[12] P.W. Higgs. *Phys. Rev. Lett.*, 13:508–509, 1964.

[13] G. Abbiendi, C. Ainsley, P.F. Akesson, G. Alexander, G. Anagnostou, K.J. Anderson et al. (The OPAL Collaboration). *Eur. Phys. J.*, C45:1–21, 2006. hep-ex/0505072.

[14] J. Abdallah, P. Abreu, W. Adam, P. Adzic, T. Albrecht, T. Alderweireld et al. (The DELPHI Collaboration). *Eur. Phys. J.*, C38:413–426, 2005. hep-ex/0410071.

[15] M.J. Rees. *Phil. Trans. Roy. Soc. Lond.*, 361:2427–2434, 2003. arXiv:astro-ph/0402045.

[16] D.N. Spergel, L. Verde, H.V. Peiris, E. Komatsu, M.R. Nolta, C.L. Bennett et al. (The WMAP Collaboration). *Astrophys. J. Suppl.*, 148:175, 2003. arXiv:astro-ph/0302209.

[17] P. Fayet and S. Ferrara. *Phys. Rept.*, 32:249–334, 1977.

[18] P. Ramond. *Jouneys Beyond the Standard Model.* Perseus Books, Cabridge, 1999.

[19] S.P. Martin. arXiv:hep-ph/9709356, 1997.

[20] M. Shiozawa, B. Viren, Y. Fukuda, T. Hayakawa, E. Ichihara, K. Inoue et al. (The Super-Kamiokande Collaboration. *Phys. Rev. Lett.*, 81:3319–3323, 1998. arXiv:hep-ex/9806014.

[21] L. Girardello and M.T. Grisaru. *Nucl. Phys.*, B194:65, 1982.

[22] W. de Boer and C. Sander. *Phys. Lett.*, B585:276–286, 2004. arXiv:hep-ph/0307049.

[23] S. Dawson. arXiv:hep-ph/9612229, 1996.

[24] V.D. Barger, M.S. Berger, and P. Ohmann. *Phys. Rev.*, D49:4908–4930, 1994. arXiv:hep-ph/9311269.

[25] S. Ask, B. Clerbaux, G. Ganis, P. Giacomelli, H. Novak, L. Pape, C. Rembser and S. Rosier (The LEP SUSY Working Group). http://lepsusy.web.cern.ch/lepsusy/, last checked August 1, 2006.

[26] A. Heister, S. Schael, R. Barate, R. Bruneliere, I. De Bonis, D. Decamp et al. (The ALEPH Collaboration). *Phys. Lett.*, B526:206–220, 2002. arXiv:hep-ex/0112011.

[27] T. Affolder, H. Akimoto, A. Akopian, M.G. Albrow, P. Amaral, S.R. Amendolia et al. (The CDF Collaboration). *Phys. Rev. Lett.*, 84:5704–5709, 2000. arXiv:hep-ex/9910049.

[28] B. Abbott, M. Abolins, V. Abramov, B.S. Acharya, I. Adam, D.L. Adams et al. (The D0 Collaboration). *Phys. Rev. Lett.*, 83:4937–4942, 1999. arXiv:hep-ex/9902013.

[29] T. Affolder, H. Akimoto, A. Akopian, M.G. Albrow, P. Amaral, S.R. Amendolia et al. (The CDF Collaboration). *Phys. Rev. Lett.*, 84:5704–5709, 2000. arXiv:hep-ex/9910049.

[30] L. Baksay, J. Huang, G. Zilizi, L. Tauscher, F.R. Cavallo, E. Booth et al. (The CMS Collaboration). CERN-LHCC-2006-21, 2006.

[31] L. Baksay, J. Huang, G. Zilizi, L. Tauscher, F.R. Cavallo, E. Booth et al. (The CMS Collaboration). CERN-LHCC-2000-38, 2000.

[32] R. Fernow. *Introduction to Experimental Particle Physics.* Cambridge University Press, New York, 1990.

[33] L. Baksay, J. Huang, G. Zilizi, L. Tauscher, F.R. Cavallo, E. Booth et al. (The CMS Collaboration). CERN-LHCC-2006-02, 2006.

[34] J.D. Jackson. *Classical Electrodynamics.* John Wiley & Sons, Inc., New York, 1998.

[35] O. Bruning, P. Collier, P. Lebrun, S. Myers, R. Ostojic, J. Poole et al. CERN-2004-003, 2004.

[36] L. Baksay, J. Huang, G. Zilizi, L. Tauscher, F.R. Cavallo, E. Booth et al. (The CMS Collaboration). CERN-LHCC-94-38, 1994.

[37] L. Baksay, J. Huang, G. Zilizi, L. Tauscher, F.R. Cavallo, E. Booth et al. (The CMS Collaboration). CERN-LHCC-97-10, 1997.

[38] http://cms.cern.ch/MTCC.html (last checked 7/9/2006).

[39] W.B. Rolnick. *The Fundamental Particles and Their Interactions.* Addison-Wesley, New York, 1994.

[40] L. Baksay, J. Huang, G. Zilizi, L. Tauscher, F.R. Cavallo, E. Booth et al. (The CMS Collaboration). CERN-LHCC-98-6, 1998, Addendum CERN/LHCC 2000-016.

[41] L. Baksay, J. Huang, G. Zilizi, L. Tauscher, F.R. Cavallo, E. Booth et al. (The CMS Collaboration). CERN-LHCC-97-33, 1997.

[42] L. Baksay, J. Huang, G. Zilizi, L. Tauscher, F.R. Cavallo, E. Booth et al. (The CMS Collaboration). CERN-LHCC-97-31, 1997.

[43] L. Baksay, J. Huang, G. Zilizi, L. Tauscher, F.R. Cavallo, E. Booth et al. (The CMS Collaboration). CERN-LHCC-97-32, 1997.

[44] D. Acosta, A. Madorsky, B. Scurlock, S.M. Wang, A. Atamanchuk, V. Golovtsov and B. Razmyslovich. CERN-CMS-NOTE-1999-060, 1999.

[45] A. Clements. *Microprocessor System Design.* PWS Publishing Company, Boston, 1992.

[46] Stoutimore M. Acosta, D. and S.M. Wang. CERN-CMS-NOTE-2001-033, 2001.

[47] D. Acosta, N. Adams, A. Atamanchouk, R. D. Cousins, M. I. Ferguson, V. Golovtsov, J. Hauser, A. Madorsky, M. Matveev, J. Mumford, T. Nussbaum, P. Padley, B. Razmyslovich, V. Sedov, W. Smith and B. Tannenbaum. *Nucl. Instrum. Meth.*, A496:64–82, 2003.

[48] V. Brigljevic, G. Bruno, E. Cano, A. Csilling, S. Cittolin, D. Gigi et al. *ECONF*, C0303241:MOGT008, 2003. arXiv:hep-ex/0305076.

[49] M.A. Dobbs, S. Frixione, E. Laenen, K. Tollefson, H. Baer, E. Boos et al. hep-ph/0403045, 2004.

[50] T. Sjostrand, S. Mrenna, and P. Skands. *JHEP*, 05:026, 2006. arXiv:hep-ph/0603175.

[51] F.E. Paige, S.D. Protopopescu, H. Baer, and X. Tata. 2003. arXiv:hep-ph/0312045.

[52] H.L. Lai, J. Botts, J. Huston, J.G. Morfin, J.F. Owens, J. Qiu, W.K. Tung and H. Weerts. *Phys. Rev.*, D51:4763–4782, 1995. arXiv:hep-ph/9410404.

[53] J. Allison, K. Amako, J. Apostolakis, H. Araujo, P.A. Dubois, M. Asai et al. *IEEE Trans. Nucl. Sci.*, 53:270, 2006.

[54] M. Battaglia, A. De Roeck, J. Ellis, F. Gianotti, K.T. Matchev, K.A. Olive, L. Pape, G. Wilson. *Eur. Phys. J.*, C22:535–561, 2001. arXiv:hep-ph/0106204.

[55] H.N. Brown, G. Bunce, R.M. Carey, P. Cushman, G.T. Danby, P.T. Debevec et al. (The Muon g-2 Collaboration). *Phys. Rev. Lett.*, 86:2227–2231, 2001. arXiv:hep-ex/0102017.

[56] D.A. Demir and K.A. Olive. *Phys. Rev.*, D65:034007, 2002. arXiv:hep-ph/0107329.

[57] M. Battaglia, A. De Roeck, J. Ellis, F. Gianotti, K.A. Olive, L. Pape. *Eur. Phys. J.*, C33:273–296, 2004. arXiv:hep-ph/0306219.

[58] A. De Roeck, John R. Ellis, F. Gianotti, F. Moortgat, K.A. Olive and L. Pape. hep-ph/0508198, 2005.

[59] M.L. Mangano, M. Moretti, F. Piccinini, R. Pittau, and A.D. Polosa. *JHEP*, 07:001, 2003. arXiv:hep-ph/0206293.

[60] S. Frixione and B.R. Webber. *JHEP*, 06:029, 2002. arXiv:hep-ph/0204244.

[61] A. Heister, O. Kodolova, V. Konoplianikov, S. Petrushanko, J. Rohlf, C. Tully and A. Ulyanov. CERN-CMS-NOTE-AN2005-005, 2005.

[62] M. Spiropulu. FERMILAB-THESIS-2000-16, 2000.

[63] D. Tsybychev. FERMILAB-THESIS-2004-58, 2004.

[64] C. Tully and J. Rohlf. CERN-CMS-IN-2006-025, 2006.

[65] J. Hartet et al. CERN-CMS-AN-2006-048, 2006.

[66] A. Pukhov, E. Boos, M. Dubinin, V. Edneral, V. Ilyin, D. Kovalenko, A. Kryukov, V. Savrin, S. Shichanin, A. Semenov. arXiv:hep-ph/9908288, 1999.

[67] J. D'Hondt, J. Heyninck, and S. Lowette. CERN-CMS-NOTE-AN2006-064, 2006.

[68] S. Abdullin, D. Acosta, P. Bartalini, R. Cavanaugh, A. Drozdetskiy, G. Karapostoli, G. Mitselmakher, Yu. Pakhotin, B. Scurlock, M. Spiropulu. arXiv:hep-ph/0605143, 2006.

[69] S. Abdullin and F. Charles. *Nucl. Phys.*, B547:60–80, 1999. arXiv:hep-ph/9811402.

[70] K. Karafasoulis, A. Kyriakis, and H. Petrakou. CERN-CMS-NOTE-2006-079, 2006.

[71] R. Cousins, J. Mumford, and V. Valuev. CERN-CMS-NOTE-2006-062, 2006.

BIOGRAPHICAL SKETCH

Bobby Scurlock was born in Miami, Florida, on June 11, 1976. His interest in physics was sparked by the excellent instruction of his physics high school teacher David Jones. In 1996, he began his undergraduate career at the University of Florida, where he obtained a Bachelor of Science in physics with highest honors and a Bachelor of Arts in philosophy with honors. In 1998, he began working under the direction of Dr. Darin Acosta in the experimental high energy physics group on the development of the endcap muon track-finder to be used at the CMS experiment at CERN. He was accepted into the University of Florida physics graduate program in 2000 and continued working with Dr. Acosta. During his time as a graduate student, Bobby became well known in the Physics Department for his caricatures of various members of the faculty, as well as his jump shot.